MID-INFRARED CHARACTERIZATION OF TWO-DIMENSIONAL PHOTONIC

CRYSTAL SLABS FABRICATED IN SILICON WITH LASER INTERFERENCE

LITHOGRAPHY

Liviu Prodan

Graduation committee

Chairman

Prof. dr. F. G. Mugele   University of Twente, The Netherlands

Promotor

Prof. dr. K. J. Boller   University of Twente, The Netherlands

Co-Promotor

Prof. dr.   L. Kuipers   University of Twente, The Netherlands

Assistant promotor

Dr. P. Gross   University of Münster, Germany

Members

Prof. dr. R. Beigang   University of Kaiserslautern, Germany
Prof. dr. J. Herek   University of Twente, The Netherlands
Prof. dr. A. Driessen   University of Twente, The Netherlands

MID-INFRARED CHARACTERIZATION OF TWO-DIMENSIONAL PHOTONIC

CRYSTAL SLABS FABRICATED IN SILICON WITH LASER INTERFERENCE

LITHOGRAPHY

DISSERTATION

to obtain
the degree of doctor at the University of Twente,
on the authority of the rector magnificus,
prof.dr. W.H.M. Zijm,
on account of the decision of the graduation committee,
to be publicly defended
on Friday the 28th of March at 13.15

by

Liviu Prodan

born on the 25th of January 1976

in Iasi, Romania

This doctoral dissertation is approved by

promotor   Prof. dr. K. J. Boller

co-promotor   Prof. dr.   L. Kuipers

assistant promotor   Dr. P. Gross

Publications

Journals

- L. Prodan, P. Gross, H. Offerhaus, J. Herek, J. Korterik, P.J.M. van der Slot, M. Lutthikof, H. Hemmes, R. Beigang, L. Kuipers and K.-J. Boller, "Nonlinear optical response of a large-area 2D silicon photonic crystal slab: phase changes of mid-IR femtosecond pulses in reflection", to be submitted.

- L. Prodan, R. Hagen, P. Gross, R. Arts, R. Beigang, C. Fallnich, A. Schirmacher, L. Kuipers and K.-J. Boller, "Mid-IR transmission of a large-area 2D silicon photonic crystal slab", submitted to *Journal of Physics D: Applied Physics* (2008).

- L. Prodan, P. Gross, R. Beigang, L. Kuipers, and K.-J. Boller, "Spectral investigation of a large-area 2D silicon photonic crystal slab for mid-IR radiation", *Journal of Physics D: Applied Physics* **40**, 5571 (2007).

- L. Prodan, T. Euser, H. van Wolferen, C. Bostan, R. de Ridder, R. Beigang, K.-J. Boller, and L. Kuipers, "Large Area 2D Silicon Photonic Crystals for Infrared Light fabricated with Laser Interference Lithography", *Nanotechnology* **15,** 639 (2004).

Conferences

- L. Prodan et.al., posters presentations: Mesa + International meeting, The Netherlands, (2004, 2005, 2006, 2007 and 2008).
- L. Prodan et.al., posters presentations: fall meeting of the section Optics Physics, Lunteren, The Netherlands, (2005, 2006 and 2007).
- L. Prodan et.al., posters presentations: Physics@Veldhoven, Veldhoven, The Netherlands, (2007 and 2008).
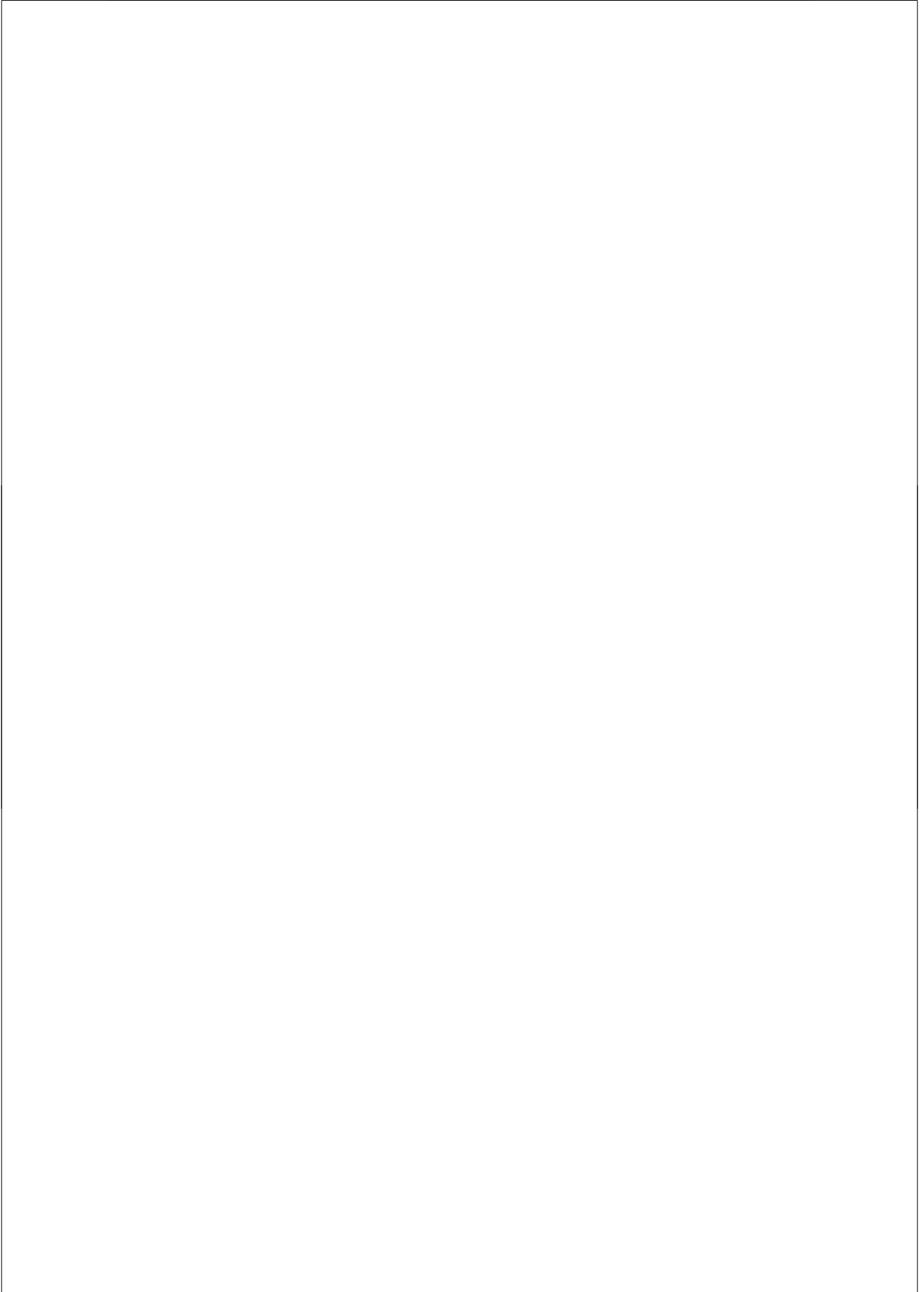
To my wife, my daughter and my parents

Abstract

The goal of the present work was to perform mid-infrared characterization of two dimensional photonic crystal slabs fabricated in silicon with laser interference lithography.

A two-dimensional (2D) silicon photonic crystal (PhC), which is designed to provide a modified dispersion for photon energies of less than half of the electronic band gap of silicon, and which has been fabricated by a novel modification of laser interference lithography (LIL), is studied by angular dependent infrared reflectivity and transmission measurements. The existence of resonance features is experimentally demonstrated as observed in the polarized reflectivity and transmission spectra, and which arises from resonant coupling of the incident infrared radiation to photonic modes. The measured photonic crystal resonances are used to derive the quality factors of the probed photonic modes via fits to the Fano-type line shapes found. The quality factor of the corresponding photonic modes is also theoretically calculated. The obtained theoretical values, and comparison with the experimentally obtained quality factors, provide the first information on the LIL fabrication-inherent quality of the crystals.

In the named experiments, the LIL fabricated crystals are investigated with low intensity probe beams in the near to mid-infrared range, such that an optically nonlinear response cannot be detected. To provide also information on the nonlinear response, we present initial results also at high intensities. For this, we have studied the light induced change in the optical phase upon reflection from the photonic crystal using a Mach-Zehnder setup. The technique involves measuring the time dependent reflection of a pulsed probe beam on the 2D PhC sample due to the excitation from an additional, pulsed drive beam. With this technique we have realized what we believe to be the first experimental observation of optical switching of the reflection phase from a guided resonance of a 2D PhC slab.

In conclusion, the goals that have been achieved are the development of a novel fabrication process for high-index 2D photonic crystals, the optically linear characterization of the properties of the fabricated crystal using specular reflectivity and normal incidence transmission experiments, and the first interferometric characterization of the optically nonlinear response of photonic crystal in terms of an optical switching of the reflection phase from a photonic resonance.

Contents

Mid-infrared characterization of two-dimensional photonic crystal slabs fabricated in silicon with laser interference lithography.

Chapter 1 Introduction

In the last 20 years the development of new optical technologies has accelerated significantly. Such technologies generally aim on the development of low cost optical systems designed for specific application requirements involving a compact and stable design. A primary goal of most of the current research area is the integration of a variety of discrete optical elements into a miniaturized planar photonic structure, to allow for a control of light on the wavelength scale and within ultrashort time scales. This includes low-loss dielectric thin films (waveguides) with a thickness in the region of one optical wavelength with a new class of materials called photonic crystals [1, 2].

Photonic crystals are also of fundamental importance in the control of light. This can qualitatively be seen, e.g., from the early work of Purcell who noted that spontaneous radiation can be enhanced or suppressed by placing the atoms in wavelength scale cavities [3]. Later, Kleppner suggested that in strongly scattering dielectric microstructures it should be possible to obtain a perfect isolation of electromagnetic modes, if a localized state of light can be formed [4]. This insight was developed further over the years and in 1987, the concept of photonic crystals was introduced [1, 2], including the term "photonic bandgap" (electromagnetic bandgap). This term was adopted in analogy to the electronic bandgap in crystals, where the periodic scattering of electronic matter waves gives rise to forbidden bands for the energy of electrons [5, 6]. Similarly, forbidden bands of photon energy (light frequency) occur for electromagnetic waves in a periodically scattering refractive index structure [1, 2]. Likewise, photons can, potentially be guided or trapped by particular structures [7].

With a variety of techniques, photonic crystals can now be fabricated to offer specific propagation properties [1, 6], e.g., a designable optical dispersion [8-10], control of spontaneous

emission [1, 11], localization of light [2, 7], and propagation along specific paths [12], particularly when high-index materials can be used. Besides their linear optical properties, out of which the mentioned possibilities arise, two-dimensional (2D) photonic crystals slabs are promising structures for nonlinear optical applications [13].

Research on the nonlinear optical properties of photonic crystals has seen extraordinary growth due to the potential applications based on altering the index of refraction on the femtosecond time scale such as through the third order optical nonlinearity, $\chi^{(3)}$. Additionally, the optically nonlinear properties of photonic crystals can be useful for exploiting new nonlinear effects [14], like gap solitons [15], nonlinear diffraction [16], second harmonic generation [17], and optical limiting [18]. More obviously the third order optical nonlinearity could be use to tune the transmission wavelength [19, 20], or to rapidly switch the transmission of photonic crystals [21].

However, despite their high potential, the nonlinear optical properties of photonic crystals have not been investigated as well as their linear optical properties. For instance, previous demonstrations of third-order nonlinear effects in photonic crystals have been dominated by unwanted linear absorption and resonant third-order nonlinear effects (two-photon absorption), which make the observation of the aimed effects difficult [20]. For example, if the photon energy is larger than half the electronic bandgap, and when high intensities are used to drive non-linear effects, this excites charge carriers. Once excited, this population decays rather slowly, with intra-band lifetimes in the picosecond to nanosecond range, which would limit the speed of optical switching accordingly. To overcome this issue, it is thus important to fabricate photonic crystals where a photonic bandgap is present at below half the electronic bandgap and to characterize their linear optical response before also the nonlinear optical response is investigated. Seen the typical values for electronic bandgaps found in photonic crystal materials, this means that photonic crystals need to be investigated with their photonic bandgap occurring at low photon energies, i.e., typically in the mid-IR.

As a promising candidate for corresponding investigations, this thesis focuses on the fabrication and characterization of two-dimensional photonic crystal slabs made from silicon. This choice is made because silicon exhibits excellent linear and nonlinear properties in the mid-IR spectral range, such as a broadband low-loss wavelength window ranging from 1.1 μm to nearly 7 μm, and a high refractive index. Also, Silicon offers good processability with currently available

2

lithographic techniques and the high third-order optical nonlinearity is about 100 times larger than, e.g., in silica [22].

However, the fabrication of suitable photonic crystals for infrared and mid-IR frequencies is, actually, a major technological challenge, because the typical period of the index pattern required is only of the order of a few hundred nanometers. Some effort has been devoted to the fabrication of two-dimensional (2D) photonic crystals due to their high versatility to vary the opto-geometric parameters, and because mature fabrication processes can be adapted. Conventional techniques to fabricate 2D photonic crystals are e-beam lithography (EBL) [23], focused ion beam (FIB) [24], and deep-UV lithography [25]. The main drawback of EBL and FIB is their sequential nature. As a result they are relatively slow and prone to drift, which makes them less useful for applications that require large areas of highly periodic lattices. Deep-UV lithography requires a lithographic mask, which is expensive for experimental work but would likely be the process to be adopted for large scale nanostructures. Nevertheless still, the mask is usually to be written sequentially by standard photolithography or electron beam lithography.

Laser interference lithography (LIL) [26] is an alternative mask-less lithographic technique, that offers many advantages over the latter techniques. LIL uses the interference of two laser beams from a standard UV laser to produce an interference pattern in a photosensitive resist, and where exposed areas can be chemically removed after development. In addition LIL can be combined with a sequential writing technique, like FIB, to place additional light guiding defects into a pre-made fabricated LIL structure if it is required [26]. Unfortunately the LIL technique, as it has been applied so far, has to be modified to work also with high index materials (such as Silicon or GaAs) because of important drawbacks. One of them is that unwanted standing wave patterns caused by the high Fresnel reflectivity of the substrate in the resist need to be suppressed which, otherwise, deteriorates the fabricated structure. Another problem comes from the limitation of the etching depth. Many materials etch slowly which results in poor pattern fidelity.

On the other hand, the optical interference on which LIL is based is well suited to fabricate photonic crystals because the large-scale period fidelity of the pattern on extended areas is an important factor for their performance. Furthermore, the technique is relatively simple and requires lower resources than deep UV lithography. Finally, LIL can generate submicron

3

patterned structures over large areas (square centimeters) in a short time (tens of seconds), because is not a sequential technique.

The large surface area of LIL fabricated crystals offers a significant advantage for spectral investigations. The reason is that the incoming light flux from sources of incandescent light (e.g. lamps), is extremely low after spatial and spectral filtering. With large area photonic crystals the spatial filtering requirements are strongly relaxed, which yields a much higher flux through the photonic crystal sample. This simplifies the setup and reduces measurement times, or contributes to a high signal-to-noise ratio. Large area 2D photonic crystal may also be used as spectral filters for light comprising a wider angular spread, if the incoming light frequency of certain transmission resonances does not vary much with the angle of incidence. Transmission measurements with sequentially fabricated 2D photonic crystals confirm these predictions [27, 28]. However, the mentioned crystals, due to the fabrication methods used, are very small (100 μm x 100 μm), which is approximately the cross section of a human hair. The disadvantage of this is that the light to be filtered has to possess high spatial coherence so that it can be focused through the small crystal area. This is usually not possible with the spatially incoherent light emitted by classical sources, such as from incandescent or fluorescent lamp-type of sources. As a result, the overall transmission would be low, leading to extended detection times or a low signal-to-noise ratio. We note that the focusability of light becomes even less in the mid-infrared spectral range and, additionally, detectors are less efficient in this range and thermal noise from background radiation is higher.

In this thesis (chapter 3) we describe a novel LIL fabrication process which is capable to pattern also high-index materials over large areas. This avoids the named disadvantages and, at the same time, allows to fabricate 2D photonic crystals based on a standard silicon-on-insulator technology. The usage of silicon-on-insulator technology is of special advantage due to the fact that silicon has excellent material properties. These are, e.g., a high thermal conductivity (about 10 times higher than GaAs) and a high optical damage threshold (about 10 times higher than GaAs). Furthermore, silicon is a semiconductor material available at low-cost. Finally, high-quality silicon on insulator (SOI) wafers offer a strong optical confinement through waveguiding due to the high index contrast between Si ($n = 3.4$) and the SiO_2 buffer layer ($n = 1.4$).

In our experiments we developed a novel modification of LIL fabrication which allows to

suppress undesired interference patterns, and which also allows to increase the etching depth. By applying this technique to SOI wafers, we fabricated a 2D silicon photonic crystal slab of exceptionally large area (1 x 1 cm^2). The design of the photonic crystal, a square pattern of round air holes with 1 μm spacing, is chosen to provide photonic resonances and bandgaps at wavelengths below about 2 μm wavelength, i.e., for photonic energies below half the electronic bandgap of silicon.

To quantify the influence of errors associated with the novel LIL fabrication technique, we have carried out a characterization of the linear optical properties of the crystal (chapters 4 and 5). This is based on measurements of the mid-IR reflectivity and transmission, in order to reconstruct the dispersion of photonic bands. In the measured spectra we found resonances which are the result of interference between directly reflected (or transmitted) light and light that first couples to the photonic crystal's resonant modes and then diffracts out with a certain phase delay. From this interference, resonance features (Fano-like resonances) were observed in the measured spectra, which change their position and shape as a function of the angle of incidence of the incoming infrared radiation. From the detailed investigation of the frequency and line shape of these resonances, the dispersion of the resonant modes is revealed, and the life time (quality factor) of the probed resonances is determined. The acquired values for the quality factors of individual photonic resonances form the first characterization of the fabrication quality achievable with the novel LIL method. Furthermore, the characterization was used to identify photonic resonances in the mid-IR which are of importance for the experimental investigation also of the nonlinear optical response of the fabricated crystal.

To investigate the nonlinear optical response of photonic crystal (chapter 6), we used ultrashort pulses in the mid-IR to measure the reflectivity of the photonic crystal at a photonic resonance while illuminating the crystal with a second ultrashort pulse. We observed that the second pulse, called here the drive pulse, changes the mid-IR reflectivity of the crystal on ultrashort time scales. All previous experimental observations of nonlinear effects in photonic crystals have been observed by monitoring changes in the reflected optical power [29-31]. However, this mode of observation requires a substantial spectral shift of photonic resonances with drive intensities that often require larger oscillator-amplifier systems with mJ level pulse energies. Here we report the observation of a nonlinear response at much lower intensities as achieved with lower pulse

energies of only a few nJ. Key to this experiment is to use, for the first time, an interferometric, and thus highly sensitive, detection of the phase shift associated with the nonlinear response of a photonic crystal.

The initial experimental results obtained thereby may be termed as a nonlinear optical switching in a photonic crystal. It seems likely that, in the two switching experiments performed, one is based on two-photon absorption (with a longer wavelength drive pulse), while the other is based on single photon absorption (shorter wavelength drive laser). In the latter case, the available band width covered by the mid-IR probe pulses was sufficiently broad to observe an enhancement of phase switching via the involved photonic resonance.

References

[1] E. Yablonovitch, *Phys. Rev.Lett.* **58**, 2059 (1987)

[2] S. John, *Phys. Rev. Lett.* **58**, 2486 (1987)

[3] E.M. Purcell, *Phys. Rev.* **69**, 681 (1946)

[4] D. Kleppner, *Phys. Rev. Lett.* **47**, 232 (1981)

[5] N.W. Aschroft and N. Mermin, *Solid State Physics*, Thomson Learning, Stanford (1976)

[6] H.V. Houten and C.W.J. Beenakker, *Principles of solid state electron optics*, in E. Burstein, C. Weisbuch (Eds.), Confined Electrons and Photons: New Physics and Applications, Plenum Press, New York, p. 269 (1995)

[7] J.D. Joannopoulos, R.D. Maede, and J.N. Win, *Photonic crystals, molding the flow of light*, Princeton: Princeton University Press (1995)

[8] C.M. Soukoulis, *Photonic crystals and Light Localization in the 21st Century*, vol 563, Dordrecht: Kluwer (2000)

[9] K. Sakoda, *Optical properties of photonic crystals*, Springer Verlag (2001)

[10] S. Noda and T. Baba, *Roadmap on Photonic crystals*, Kluwer Academic (2003)

[11] P. Lodahl, A.F. van Driel, I.S. Nikolaev, A. Irman, K. Overgaag, D. Vanmaekelbergh and W.L. Vos, Nature 430 (7000), 654 (2004)

[12] S. Fan, J.N. Winn, A. Devenyi, J.C. Chen, R.D. Meade and J.D. Joannopoulos, *J. Opt. Soc. Am. B* **12**, 1267 (1995)

[13] R.E. Slusher and B.J. Eggleton, *Nonlinear Photonic Crystals*, Springer, Berlin (2003)

[14] e.g. articles in *Nonlinear Optics of Photonic Crystals*, edited by C.M. Bowden and A.M. Zheltikov, feature issue *J. Opt. Soc. Am B* **19**, 1961 (2002)

[15] S. John and N. Akozbek, *Phys. Rev. Lett.* **71**, 1168 (1993)

[16] V. Berger, *Phys. Rev. Lett.* **81**, 4136 (1998)

[17] P.K. Kashkarov, L.A. Golovan, A.B. Fedotov, A.I. Efimova, L.P. Kuznetsova, V.Y. Timoshenko, D.A. Sidorov-Biryukov, A.M. Zheltikov, and J.W. Haus, *J. Opt. Soc. Am. B* **19**, 2273 (2002)

[18] M. Scalora, J.P. Dowling, C. Bowden, and M.J. Bloemer, *Phys. Rev. Lett.* **73**, 1368 (1994)

[19] F. Raineri, C. Cojocaru, R. Raj, P. Monnier, A. Levenson, C. Seassal, X. Letartre and P.

Viktorovitch, *Opt. Lett.* **30,** 64 (2005)

[20] S. Leonard, H.M. van Driel, J. Schilling and R.B. Wehrspohn, *Phys. Rev. B* **66,** 161102(R) (2002)

[21] A. Hache and M. Bourgeois, *Appl. Phys. Lett.* **77,** 4089 (2000)

[22] M. Dinu,F. Quochi and H. Garcia H, *Appl. Phys. Lett.* **82** 2954 (2003)

[23] T.F. Krauss, Y.P. Song, S. Thoms, C. Wilkinson and R. Rue, *Electron. Lett.* **30**, 1444 (1994)

[24] C. Peeters, E. Fluck, A. Otter, M. Balistreri, J. Korterik, L. Kuipers and N. van Hulst, *Appl. Phys. Lett.* **77**, 142 (2000)

 [25] W. Boogaerts, V. Wiaux, D. Taillaert, S. Beckx, B. Luyssaert, P. Bienstman and R. Baets, *IEEE J. Sel. Top. Quantum Electron.* **8**, 928 (2002)

[26] L. Vogelaar, W. Nijdam, H. A. G. M. Wolferen, R.M. Ridder, F. Segerink, E. Flück, L. Kuipers and N.F. Hulst, *Adv. Mater.* **13,** 1551 (2001)

[27] S. Fan and J. D. Jonnopoulos, *Phys. Rev. B* **65**, 235112 (2002)

[28] C. Grillet, D. Freeman, B. Luther-Davies, S. Madden, R. McPhedran, D.J. Moss, M.J. Steel, B.J. Eggleton, *Opt. Express* **14**, 369 (2006)

[29] A.D. Bristow, J. Wells, W. Fan, A. Fox, M. Skolnick, D. Whittaker, A. Tahraomi, T. Krauss, and J. Roberts, *Appl. Phys. Lett.* **83**, 851 (2003)

[30] P. Murzyn, A.Z. Garcia-Zeniz, D.O. Kundys, A.M. Fox, J.R. Wells, D.M. Whittaker, M.S. Skolnick, T.F. Krauss, and J.S. Roberts, *Appl. Phys. Lett.* **88**, 141104 (2006)

[31] S.W. Leonard, H.M. van Driel, J.Schilling, and R.B. Wehrspohn, *Phys. Rev. B* **66**, 161102 (2002)

Mid-infrared characterization of two-dimensional photonic crystal slabs fabricated in silicon with laser interference lithography

Chapter 2 Theoretical description of photonic crystals

In this chapter, a brief outline is given on how photonic crystals can theoretically be described. Key for understanding the properties of photonic crystals is the description of the photonic band structure, i.e., how the band structure develops and how to calculate the band structure. There is a strong analogy between electrons moving in a periodic potential and photons scattering off periodic refractive index structures which allows to utilize much of the mathematics developed to describe the electronic band structure of semiconductors. We begin to describe the propagation of light in a periodic refractive index variation medium in one dimension (Bragg mirror), for which analytical solution can be obtained. This description is extended qualitatively to two-dimensional structures (see 2.1). Furthermore, three computational methods used for the study of 2D photonic crystals will be briefly outlined (see 2.2 - 2.4).

2.1 General introduction of photonic crystals

In general, a crystal is a spatially periodic arrangement of a basic building block. In a photonic crystal, the unit cell is made of materials with various dielectric constants. The dimensionality of a photonic crystal (PhC) is determined by the number of independent axes along which the lattice or variation of the refractive index is periodic (in one-, two- or three-dimensions, see figure 2.1) on typically the wavelength scale, in order to modify the propagation of light.
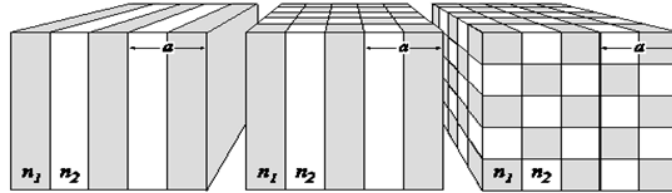
Figure 2.1 Periodic structures in 1, 2 and 3 dimensions. *a* correspond to the period of the structure, n_1 and n_2 represents the refractive indices of two different dielectric materials.

A 1D PhC is composed of a periodic stack of layers made from different dielectric materials, an example of what is a thin film multilayer. The optical properties of such multilayer stacks had since long been studied, well before the term photonic crystal was coined [2]. Qualitatively, the propagation of light in a 1D structure can be explained as follows. When light interacts with the materials of different refractive indices, scattering and diffraction occurs. For example, a multilayer stack consisting of alternating layers ("Bragg mirror"), the simplest example of a 1D PhC, can manipulate the light propagation via Bragg scattering [3] (see figure 2.2).
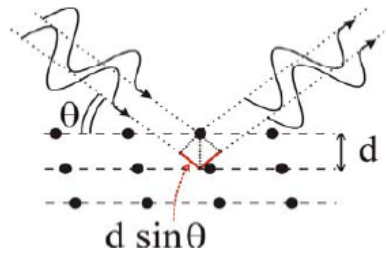

Figure 2.2 Schematic representation of Bragg diffraction.

The incoming waves are diffracted from the atomic lattice planes and can interfere destructively if maxima and minima of the reflected waves are superimposed, or constructively if the path difference between the incident and scattered waves is an integer (*m*) times the wavelength λ,

10

$$m\lambda = 2d\sin\theta$$

<div align="right">(2.1)</div>

where d is the lattice spacing, and θ is the angle of the incident wave with respect to the lattice plane.

In PhCs, the lattice spacing is on the order of the optical wavelength, causing strong Bragg diffraction to occur in this wavelength range. Bragg reflection of optical waves has been studied extensively for multilayer structures such as Bragg mirrors [4], and can also partially explain the physical origin of the optical properties of PhCs. A well-known example of such a structure is the multilayer coating found on mirrors and lenses. These coatings consist of multiple stacked thin layers, resulting in either a high reflectivity or high transmission for a certain range of wavelengths. As an example, a plane wave incident on the 1D PhC from left to right (see figure 2.3) will be repeatedly partially reflected at each material interface by Fresnel-reflections.
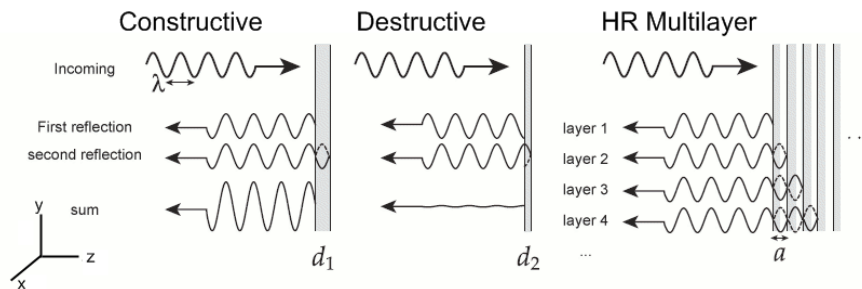

Figure 2.3 Schematic representation of interference process on a multilayer mirror.

Depending on the optical path length difference, which is given by the period a and the refractive index of the layers, the reflections can interfere constructively or destructively, such that light will be reflected or transmitted from the entire structure more effectively. A certain spectral range can be completely reflected by using a PhC with a large number of periods as in a highly reflective multi-layer mirror. This is an example of a 1D PhC having a stopband in its band structure in the direction perpendicular to the refractive index modulation. The spectral

position of the stopgap can be modified by changing the thickness and/or refractive index of the layer.

The difference between 1D and 2D PhCs is that a 2D PhC confines light in two dimensions rather than one. A 2D PhC consists of a periodic arrangement of materials with different refractive indices in two dimensions, as can be seen in figure 2.1. These types of structures have been studied extensively by Joannopoulos [6]. Light propagation through the crystal is explained by the interference of light, which is reflected, refracted and diffracted in the plane of the lattice by the periodic index variations. As a result, light propagation through the structure shows a dispersion which depends on the propagation direction, therefore the idea of a Brillouin zone, used to describe crystalline lattices is useful in explaining the PhC. Since photonic crystals have discrete translational symmetry, the calculations can be reduced by calculating all the photonic modes in the Brillouin zone, which is the unit cell of the reciprocal lattice (or *k*-space). The reciprocal lattice is the inverse of the real space [7]. Thus to calculate the dispersion of modes and the frequency range of a stopband, only the wave vectors within the first Brillouin zone have to be considered [6].

In order to create a photonic band gap, which is a stopgap formed in all propagation directions [5] in principle a 3D PhC is required [6]. However, 3D PhCs are difficult to manufacture because the crystalline order requires a low defect density in all three directions. 3D PhCs have been fabricated, e.g., by growing layers of colloids of high index materials surrounded by air [8]. A structure which is much easier to fabricate and where controllable defects (both points and line defects) can be fabricated is a 2D PhC slab. Here refractive index-guiding provides light confinement in the third dimension.

A rigorous treatment of light propagation and the band structure of PhC is accessible in many books (see e.g., [9]). In this thesis, we recall only the basic properties of PhCs in order to understand the optical properties of the PhC slab which is under experimental investigation here. The theoretical calculations used to predict the properties of a PhC are based on the assumption that PhCs are perfectly periodic and extend to infinity. In practice, however, there are limits to the size of structures, and there are deviations from the perfectly periodic PhC [6]. However still many of the optical properties of infinite perfectly fabricated periodic structures are found in finite photonic crystal samples that contain fabrication errors.

2.1.1 Theory of photonic crystal slabs

In this section approaches for a theoretical description of PhCs are recalled. A reader interested in more detailed mathematics should refer to the literature on this subject (see e.g., [6]).

In order to determine the existence of and quantify stopgaps, the dispersion relation of light propagation in the crystal is to be found, which is the dependence of the optical frequency, ω, on the wavevector, $\mathbf{k}$, in the crystal.

The starting point is the Maxwell equations, used to describe any electromagnetic phenomenon. These equations are as follows:

$$\nabla \cdot \vec{B} = 0 \qquad\qquad \nabla \times \vec{H} - \frac{\partial \vec{D}}{\partial t} = \vec{J}$$

$$\nabla \cdot \vec{D} = \rho \qquad\qquad \nabla \times \vec{E} + \frac{\partial \vec{B}}{\partial t} = 0 \tag{2.2}$$

where $\mathbf{B}$ is the magnetic flux (in units of tesla), ρ is the charge density (in units of C/m^3) and $\mathbf{D}$ is the electric displacement field (in units of of C/m^2), which is related to the electric field, $\mathbf{E}$ (in units of V/m), via a materials-dependent constant called the permittivity, ε, $\mathbf{J}$ is the current density (in units of A/m^2) and c is the vacuum speed of light (in units of m/s). The Maxwell equations are simplified by assuming that the dielectric media has no free charges or currents, therefore $\rho = 0$ and $\mathbf{J} = 0$. Second, it is assumed that the PhC is only subjected to weak radiation field strengths ($\sim$ V/cm), such that the induced polarization of the medium remains proportional to the electric field of the light, ignoring the higher order terms in the relation between $\mathbf{E}$ and $\mathbf{D}$. Third, it is assumed that ε at position r does not depend on the light frequency, therefore any frequency dependence in the relation between $\mathbf{D}$ and $\mathbf{E}$ is ignored. Fourth, the dielectric media is considered to have a magnetic permeability close to 1, so that the magnetic flux is equal with the magnetic field strength ($\mathbf{B} = \mathbf{H}$). Finally, we consider only low-loss (transparent) dielectric media, which means that $\varepsilon\!\left(\vec{r}\right)$ is a real number.

Considering these assumptions, reduces the relation between $\mathbf{D}$ and $\mathbf{E}$ to:

$$\vec{D}(r) = \varepsilon\left(\vec{r}\right)\vec{E}(r) \tag{2.3}$$

Where the dielectric constant can be defined by the following formula:

$$\varepsilon\left(\vec{r} + \vec{R}\right) = \varepsilon\left(\vec{r}\right) \tag{2.4}$$

where $\varepsilon\left(\vec{r}\right)$ is the dielectric constant which contains both the structural and the material information about the PhC. In particular, the dielectric constant is periodic with respect to the set $\Re = \left\{n_1\vec{a_1} + n_2\vec{a_2} + n_3\vec{a_3}; (n_1, n_2, n_3) \in Z^3\right\}$ of lattice vectors $\vec{R}$ generated by the basis lattice vectors $\vec{a_i}$, i=1, 2, 3 that describe the structure of the photonic crystal, and n_1, n_2, n_3 are integers. Now **E** can be eliminated to obtain the Helmholtz equation for H(r) (equation 2.5). This must be satisfied in order for a wave to propagate through the medium:

$$\nabla \times \left(\frac{1}{\varepsilon\left(\vec{r}\right)}\nabla \times \vec{H}\left(\vec{r}\right)\right) = \left(\frac{\omega}{c}\right)^2 \vec{H}\left(\vec{r}\right) \tag{2.5}$$

The goal is then to solve equation 2.5 i.e., its eigenmodes and eigenvalues for a given index variation $\varepsilon\left(\vec{r}\right)$ are to be found.

2.1.2 Solution in a homogeneous medium

In a homogeneous medium the permittivity is constant ($\varepsilon = \varepsilon_0\varepsilon_r$) and the master equation (2.5) reduces to a standard wave equation.
The solutions are then plane waves or spherical waves and arbitrary superpositions of them, such as:

14

$$\vec{H}(\vec{r}) = \vec{H}_0(\vec{r})e^{i\vec{k}\vec{r}} \qquad\qquad (2.6)$$

where H is the magnetic field, written as a space dependent amplitude with a harmonic space dependence, and k indicates the propagation direction.

Inserting equation 2.6 into equation 2.5 reveals the relationship between the light frequency and wavevector:

$$\omega = \frac{c}{\sqrt{\varepsilon}}k \qquad\qquad (2.7)$$

called the dispersion relation. Equation 2.7 means that a continuum of eigenmodes, $H(r)$, exists, which is characterized by the eigenvalues $\left(\dfrac{\omega}{c}\right)^2 = \dfrac{k^2}{\varepsilon}$, that lie on a straight line in an k-ω diagram, such as the described line in figure 2.4. Each point on this dispersion line corresponds to a mode. The dispersion line is, consequently, also called a band of modes.

2.1.3 Solution in a 1D photonic crystal

The H-field for a 1D PhC structure is found by solving equation 2.5, however, with ε now being a 1D periodic function of a space coordinate, e.g., z. The associated discrete translation symmetry of the crystal has consequences for the solutions of the wave equation. Two modes, one with the wave vector k_z and one with the wave vector $k_z+2\pi/a$ have the same eigenvalues. As a result, all the modes with the wave vector $k_z+m2\pi/a$, with m an integer, form a degenerate set. This means that once the band structure within one period of the reciprocal lattice is known, it is known for every wave vector. Therefore, it is only necessary to solve the Helmholtz equation with the results restricted to one period of the reciprocal lattice, also called the Brillouin zone. The Brillouin zone is formed by the wavevectors for which $ka/2\pi$ is between -0.5 and +0.5.

In figure 2.4, both the dispersion relation of a homogeneous material and of a 1D PhC are displayed in a so called band diagram, where the normalized frequency, i.e., frequency in units

15

of [2πc/*a*] is plotted versus the normalized wavevector, in units of [2π/*a*].
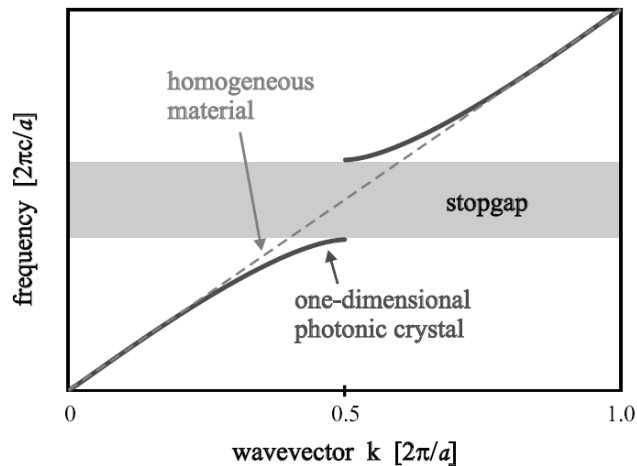

Figure 2.4 A basic illustration of the dispersion relation of a homogeneous material (dashed line) and a 1D PhC (solid line). The slope of the dispersion is $\frac{1}{\sqrt{\varepsilon}}$ for a homogeneous medium.

Note that the dispersion curve of the 1D PhC is discontinuous. Light with frequency corresponding to the shaded area cannot propagate through the PhC, which is called a stopband or stopgap. Here, no *k*-value satisfies the Helmholtz equation and no light can propagate through the crystal.

The solid black curve is the dispersion relation of a 1D photonic crystal, which is approaching that of the homogeneous material for short and large wavevectors, but in the center it differs clearly, at *k* = 0.5. There, the dispersion curves display maxima and minima. Approaching the stopband of a photonic crystal, the refractive index changes. For example, below the stopband frequencies, the refractive index is high. This is explained by the power of the electric field being located mainly in the material with the higher refractive index. Above the stopgap, the power of the electric field is located in the material with the lower refractive index.

Similar dispersion curves also appear in 2D and 3D crystals, although there the wavevector, *k,* can assume more than a single direction of propagation. If the stopgaps overlap for light propagating each direction of propagation, then a so called photonic bandgap is present. The size

of the bandgap can be used as a quantitative measure for how strongly the dispersion is modified by the photonic states. A large bandgap also means that the range over which one may design the dispersion for a particular purpose is larger.

2.1.4 Solutions in a two-dimensional PhC slab

For a 2D PhC slab, the dispersion variation can be calculated for a given periodic structure by a method that makes use of the irreducible Brillouin zone. To find solutions of the Helmholtz equation (equation 2.5) for a 2D PhC slab, only wave vectors within the unit cell of the reciprocal lattice are considered. If a particular reciprocal lattice point is chosen as the origin, the Brillouin zone is the region containing all reciprocal points that are closer to the origin than to any other lattice point.
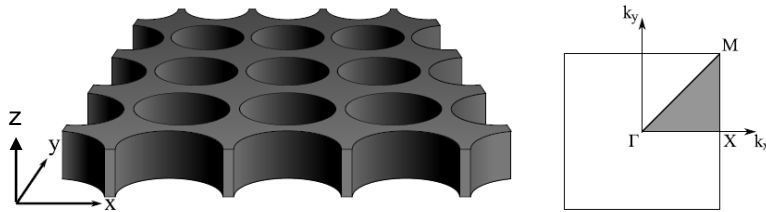

Figure 2.5 Left: schematic example of 2D PhC slab in which a square pattern of air holes has been introduced into a high refractive index material, e.g., silicon, where the light is restricted to the x and y directions by waveguiding in the z-direction. A high refractive index contrast is thereby achieved between the silicon core ($n_{Si} = 3.4$) and air holes ($n_{air} = 1$). Right: part of the corresponding reciprocal lattice and its first Brillouin zone (square area) with the irreducible Brillouin zone (shaded) limited by the high-symmetry points Γ, X and M.

Within this zone, a number of high-symmetry points can be defined. These points lie on the corners of the iBZ and are usually named Γ, X and M. Along the horizontal axes (x, y) the in-plane wavevector of the crystal, k_{II}, varies along the edge of the irreducible Brillouin zone. The high symmetry points of the irreducible Brillouin zone correspond to the following in-plane k-

17

vectors: $k_\Gamma = 0, k_X = \frac{\pi}{a}\hat{x},$ and $k_M = \frac{\pi}{a}\hat{x} + \frac{\pi}{a}\hat{y}$. These points can then be used to express all other propagation directions inside the crystal. Γ-X and Γ-M are two of those directions, and all other wavevectors are obtained by rotating from Γ-X to Γ-M.

In this picture, the dispersion relation $\omega_n(\vec{\kappa})$ in the infinitely extended momentum space can folded back onto the first Brillouin zone, by introducing a discrete mode or band index n. Mathematically, when solving e.g. (Helmholtz), this means that for all possible values of k inside the irreducible Brillouin zone, the Helmholtz equation has solutions of the form $\omega_{k,n}$, labeled by the band number n in order of increasing frequency [10]. If the wavevector k is varied over all-possible k-vectors along the symmetry points of the crystal inside the first Brillouin zone, the set of solutions $\omega_{k,n}$ for a fixed integer n constitute a band. The collection of all these bands makes up the band diagram of the crystal. A typical example of a numerically calculated band diagram for PhC slabs of the type as in figure 2.5 is shown in figure 2.6. If adjacent bands, n and $n + 1$ do not touch in the wavevector k space, then a stopgap appears.

The high symmetry points are special, because here every wave with a k-vector extending from Γ to the zone boundary gives rise to Bragg-reflected waves. For a large PhC, i.e. many holes, a wave undergoes multiple scattering as it moves through the crystal, but, because of the periodicity of the crystal, the scattering is coherent. The field then produces a standing wave field, which is a Bloch mode of the periodic structure [6, 7].

Powerful computation techniques are available to calculate the photonic modes [11], but they will not be discussed thoroughly here. Only the computational methods that were of particular use and applied in this thesis will be briefly presented in the next section.
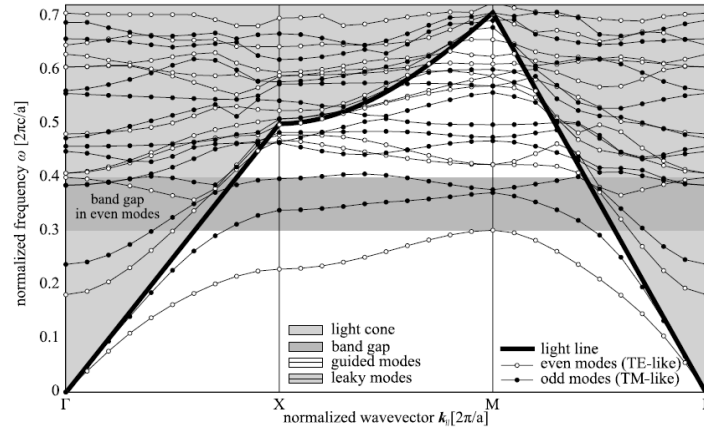
Figure 2.6 A calculated band diagram for an ideal 2D PhC slab with a square lattice of round air holes. In these calculations we used a Si slab with a thickness of 0.5 μm and with a hole radius of 0.3 μm. The shaded area, called the light cone [11], is the continuum of states when the wavevector of light is not confined to the *x-y* plane of periodicity but also contain a wave vector in the *z*-direction. The horizontal gray region indicates the stop-gap for even modes.

The band diagram presented in figure 2.6 shows as the horizontal axis, the in-plane wavevectors along a path connecting the high symmetry points *Γ-X-M-Γ*. The vertical axis is the relative frequency *ω* of the modes.

For a 2D PhC slab, the high index of the slab provides light confinement by refractive index-guiding in the *z*-direction (white area under the light cone in figure 2.6). In addition to the guided modes created thereby, and with its light distribution mainly outside of the slab, a continuum of modes (so called leaky modes) is present (shadowed area). The thick black line is called the light line, and gives the border between guided light (below the light line) and non-guided (leaky) light (above the light line) of the slab. Theoretically, in a perfectly fabricated structure, the guided modes possess an infinite lifetime, which means that there is no energy transfer with external radiation outside the slab. However, guided modes will typically encounter two-types of loss mechanisms. The first type will be the losses due to scattering from impurities and absorption of the dielectric material as is seen also in standard dielectric waveguides. The second type of losses is specific for photonic crystal slabs. These losses arise from the out of plane

19

scattering at the interfaces between the areas with different indices of refraction. These interfaces introduce possibilities for unwanted scattering due to fabrication impurities at the interface. The non-guided leaky modes possess a finite lifetime even in a perfectly fabricated structure, because they lose their energy to the background with which they overlap and thus couple. An advantage of the non-guided modes is thus that they can be investigated by reflection and transmission measurements with the PhC slab. The nature of these non-guided modes is thus an interesting key for investigating the quality of the structure, e.g., with angular reflectivity measurements. The thin lines with circles represent the solutions of the Helmholtz equation (equation 2.5) for light polarized in the plane of the PhC slab and perpendicular to the plane of the PhC slab. Furthermore, because of the lack of translational symmetry in the vertical direction, the photonic states are not purely TE or TM polarized. Instead they are called even and odd. This labeling of the modes as even and odd modes is based on a mirror symmetry argument. If one considers the electric field profiles of modes in a thin (smaller than the wavelength) dielectric structure, then at the symmetry plane ($z = 0$), the fields must be purely TE or TM polarized, which is parallel or perpendicular to the $z = 0$ plane, respectively, as shown in figure 2.7.
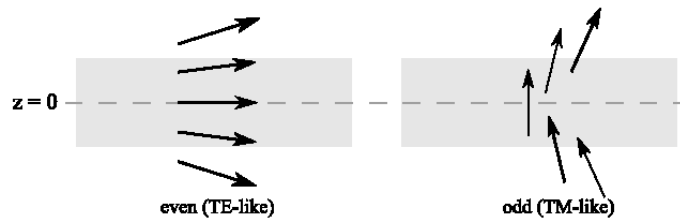

Figure 2.7: A thin dielectric structure with mirror symmetry at $z = 0$. The labeling of modes that are mostly parallel, i.e. even, with respect to the mirror plane are TE-like, the modes that are mostly perpendicular, i.e. odd, with respect to the mirror plane are TM-like.

Since the dielectric structure has a certain thickness the fields at other locations than the $z = 0$ plane can no longer be purely TE or TM polarized, but because of continuity, the field is mostly TE-like or TM-like, which is also called even for polarizations parallel or odd for polarizations

perpendicular to $z = 0$, respectively.

In order to present the band diagram of a 2D PhC, it is sufficient to calculate only the lower boundary of the light cone, since all higher frequencies are automatically included. This lower boundary corresponds to the frequency for which the in-plane wavevector of the light in the structure is equal to the wavevector of the light in the background. The lower boundary frequency in the background is simply the dispersion relation of the background, given by equation 2.7.

In summary so far, when the structural parameters of the slab structure are properly chosen, a PhC can exhibit a band gap. From calculations as shown in figure 2.6, i.e., for a square lattice of holes with the dimensions stated above, one finds a range of frequencies in which no guided modes exist. For the type of 2D PhC considered, in the normalized frequency range 0.30 - 0.39, i.e., there is no allowed frequency for any direction or value of the in-plane k-vector.

2.2 Computational modeling for 2D PhCs

In this section, the computational methods for modeling the fabricated 2D PhC sample, described in the next chapter, are briefly outlined. The structure parameters used for modeling (e.g., hole size, periodicity of the holes, thickness of the layers the PhC consists of) are in close relation to the scanning electron microscopy (SEM) observations of the fabricated sample.

A first goal of this section is to briefly introduce the theoretical modeling necessary to motivate our choice of certain structure parameters for the fabricated sample. A second goal is to present theoretical calculations of the transmission and reflection spectra, with which experimental measurements of reflection and transmission (chapters 4 and 5) can be compared.

2.2.1   MIT Photonic-Bands

There are a few computational models that are currently used to predict the band structure of dielectric periodic structures [12-16]. The results of such simulations are (besides numerical errors) exact because they numerically compute eigenvectors and eigenvalues of the Maxwell's equation in the frequency domain, such that each eigenvector and eigenvalue is mapped to an analytical mode. One of the computational models is the MIT Photonic Bands model (MPB), which calculates the band structure of the guided modes using the supercell method [17]. A supercell is the primitive cell a 3D periodic crystal is made of. The supercell is considering the PhC core and the claddings (see figure 2.8). MPB is based on the plane wave method (PWM) for obtaining guided mode solutions and their band structure. In the PWM, a hypothetic lattice periodicity is introducing a new period in the vertical direction, visualized in figure 2.8. The related Bloch waves (photonic modes in a periodic refractive index lattice can be described using a modulated plane wave with a periodic function that describes the lattice [6]) as approximated by a Fourier transform. The numerical code used, applies periodic boundary conditions in all 3 dimensions for defining a supercell.
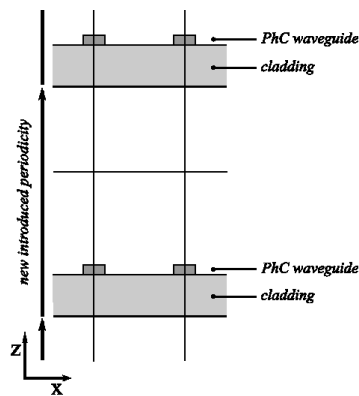

Figure 2.8 Shown is the approach of the used MPB code in which supercells are assumed (two of them shown). A larger spacing of the supercells reduces the influence on the calculated band dispersion. This allows to calculate, with high precision, only the modes distributions that are strongly localized within the PhC waveguide.

This method can be seen like a 3D calculation, where the third dimension consists of a periodic sequence of slabs. By increasing the vertical period (a few lattice constants), it is possible to decrease the coupling between the guided modes in adjacent slabs until it is negligible, such that the guided modes frequency are calculated with sufficiently high accuracy. The magnitude of the vertical wavevector is inversely proportional to the vertical period and determines the phase relationship between adjacent slabs, i.e., whether or not the guided modes influence each other's frequency. The main problem is that the coupling between leaky modes cannot be neglected, no matter what the size of the supercell is. Thus it is preferable to calculate only the guided modes with MPB, and the nonguided (leaky) modes with other methods, such as with the Scattering Matrix Method (SMM) [12], Finite Element Method (FEM) [13], Finite Difference Time-Domain (FDTD) [14-15] or RCWA (DiffractMOD) method [16]. More information and details about the weaknesses and strengths of the various models can be found in reference 18 and 19.

2.2.2 Numerical results and discussion

The band structure associated to a square lattice waveguide for TE and TM guided modes is shown in figure 2.9.

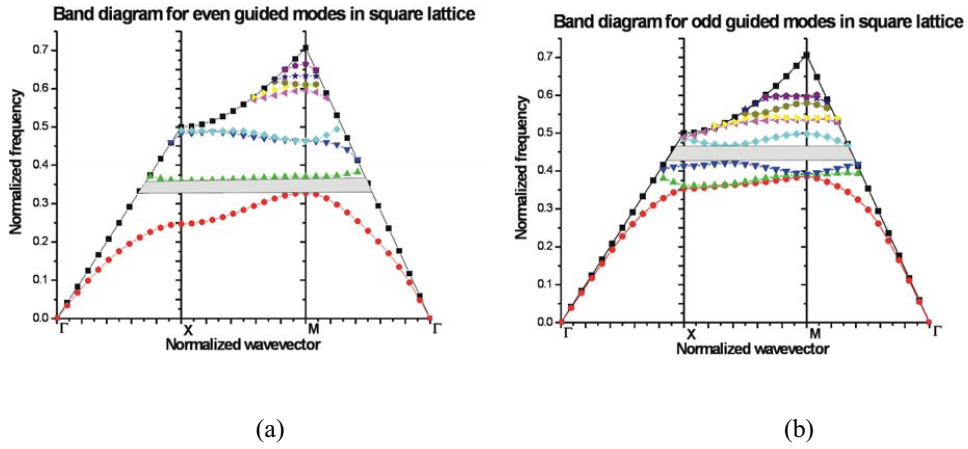<div align="center">(a)   (b)</div>

Figure 2.9 The band structure of the even and odd guided modes in a 2D Si PhC with square lattice calculated with the MPB model [20, 21, 22]. The square lattice has a period a and the radius of the air holes is $r = 0.4a$. The thickness of the slab is $0.5a$ and the dielectric constant is 12. These parameters are chosen because they are close to those used in the experiments. The band structure is calculated at discrete points (colored symbols). The colored lines represent the guided modes. The in-plane wave vector progresses from Γ to X to M and back to Γ. The gray regions represent the stopgaps.

The vertical axis displays the normalized light frequency. The horizontal axis contains the in-plane wavevectors of the crystals along the edge of the irreducible Brillouin zone. The high symmetry points of the irreducible Brillouin zone correspond to Γ with $k_{\text{in-plane}} = (0,0)$, X with $k_{\text{in-plane}} = (\pi/a)$ $(1,0)$ and M with $k_{\text{in-plane}} = (\pi/a)$ $(1,1)$. The thin lines with the differently colored symbols show the solutions of the Helmholtz equation under the light cone, i.e. guided modes confined to the waveguide slab.

The position of the light cone depends on the index contrast between the slab and the air. In particular, for higher index photonic crystals, the light cone will reach higher frequencies and more modes will be confined [23, 24].

The periodicity in the pattern of holes in the slab waveguide has the following consequences. The wavevector is limited as it is folded back into the irreducible Brillouin zone. This also splits the guided-mode bands; the guided modes are shifted to higher frequencies because high-index material is removed, which reduces the effective index of the waveguide; a frequency cut-off for the guided modes appears. In the band diagram this cut-off means that guided modes cannot be found above a certain normalized frequency, in the shown case above $c/a = 0.7$. The cut-off frequency depends only on the geometry of the lattice from which the structure is made, but it is independent of the other parameters such as the refractive index of the waveguide or the size of the holes [25]. Besides the guided modes, leaky modes can be found above the light line. These modes experience radiation losses due to diffraction out of the structure, and the associated losses can be rather different for each mode [26]. The leaky modes are not depicted in figure 2.9, but are investigated in detail in chapter 4.

In figure 2.9, one can identify several frequency intervals under the light cone, which are free of guided modes (marked by the horizontal, grey ranges), and which are photonic stop gaps. The position and size of these gaps is influenced by structure parameters. In particular, for obtaining a gap, the thickness of the waveguide must be such than only a single spatial mode is supported. Otherwise the gap would be suppressed by coupling into higher order modes [23]. Furthermore, the refractive index contrast needs to be sufficiently large (typically > 2) to open a gap and to provide strong field confinement in the vertical direction [6].

For the case that we consider, a square lattice of round holes, one of these bandgaps is found for TE polarized light in the frequency range from 0.328 to 0.361, i.e. in the mid-IR wavelength range from 2.7 to 3 µm. This range corresponds to a gap around a wavelength of 2.8 µm having a width of about 10% of its center wavelength. Close to this bandgap, the PhC guided modes show strongly anomalous dispersion. To perform nonlinear optical experiments that do not suffer from undesired two photon absorption losses, one would have to compare the photon energy at the named gap with half of the electronic bandgap of the material from which the PhC is made. Here we use silicon, in which the bandgap is approximately 1 eV. Correspondingly, a wavelength of

greater than approximately 2 μm would exclude two-photon absorption, and that the named mid-IR wavelengths at the photonic bandgap, indeed, fulfill this condition.

The band structure is also shown for TM polarized light in figure 2.9b. In this case the guided modes show a gap for light frequencies between 0.42 and 0.466. This corresponds to mid-IR wavelengths ranging from 2.17 to 2.38 μm (2.2 μm with a width of about 8%). Although these wavelengths are somewhat shorter than for the TE gap, the photon energy is till not sufficient for two-photon absorption in Si.

In the next section, the influences of the bandstructure on the PhCs reflection and transmission properties are discussed. In particular, i.e., we focus on coupling into the non-guided modes, i.e., the so-called leaky modes which lie above the light line.

2.2.3 Reflection and transmission of 2D PhC slab

Understanding the optical properties of a specifically fabricated 2D PhC slab can be achieved through a calculation of its basic, linear properties and comparison to experimental data. An experimental characterization of 2D PhC slabs can be achieved most easiest with transmission and reflection measurements using a widely tunable source. For a comparison, this has to be accompanied by theoretical calculations of the expected transmission and reflection spectra. The named method has been successfully applied to PhC slabs earlier [27, 28].

Experimentally, the dispersion of leaky modes of 2D PhC can be reconstructed based on resonant coupling in reflectivity as a function of wavelength and incidence angle as is shown in fig. 2.10. For a given wavelength (i.e., photon energy), resonant coupling occurs, when the in-plane component of the incident wave vector matches the wavevector of a corresponding photonic mode. If the light reflected off the sample surface is measured as a function of wavelength, such coupling can then be identified as a resonance feature (e.g. a peak or dip) in the reflected spectrum. By recording such spectra for a number of angles of incidence, thereby varying the in-plane component of the incident wave vector, particular points of the photonic band structure can be probed, and the dispersion curves of leaky modes can be mapped.
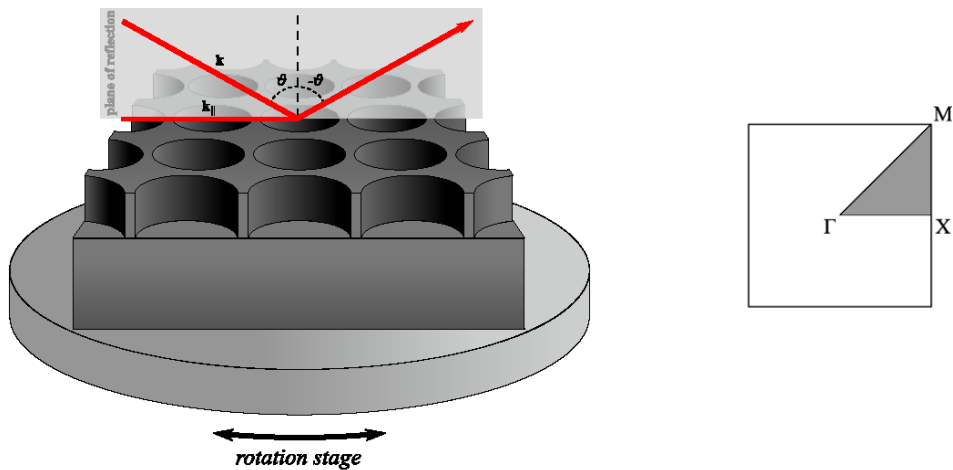
Figure 2.10 Left: Schematic geometry used to measure angle-dependent reflectivity spectra. A collimated white light beam (*k*) is incident under an angle +θ onto the PhC slab, which determines the magnitude of the in plane wave vector component, k_{II}. The reflected spectrum is measured under an angle -θ by a detector behind a spectrometer or monochromator. Right: The symmetry directions of the crystal, such as ΓM or ΓX, can be accessed by rotation of the crystal, such that particular resonances shift in wavelength and dispersion curves of the leaky modes can be accessed.

When recording the bandstructure however, there is a restriction, namely only the projection of the wavevector onto the plane of the slab can be coupled to the PhC modes. As a consequence, the in-plane wavevector of the incident light which is available for such coupling is reduced with respect to the wavevector of the light in surrounding air by a factor sin(θ), where θ is the angle of incidence, and where λ_{air} is the wavelength in air;

$$k_{II} = k \sin \theta = \frac{2\pi}{\lambda_{air}} \sin \theta \qquad (2.8)$$

A variation of θ (between 0° and 90°) in equation 2.8 shows, that the magnitude of the component of the wavevector parallel (k_{II}) to the surface can never match that of a guided mode, because the guided modes lie below the light line (defined by setting $\theta = 90$ in equation 2.8). This excludes the direct probing of the dispersion of guided modes via simple reflection measurements. Rather one expects a coupling only to the leaky modes (named also quasi-guided modes or guided resonances) because these lie above the light line and can thus be accessed with a suitable combination of light frequency, polarization and angle of incidence. The suitable combination of these parameters depends on the exact band structure of the crystal and a prediction is possible only with numerical methods that calculate the spectral response in reflection.

The required numerical modeling is, actually, rather similar to what is required in modeling diffraction from plane objects showing a spatial periodicity, such as diffraction gratings made from transparent dielectric materials (phase gratings). Correspondingly, many numerical methods are available for analyzing diffraction, and which can also model the situation of interest here, where light is incident under an oblique angle onto a 2D PhC slab. Examples are the so-called vector diffraction theory [29], the vector modal method [30] or C methods [31] which are analyzing diffraction from spatially periodic structures [32]. These methods, which have been treated in several reviews [33-35], all use the wave equation for a calculation of the electromagnetic field inside the grating, to determine the diffracted or reflected field outside the grating. Since a full treatment about all available methods goes far beyond the scope of this thesis, we restrict ourselves only to two models used in our evaluation of 2D PhC, namely the rigorous coupled wave analysis (RCWA) [32] and a finite-difference time-domain (FDTD) method.

2.2.4 Two-dimensional PhC grating diffraction

The analysis of light diffraction in this work is done with the RCWA, for which we use a

software code called DiffractMOD [36, 37]. The code uses a computer-aided design (CAD) user interface. The model calculates the diffraction of electromagnetic waves from a large variety of different geometries. It implements several advanced algorithms together with a fast converging formulation of scalar wave equations (Helmholtz equation, expressed by equation 2.5), which takes into account Fresnel reflection at the layer interfaces.

When an electromagnetic wave with arbitrary polarization is obliquely incident upon a 2D PhC there will be simultaneously both forward-diffracted (transmitted) and backward-diffracted (reflected) waves. The general approach to the 2D PhC-grating diffraction problem involves finding a solution to the wave equation at each interface of the structure and then these independent solutions are adjusted to match at their common interfaces. RCWA considers that there exists common boundary condition between layers, such as so-called perfectly matching layers (PMLs) in the computational cell, as is displayed in figure 2.11a. A PML represents a (non-physical) material that, in theory, absorbs waves without any reflection, at all frequencies and angles of incidence [38]. Materials and waves adjacent a PML can then be interpreted as ongoing at the outside of the computational cell.

Figure 2.11a shows a graphical representation of a computational cell filled with an index distribution as given by the corresponding component materials, while the bottom and top end of the cell carry a PML. There are no PMLs added in the horizontal directions, because the index materials are considered to repeat periodically and infinitely in the horizontal *xy*-plane. A square lattice that is periodic with the size of the computational cell is then constructed. Inside the computational cell of figure 2.11 the stack of materials represent a PhC slab with an asymmetric cladding (index and thickness of cladding 1 different from cladding 2). The hole in the center of the square *xy*-plane provides the refractive index modulation.
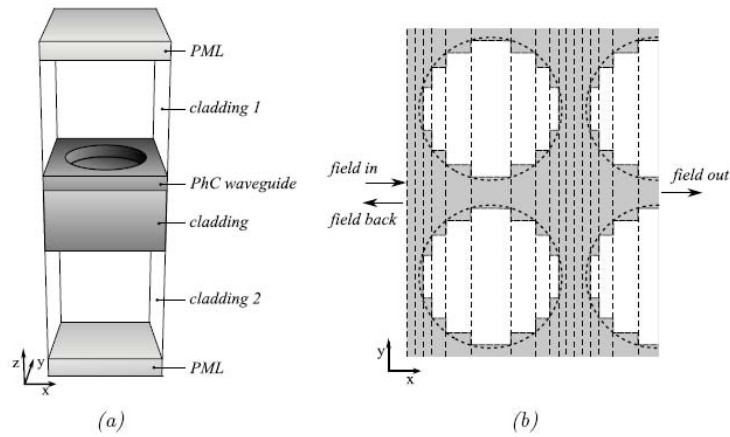
29

Figure 2.11 a) Computational cell for a 2D square lattice PhC structure. b) Slices for a Fourier expansion of the refractive index modulation in the *xy*-plane.

The RCWA method expresses the spatial variations of the refractive index as a Fourier expansion of the index as found in slices. Figure 2.11b illustrates this for the *xy*-plane. The width of slices is chosen to model the distribution of the refractive index as closely as practical with a minimum number of slices. The related input and output fields are computed by matching the boundary conditions at every slice. The fields inside a single slice are treated like diffracted waves that progress through the 2D PhC slab and couple energy between each other as they progress. The backward-traveling waves are produced both by diffraction from within the structure volume and by diffraction and reflection from the periodic boundaries of the multi-layer structure. These physical processes produce a spectrum of plane waves, which are reflected by the structure.

A limitation of this method is that the Fourier expansion introduces a discretization to the distribution of the refractive index, which leads to a staircase effect, as shown in figure 2.11b. The RCWA method in combination with PMLs and the named staircase approximation lead to complex eigenvalue problems. For these reasons RCWA is a method that is sensitive to convergence problems [18, 39, and 40].

An example of simulations result is the total diffraction efficiency, which can be promptly

calculated as the design and modeling process is completely parameterized. The term total diffraction efficiency means that a single value of the output power is calculated which is the sum of the power from all diffraction orders. DiffractMOD calculations were performed to investigate the total reflection, and also the total transmission of 2D silicon PhC.

2.2.5 Spectral reflectivity simulations

DiffractMOD uses the light polarization, geometry of incidence and the crystal lattice parameters as input and calculates the spectrum of the reflected and transmitted light. Here, for the purpose of comparison with experimental data, we present the results of calculations for the fabricated crystal to be investigated in the following chapters. The crystal consist of Si host material with a refractive index of $n = 3.4$, bond on a silicon oxide substrate ($n = 1.4$), surrounded by air ($n = 1$). The silicon layer is 0.5 μm, the silicon oxide is 3 μm thick. The square lattice has a spacing of 1 μm and consists of holes in the silicon with a diameter of about 0.4 μm. During each calculation, the wavelength is varied, but the angle of incidence is varied between calculations. The reflectivity results for Γ-M symmetry direction are shown in figures 2.12a and 2.12b, for incident light which is TE and TM polarized, respectively.
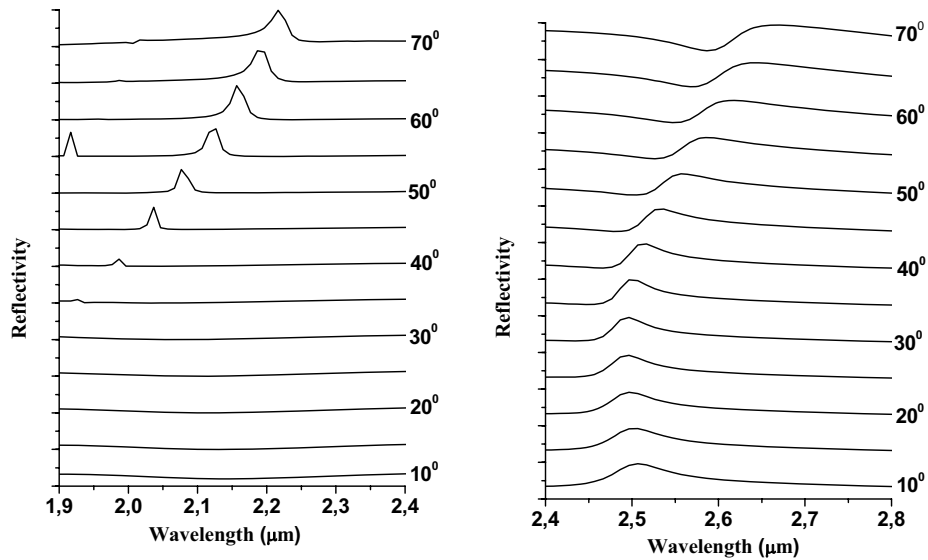
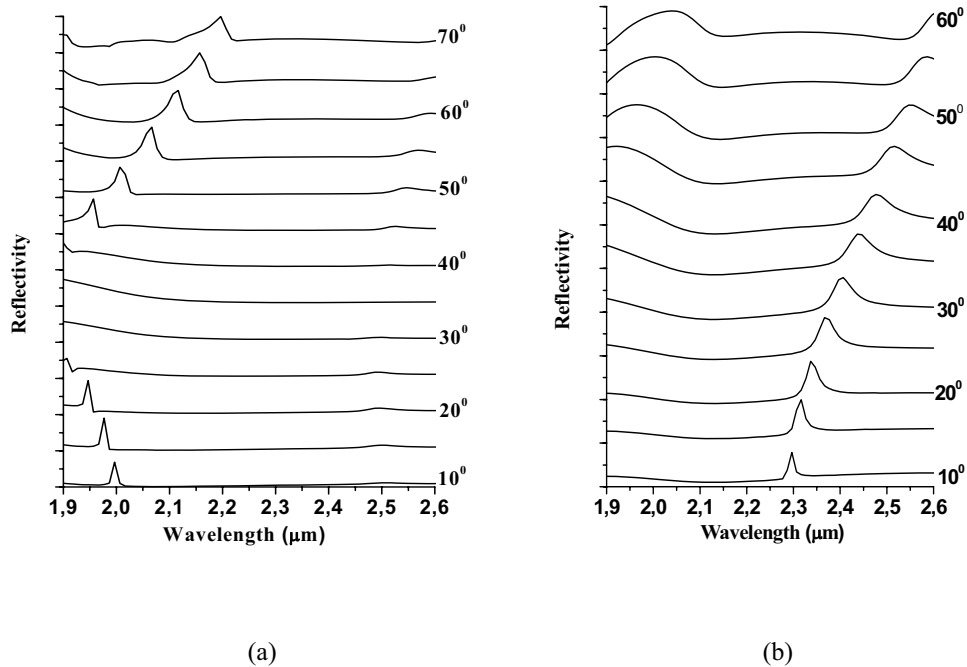(a)   (b)

Figure 2.12 Calculated reflectivity of the photonic crystal slab as a function of wavelength for propagation along Γ-M symmetry direction. The distance between the large ticks on the vertical axes correspond to absolute reflectivities between zero and unity for each trace. (a) Calculated reflectivity for TE polarized and (b) for TM polarized light. The curves are vertically shifted for clarity; from bottom to top, the angle of incidence is varied in the range from θ = 10° to 70°.

(a)   (b)

Figure 2.13 Calculated reflectivity of the photonic crystal slab as a function of wavelength for propagation along *Γ-X* symmetry direction. The distance between the large ticks on the vertical axes correspond to absolute reflectivities between zero and unity for each trace. (a) Calculated reflectivity for TE polarized and (b) for TM polarized light. The curves are vertically shifted for clarity; from bottom to top, the angle of incidence increases from $\theta = 10°$ to $70°$.

The spectra display distinct features which shift in wavelength as the angle of incidence is varied. In figures 2.12a, b and 2.13a, b one can also see some slowly varying, background-like features (e.g. in figure 2.12a at 10°, or in figure 2.13b at 40° around 2 μm). These are probably due to broadband Fresnel reflection or broad Fabry Perot fringes from the SiO_2 layer underneath the periodic structure.

In the experiments, we also measured the transmission spectra obtained with broadband light that falls under normal incidence onto the PhC. In order to enable a comparison with the expected

transmission spectra, these spectra were calculated as well, for which we used the RCWA with the same crystal parameters. The computed transmission spectrum is displayed in figure 2.14 on a wavelength range of 1.1 μm - 2.4 μm.
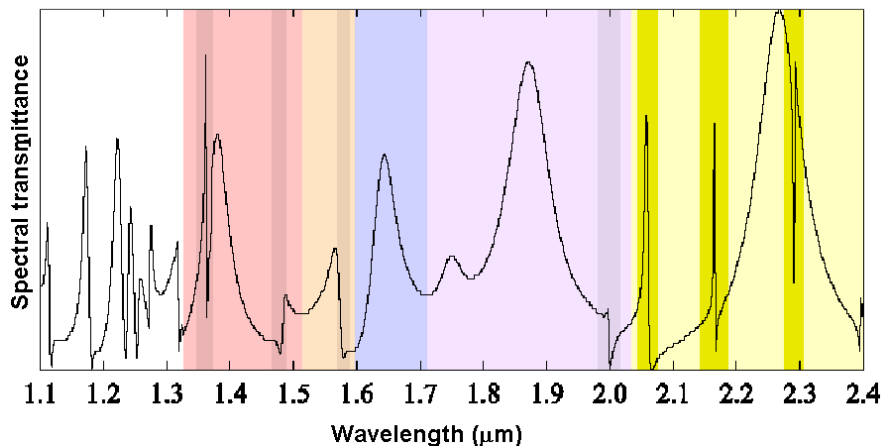

Figure 2.14 Calculated transmission vs wavelength at normal incidence for polarized light along Γ-M symmetry direction

It can be seen that the calculated spectra show a variety of different spectral features which possess different line shapes and rather different spectral bandwidths. In chapter 5 we discuss that the spectrally broad features can be addressed to Fabry-Perot (Airy) fringes caused by the layered structure of the crystal with its Si top layer, a SiO_2 buffer layer, and a Si substrate. Figure 2.14 uses colors to highlight these Fabry-Perot fringes. A closer description of such resonances will be given below in this section. In figure 2.14, in addition one finds sharper, somewhat asymmetric resonances superimposed on the Fabry-Perot resonances. In chapter 5 we show that these narrow-band features and their dispersive nature such as seen in 2.14 in the range between 2 μm and 2.2 μm wavelength, can be attributed to the photonic structure in the Si top layer.

Resonances with Fano-type line shape

A closer inspection of the line shape of the photonic resonances reveals a Fano-type of line shape

[41]. The physical explanation for this line shape is the following. The hole pattern diffracts part of the normally incident (zero in-plane wavevector) light towards the in-plane direction where, at suitable frequencies, leaky modes of the 2D PhC slab can be excited and diffractively radiate back into the normal direction. This corresponds to an additional pathway in transmission at leaky mode frequencies. The superposition of this pathway with the direct transmission then leads to the asymmetric Fano-shaped resonances [42].

For a comparison of measured and predicted spectra it is important to extract from measured Fano-line shapes the spectral bandwidth of the participating leaky mode. The importance lies in that an increased leaky mode bandwidth (experimental beyond prediction) is indicative for additional losses associated with the fabrication process of a PhC. Particularly here, where the crystal was fabricated with a novel modification of laser interference lithography (see chapter 3), it is of interest to quantify the additional, fabrication induced losses.

To extract from measured Fano line shapes the leaky mode bandwidth and also the central frequency of the corresponding leaky mode, we performed Fano-fits to the observed resonances. The line shape expression used for these fits can, e.g., be derived from Fano's publication [42], however, here we use a form which is more appropriate for resonances from photonic crystals [42].

With the frequency of the incident light, ω, and with the resonance frequency and bandwidth of a leaky mode, ω_0 and $\Gamma = \hbar\gamma$, respectively, one defines the so-called reduced energy variable, ε, in analogy to equation 19 of reference 42:

$$\varepsilon = \frac{\hbar\omega - \hbar\omega_0}{\frac{1}{2}\hbar\gamma} \, . \qquad (2.9)$$

The line shape of a Fano resonance can then be expressed as:

$$F(\omega) = F_0 \frac{(q+\varepsilon)^2}{1+\varepsilon^2} = F_0 \cdot \left[1 + \frac{q^2 - 1 + 4q(\omega - \omega_0)/\gamma}{1 + 4(\omega - \omega_0)^2/\gamma^2} \right] \qquad (2.10)$$

Here, F_0 is oscillator strength, while the so-called asymmetry parameter, q, determines the shape of the resonance and may assume values between –1 and +1. The parameter q can be regarded as a coupling parameter that quantifies how efficiently and with what phase the incident light is

reflected (or transmitted) via excitation of the leaky mode, in comparison to the direct reflection (or transmission) pathway. This is illustrated in figure 2.15 which shows how the coupling parameter q determines the line shape of the Fano function.
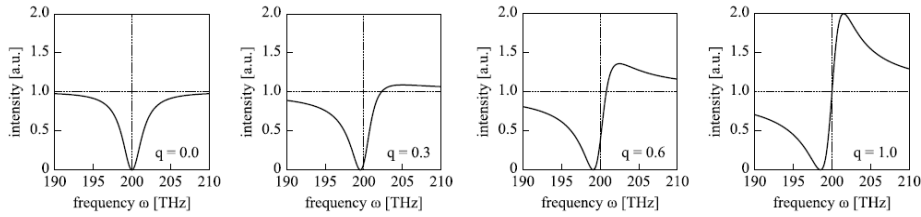

Figure 2.15 Example of Fano line shapes for $\gamma = 0.3THz, \omega_0 = 200THz$ and different q values.

When $q = 0$, this means that light reflection via a leaky mode occurs without phase shift with regard to direct transmission, resulting in a symmetric dip in the reflectivity spectrum. For higher q a resonant peak is appearing in the reflectivity spectrum and the resonances becomes asymmetric.

In chapters 4 and 5, equation 2.10 (and thus line shapes as in figure 2.15) is used as a fit function to spectral features which are either measured reflection or in transmission. In these fits the free parameters of main interest are the center frequency, ω_0, and the linewidth of the feature γ. The reason is that these yield the so-called quality factor of a measured resonance (see section 2.4) in comparison to the expected quality factor, for a quantification of fabrication losses. In contrast, the q-parameter and two additional fit parameters (an offset and a scaling factor) are provided by such fits as well, but their values are of little relevance for the quality factor of a photonic resonance.

Resonances with Fabry-Perot (Airy) type line shape

As mentioned above, the broad resonances obtained in reflection or transmission from a 2D PhC slab can be attributed to interference in the alternating layers of materials and their respective refractive indices. To recall the origin of the resulting Fabry-Perot (or Airy) fringes, figure 2.16a shows a plane wave (illustrated by rays) that enters a planar transparent layer and undergoes

multiple internal Fresnel-reflections between the two reflecting surfaces, before it is (partially) transmitted. The interference is constructive when the optical path length between the transmitted partial waves attain a phase difference φ that is an integer multiple of the wavelength. For incident light under an angle on the layer (see figure 2.16), this phase difference is a function on incident angle θ, refractive index n and thickness l of the layer:

$$\varphi = \left(\frac{2\pi}{\lambda} \right) 2nl \cos\theta \qquad (2.11)$$

Figure 2.16b shows the corresponding Fabry-Perot interferences fringes calculated in transmission as a function of wavelength:

$$T = \frac{(1-r)^2}{1+r^2 - 2r\cos\varphi} \qquad (2.12)$$

where r is the Fresnel-reflection coefficient, and φ is the phase difference.

(a)   (b)
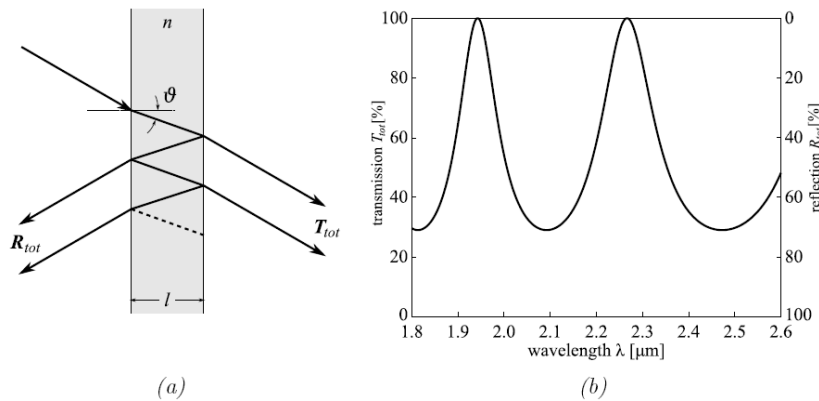
Figure 2.16 Basic principle of how a single layer creates Fabry-Perot interference fringes in transmission. (a) Light enters a planar transparent layer and undergoes multiple internal reflections. (b) Fabry-Perot (Airy) interference fringes calculated with equation 2.12 for $\theta = 0°$, reflection coefficient $r = 0.3$, refractive index $n = 3.4$ and layer thickness $l = 2$ μm. Absorption and scattering losses are neglected.

From equation 2.12, the spectral separation between the fringes in figure 2.16b becomes smaller when the light propagates through effectively more material. This creates a longer optical path length difference, which can be realized by increasing the layer thickness, the angle of incidence, or choosing a material with a higher refractive index. A change of the refractive index, however, also increases the reflection coefficients between the interfaces, which will decrease the spectral bandwidth of the transmission peaks. It should be pointed out that layers with a few microns range thicknesses lead to a rather slow variation with wavelength, to broad features that appear like a slow variation of some background spectra. The discussed Fabry-Perot type of line shapes have been previously observed with thin, air-bridged photonic crystal slabs [43] as well as with chalcogenide photonic crystal membranes [44, 41]. We note that the above mentioned RCWA model includes these Fabry-Perot line shapes as well, when the computational cell comprises the various thin layers of which a PhC is consisting.

2. 3 Leaky modes quality factors of 2D PhC slab

2.3.1 Leaky modes quality factor and losses

While a guided mode, at least in a perfectly fabricated structure, possesses an infinite lifetime and thus an infinitely small line width, γ, a leaky mode can diffractively exchange energy with light outside the slab (also called incident, reflected, transmitted light, or called background). This happens when the leaky mode is excited with a suitable in-plane wavevector of the incident light which matches the wavevectors of a leaky mode. The capability of the leaky mode to resonantly enhance light can be expressed by a corresponding lifetime or decay time, $\tau = \dfrac{1}{\gamma}$, where γ is the line width as given in equations 2.9 and 2.10. As a consequence of the finite lifetime, light that leaves a leaky mode shows a delay or phase shift which strongly depends on the excitation frequency, compared to the incident light which excites the leaky mode. This frequency dependent delay produces resonance (Fano) features in reflection or transmission spectra when the delayed leaky mode transmission is superimposed with the directly transmitted

light, because direct transmission does not generally show a strong frequency dependent delay. The width of a leaky mode resonances becomes narrower with decreasing losses in that mode, expressed by a narrower line width γ, and so does the observed Fano resonance narrow. Extracting the line width of a leaky mode resonance from a Fano fit thus provides information over the quality of the leaky mode resonance.

A widely used measure for the quality of resonances is the so-called quality factor, Q, which is defined as the ratio of the center frequency of the resonance, ω_0, and the linewidth of the resonance, γ, i.e., $Q = \frac{\omega_0}{\gamma}$. Experimentally, the center frequency of a leaky mode and also its bandwidth can be retrieved by a Fano fit as is presented in chapters 4 and 5.

From the definition of the quality factor it is evident that a perfectly guided mode shows an infinite quality factor due its infinitely small linewidth, when the corresponding PhC is fabricated without any errors. In contrast, even in a perfectly fabricated crystal, the quality factor for leaky modes is intrinsically a finite value, due to coupling to the background, the strength of which is determined by the design of the photonic structure. This intrinsic limitation of Q-value is imposed by the losses due to the out of plane diffraction produced by the pattern of holes, called intrinsic losses [45]. At a closer look, there are two physical effects which determine the amount of intrinsic losses and, thereby, the theoretical lifetime of leaky modes. Firstly, Q is influenced by the mode confinement in the vertical direction. The corresponding contribution to the total quality factor is usually labeled as Q_v. The other physical effect is associated with light that decays into the plane of the PhC slab, into the horizontal direction. This contribution is usually labeled as Q_p and depends, e.g., on the radius of the holes [46], where smaller holes increase the quality factors.

Since the two described loss mechanisms are largely independent of each, they contribute to the total Q as [47]:

$$\frac{1}{Q} = \frac{1}{Q_v} + \frac{1}{Q_p}$$

(2.13)

For instance, by increasing the number of photonic states, such as via increasing the area PhC and thus the number of holes, Q_p increases exponentially with the number of cavities formed by

the holes in the slab, while Q_v remains unaffected. Thus, in the limit of large area photonic structure, Q saturates at Q_p ($Q \approx Q_p$).

Contrary to this, experimental investigations have to rely on fabrication techniques which provide crystals only with limited size and unwanted fabrication errors. These results in an additional contribution called extrinsic losses, expressed by a corresponding quality factor Q_E, which adds inversely to the *rhs* of equation 2.13.

2.3.2 Quality factor calculations

The characterization of extrinsic losses forms an important measure to judge the quality of the fabrication technique from which the crystals were obtained. For such characterization, the total quality factor, Q in equation 2.13, can be measured via Fano fits as described above. However, the determination of extrinsic losses, Q_E, then requires that the intrinsic losses (given by Q_v and Q_p) are determined for a perfect PhC as well, i.e., by calculation of losses with a model.

To calculate the intrinsic losses for the crystal structure investigated here, we used a finite-difference time domain computational scheme [48]. In this scheme, in a first step, an initial, spectrally broadband light field is provided inside the PhC. Thereafter its decay is calculated as a function of time, which yields the decay time and frequency of the initially excited photonic modes. The code that we use [49, MEEP] calculates the propagation of electromagnetic fields as a function of space and time, by repetitively solving Maxwell's equations. Again, for this the photonic crystal is approximated by a computational cell structure, which is identical to that used in the RCWA calculations. The initial light field is generated by specifying, within a computational cell, light sources that generate light. Calculating the subsequent decay of energy in the PhC requires to define flux planes where light is detected (and to track the light propagation all the way through the designed structure). The code also performs a Fourier analysis of the superposition of the damped oscillations of the light field, to extract the PhC mode frequencies and their decay rates, or equivalently, the Q values. For the 2D PhC as described above, the calculated Q values vary from 60 to 1800 for TE modes, and from 90 to 1500 for TM modes in the spectral range between 1.1 μm to 2.4 μm, which was accessible in our

experiments.

2. 4 Conclusions and remarks

In conclusion, we have used numerical calculations to predict the complete band diagram of the investigated 2D PhC slab in the mid-IR spectral range of interest here. For both polarizations, the 2D PhC offers a bandgap at photon energies that are less than half the electronic bandgap of silicon, i.e. at wavelengths longer than 2.1 μm. In the vicinity of this bandgap, the PhC shows strongly anomalous dispersion. Via modeling, we also predict resonances in the optical reflection and transmission spectrum, which are due to excitation of leaky modes. For the investigated structure we have numerically calculated the decay times and frequencies of the relevant leaky modes which yields the theoretical upper limit for the quality factors to be expected for the investigated leaky modes.

References

[1] S. John, *Phys. Rev. Lett.* **58,** 2059 (1987)

[2] H.A. Mac Leod, *Thin-Film Optical Filters* (Adam Hilger, London 1969)

[3] R.W. James, *The optical principles of the diffraction of x-rays*, G. Bell and Sons, London (1958)

[4] A. Yariv and P. Yeh, *Photonics, optical electronics in modern communications*, Oxford University Press, New York (2006)

[5] K. Sakoda, *Optical Properties of Photonic Crystals*, Springer Series in Optical Sciences, vol.**80**, Springer-Verlag, Berlin (2001)

[6] J.D. Joannopoulos, R. Meade, J. Winn: *Photonic Crystal* (Princeton Press, Princeton 1995)

[7] H. Ibach, and H. Luth, *Solid-State Physics: An introduction to Principles of Materials Science*, Springer (1995)

[8] J.E.G.J. Wijnhoven and W.L. Vos, *Science* **281**, 802 (1998)

[9] S.G. Johnson and J.D. Joannopoulos, *Photonic Crystals: the road from theory to practice*, Springer Series (2002)

[10] N.W. Ashcroft and N.D. Mermin, *Solid State Physics* (Harcourt Brace College Publishers, New York, 1976)

[11] S.G. Johnson, S. Fan, P.R. Villeneuve, J.D. Joannopoulos, *Phys. Rev. B* **60,** 5751 (1999)

[12] D.M. Whittaker and I.S. Culshaw, *Phys. Rev. B* **60**, 2610-2618 (1999)

[13] B.P. Hiett, PhD thesis, University of Southampton, 2002

[14] M. Loncar, T. Doll, J. Vuckovic and A. Scherer, *J. Lightwave Tech.* **18**, 1402 (2000)

[15] A. Taflove, *Computational Electrodynamics: the Finite-Difference Time-Domain Method*, Artech House, Boston, 1995

[16] DiffractMOD^{TM} software packet. DiffractMOD^{TM} is a registered trademark of the Rsoft Design Group Inc

[17] C. Jamois, R.B. Wehrspohn, L.C. Andreani, C. Herman, O. Hess, U. Gosele, *Photonics and Nanostructures, Fundamental and Applications* **1**, 1-13 (2003)

[18] C. Bostan, PhD thesis, University of Twente, 2005

[19] K. Busch, *C.R. Physique* **3**, 53 (2002)

[20] T. Ochiai and K. Sakoda, *Phys. Rev. B* **64**, 045108 (2001)

[21] S.G. Johnson, J.D. Joannopoulos, *Opt. Express* **8**, 173 (2001)

[22] L. Prodan, P. Gross, R. Beigang, L. Kuipers, and K.-J. Boller, *J. Phys. D: Appl. Phys.* **40**, 5571 (2007)

[23] S.G. Johnson, P.R. Villeneuve, S. Fan, and J.D. Joannopoulos, *Phys. Rev. B* **60,** 5751 (1999)

[24] L.C. Andreani, M. Agio, *IEEE J. Quant. Electron.* **38,** 891 (2002)

[25] P.R. Villeneuve, S. Fan, S.G. Johnson, J.D. Joannopoulos, *IEE Proc.- Optoelectron.* **145**, 384 (1998)

[26] T. Ochiai, K. Sakoda, *Phys. Rev. B* **63,** 125107 (2001)

[27] M. Galli, D. Bajoni, M. Belotti, F. Paleari, M. Patrini, G. Guizzetti, D. Gerace, M. Agio, L.C. Andreani, D. Peyrade and Y. Chen, *IEEE J-SAC* **23,**1402 (2005)

[28] V. Pacradouni, W.J. Mandeville, A.R. Cowan, P. Paddon, J.F. Young and S.R. Johnson, *Phys. Rev. B* **62,** 4204 (2000)

[29] B. Kress and P. Meyrueis, *Digital Diffractive Optics* (Wiley 2000)

[30] L. Escoubas, J. Simon, M. Loli, G. Berginc, F. Flory, and H. Giovannini, *Opt. Commun.* **226**, 81 (2003)

[31] H. Ichikawa, *J. Opt. A* **6**, S121 (2004)

[32] I. Richter and P. Fiala, *Optik* **111**, 237-245 (2000)

[33] L. Solymar and D. J. Cooke, *Volume Holography and Volume Gratings*, Academic Press, 1981

[34] P.J. Russell, *Phys. Rep.* **71**, 209 (1981)

[35] T.K. Gaylord and M.C. Moharam, *Appl. Phys.* **6,** 1-14 (1982)

[36] M.G. Moharam and T.K. Gaylord, *J. Opt. Soc. Am.* **72**, 1385 (1982)

[37] M.G. Moharam and T.K. Gaylord, *J. Opt. Soc. Am.* **73**, 451 (1983)

[38] J.P. Berenger, *J. Comput. Phys.* **114**, 185 (1994)

[39] E. Popov and M. Neviere, *J. Opt. Soc. Am. A* **18**, 2886 (2001)

[40] E. Popov, M. Neviere, B. Gralak, and G. Tayeb, *J. Opt. Soc. Am. A* **19,** 33 (2002)

[41] S. Fan, J.D. Joannopoulos, *Phys. Rev. B* **65**, 235112 (2002)

[42] U. Fano, *Phys. Rev.* **124**, 1866 (1961)

[43] V. Lousse, W. Suh, O. Kilic and S. Fan, *Opt. Express* **12**, 1575 (2004)

[44] C. Grillet, D. Freeman, B. Luther-Davies, S. Madden, R. McPhedran, D. Moss, M. Steel and B. Eggleton, *Opt. Express* **14**, 369 (2006)

[45] W. Bogaerts, P. Bienstman, D. Taillaert, R. Baets, and D. de Zutter, *Optic. Quant. Electron.* **34**, 934 (2002)

[46] W. Bogaerts, P. Bienstman, and R. Baets, *Opt. Lett.* **28**, 689 (2003)

[47] H.A. Haus, *Waves and fields in electronics*, Prentice-Hall, Englewood Cliffs, chapter 7, 1984

[48] K.S. Kunz and R.J. Luebbers, *The finite-difference time domain method for electronics*, CRC Press, Boca, Raton, 1993

[49] S. Johnson, Meep introduction: http://abinitio.mit.edu

Mid-infrared characterization of two-dimensional photonic crystal slabs fabricated in silicon with laser interference lithography

Chapter 3 Fabrication of 2D PhC slabs

In the following sections, the fabrication of a silicon-on-insulator photonic crystal with an exceptionally large area exceeding 1 cm^2 is described. The method employed in this work is based on Laser Interference Lithography (LIL). We modified this already existing technique such that it now be used for processing also of high index materials, such as silicon. This was not possible before due to the large Fresnel reflectivity of these materials. Applying LIL to silicon has become possible due to the use of a novel, more reliable photoresist, and due to the use of an anti-reflection coating to prevent the otherwise strong reflection from the high-index silicon surface, which would disturb the interference pattern mandatory for LIL. Furthermore, for the first time a stable Cr mask has been employed in combination with LIL, which enabled etching of deep holes. Such holes are required for the intended massive alteration of the dispersion.

After a summary of conventional methods to fabricate PhC, the working principle of LIL is briefly explained. Then the modified LIL process to fabricate a large-are 2D PhC in Si is described in detail, and the results of the manufacturing are presented.

3.1 Common types of fabrication techniques

Encouraged by research successes and new application prospects, the fabrication technology of PhCs has developed quickly during the last decade, in turn enabling further research. Today, a wealth of different fabrication techniques exist, from which one can choose the most suitable one, depending on the type of PhC to be fabricated, and depending on the relative importance of specific properties.

Fabrication methods can roughly be divided into sequential and parallel methods. For example, electron beam lithography [1] or focused ion beam [2] are direct sequential writing methods. With electron beam lithography, a pattern is created in a layer of photoresist by 'writing' or 'printing' one hole at a time. For this, the electron beam is scanned across the surface. Similarly, a focused ion beam (FIB) can be scanned across a surface. Unlike the first method, here no photoresist patterning and subsequent etching processes are required as FIB directly removes material to form, e.g., a regular pattern in a PhC. Both methods offer the primary advantage of changing the material on a sub-micron scale. This approach of writing one hole at a time implies that these two methods are mainly restricted to small volume production, e.g., for making small-area 1D or 2D PhCs. On the other hand, they also offer the highest flexibility for designing non-periodic photonic structures, such as light guiding defect structures. A main disadvantage is that these methods are rather time consuming, even for small volume production.

For the fabrication of 2D PhCs on a larger scale, non-sequential or parallel methods are more suitable, like, for example, deep-UV lithography [3]. Deep-UV lithography is a variant of optical lithography, where the light source is of very short wavelength in order to lower the diffraction limit. Here, a pattern is imprinted on a layer of photoresist in one step by projecting a pre-defined mask (which is often created by electron-beam lithography) onto the layer with a deep-UV light source. Because of acquisition and maintenance costs these systems are only used for commercial production.

Microcontact printing is another parallel or, rather, semi-parallel technique, where a stamp, which has been patterned before (using a sequential technique like FIB), is used to copy that pattern onto the sample surface. The transferred substance works as a photoresist. The pattern can be printed onto the surface repeatedly using a wafer stepper, which would enable the fabrication of large-area structures.

Microcontact printing enables the fabrication of a variety of patterns using a single stamp, e.g., by repeatedly stamping after slight rotation of the sample. The latter has been demonstrated successfully to fabricate sub 500-nm features [4].

Note that, in case of fabricating a PhC with a sequential technique, the accuracy of the periodicity and also the spatial range over which periodicity can be maintained is determined by the accuracy of the scanning process, which is inherent to the sequential writing methods. This is

also true for the parallel methods described here as they all rely on masks produced by a sequential writing process. The accuracy of stamping may be further deteriorated due to the fact that this is a two-step process. Finally, holographic methods should be named as additional parallel techniques, which allow the fabrication of holographic structures [5].

In this work, we concentrate on the fabrication of a large-area 2D PhC with a well-defined periodicity for altering the light propagation in the mid-infrared, at photon energies well below the two-photon absorption of silicon. A suitable parallel method for the fabrication of large-area PhCs is laser interference lithography (LIL). LIL is based on imprinting a pattern on a layer of photoresist, which is generated on basis of the interference pattern of a UV laser light beam. LIL offers two significant advantages. The first is a highly accurate periodicity due to the coherence of the used laser. The second is that LIL should enable generation of regular patterns over a relatively large area (order of cm^2) in a single step and should thus facilitate the fabrication of large-area 2D PhCs with improved large-range periodicity. In comparison with sequential methods, LIL is also time-saving and cost-efficient. On the other hand, the application range of LIL is smaller, as the use of an interference pattern leads to a limited choice of 2D structures (cubic and triangular hole structures). More complex structures can, however, be created by combining LIL with a sequential writing technique, such as FIB, to add defects to a pre-made periodic structure [6].

LIL has so far rarely been applied to fabricate structures made from high index materials due to some technical difficulties. First, if PhCs with high index contrast are to be fabricated (such as from Si or GaAs), the high Fresnel reflectivity of the substrate causes standing wave patterns in the resist, which results in an unwanted and usually detrimental vertical modulation of the desired resist pattern. The successful application of LIL to high index materials therefore would require the suppression of such standing wave patterns. Second, the etching depth into slowly etching substrates is limited, if the resist patterned by LIL is used as the etch mask itself. Rather, it would be desirable to first transfer the resist pattern into a stable mask (such as Cr) before etching into the substrate. In the work presented here, we applied both, a novel anti-reflection coating and an intermediate Cr layer to successfully use LIL for the first time to fabricate a large area PhC from Si. With this method we could etch holes as deep as the Si layer was thick, 0.5 µm in our case. In the following, the working principle of LIL as well as the modifications of the

47

process, which enabled the fabrication of this particular PhC, are described in detail.

3.2 Working principle of Laser Interference Lithography

The interference pattern required for LIL is generated using Lloyd's mirror setup [7], which is displayed in figure 3.1.
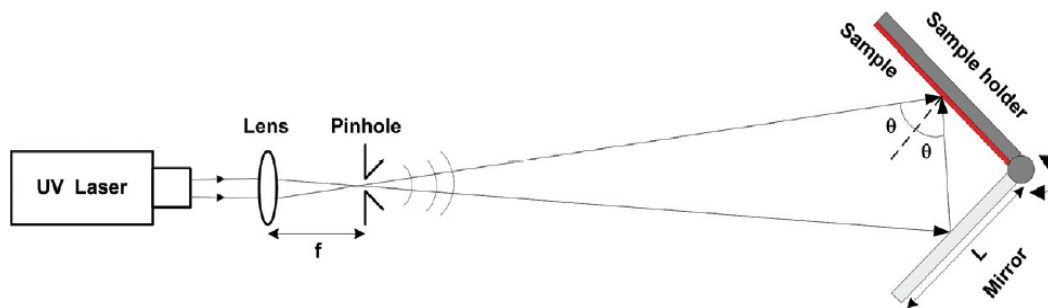

Figure 3.1 Lloyd's mirror interferometer setup.

In this setup, the beam from a continuous–wave UV Ar-ion laser (Spectra Physics, wavelength 363.8 nm) is expanded and spatially filtered using a lens with a focal length of 20 mm and a pinhole with a diameter of 10 μm positioned at the focus. In a distance of 2 m from the pinhole and over small transverse ranges there (cm's), which can be regarded as the far field, the beam forms, to good approximation, a plane wave with a measured intensity of 90 μW/ cm^2. At this position, the sample is mounted in a holder together with a highly reflecting mirror. The angle between sample and mirror is fixed at 90 degrees. One part of the UV plane wave is directly incident on the sample, while a second part is reflected off the mirror before it arrives at the sample. The overlapping two plane waves on the surface of the sample then form, a one-dimensional periodic interference pattern (stripes) at the wafer surface. To avoid a temporal instability of the interference pattern as caused by acoustic vibration and air turbulence, an electronic fringe locking system was employed [8].

The period, *a*, of the stripes pattern can be adjusted by tilting the complete mount holding the sample and mirror and is given by:

$$a = \frac{\lambda}{2\sin\theta} \qquad\qquad (3.1)$$

where λ is the wavelength of the laser light, and were θ is the angle of incidence with respect to the sample surface normal. The smallest period that can be theoretically obtained occurs for $\theta = 90^{\circ}$ and is equal to $\lambda/2$.

A silicon-on-insulator (SOI) wafer with a layer of negative photoresist on top is placed in the sample holder. Using Lloyd's mirror configuration with an angle of $\theta = 11^{\circ}$, a stripe pattern with a period of 1 μm is generated. A two-dimensional pattern is achieved by illuminating the sample with this stripe pattern two times and by rotating the sample around the surface normal between illuminations. For example, a square pattern and a triangular pattern are obtained by rotating the sample by 90° and by 60°, respectively. The exposure time before rotating the sample for a next exposure was chosen such that a single exposure does not suffice to reach the threshold for a photochemical reaction in the resist, but that a sufficient exposure is only reached with illuminating the resist a second time, after the wafer sample has been rotated.

3.3 Modified fabrication process and results

The LIL fabrication process developed by us uses an additional antireflection coating (ARC) that suppresses standing wave induced pattern deformation in the resist. Furthermore, we transfer the resist pattern obtained with LIL into a Cr mask, which allows for high etching depths in the substrate. These advantages allow to fabricate highly periodic, high contrast Si 2D PhCs with sizes in excess of a cm^2, as will be presented below.

Figure 3.2 shows an overview of the involved fabrication steps. Starting point for the fabrication of 2D PhCs is a commercially available SOI bulk wafer [9] with a 1.5 μm thickness of the Si top layer. This high index top layer ($n \approx 3.4$ @ $\lambda = 2.5$ μm) is mono-crystalline and is separated from the 522 μm thick Si wafer substrate by a 3 μm thick silicon oxide layer with low index ($n \approx 1.4$) to ensure that the light propagating in the silicon top layer would not be influenced by the high

index silicon substrate. In the SOI based PhC slab that is to be fabricated, the silicon top layer shall act as the core layer containing the photonic structure. Within this layer, the 2.5-μm light should be confined to the plane by classical slab waveguiding in the silicon layer, where the surrounding air on one side, and the silicon-dioxide layer on the other side act as cladding layers. To ensure guiding of only the fundamental mode, the silicon layer should not be thicker than about 0.5 μm, so the first step of the PhC fabrication process is to reduce the thickness of the Si top layer with chemical and mechanical polishing and reactive ion etching (RIE). After this step the surface roughness is less than 3 nm (RMS), as measured by atomic force microscopy and scanning electron microscopy (SEM). A mixture of hydrochloric acid and water, followed by oxygen plasma etching is used to clean the surface. After that, a 25 nm thick Cr layer is deposited on the silicon top layer using an electron beam physical vapor deposition process, and an antireflection coating (ARC) layer is spin coated on top of the Cr layer. As the ARC layer, Barli II [10] was used, which is a polymer doped with light-absorbing dye. Theoretical reflectivity calculations (based on matrix formalism for thin layers [10]) show that a Barli II thickness of 200 nm would result in a reduction of the light amplitude reflected off the Cr layer by a factor of approximately 10. This is sufficient to largely suppress standing wave patterns during the LIL illumination. To achieve this thickness of the Barli II layer, the spin speed was set to 3000 rpm for 30 seconds, and the viscosity was adjusted by adding an appropriate solvent (ethyl 3-ethoxypropionate and methyl 3-methoxypropionate). A pre-bake step at 200^0 C for 60 seconds is implemented to drive off the remaining solvent. Finally, a 0.9 μm thick resist layer consisting of Clariant TI09 XR [11] is spin coated at 3000 rpm for 30 seconds. Clariant TI09 XR is a prototype image-reversal resist, which contains a photoactive compound that reacts to relatively broad band UV light from 310 to 440 nm. It is expected, that Clariant TI09 XR should result in significantly lower number of photonic defects than other, commonly used resists, which would make it particularly suitable for photonic applications. The fully prepared wafer is shown in figure 3.2.

resist
ARC
Cr
Si
SiO$_2$
Si

Si 2D PhC
SiO$_2$
Si
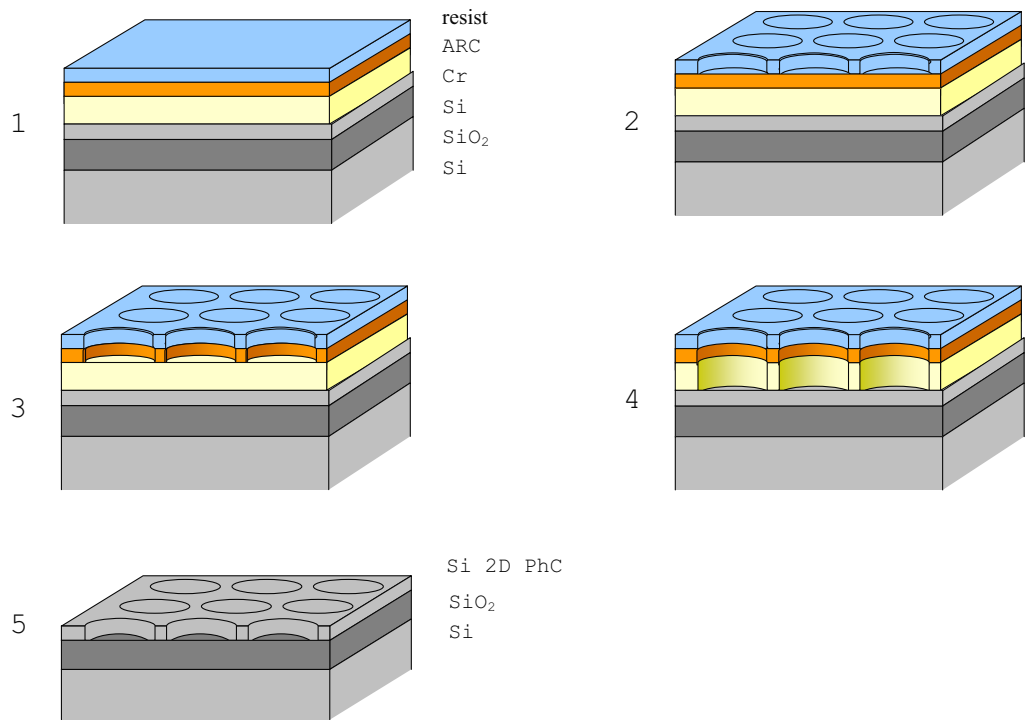
Figure 3.2 Sequence of the steps performed for fabrication of 2D Si PhCs from a SOI wafer (layer thicknesses not to scale): (1) a photoresist layer (0.9 μm) on top of an ARC layer (0.2 μm), Cr (0.2 μm), Si (0.5 μm), SiO$_2$ (3 μm), and a Si wafer, is patterned into a large-area hole structure with LIL. (2) After LIL exposure, heating, flood exposure and resist development, the non-exposed photoresist is removed, leaving a hole structure; (3) thereafter follows reactive ion etching into the ARC layer, so that the ARC layer under the holes is removed. (4) After wet etching into the Cr layer, the chromium layer under the holes is removed with a diluted chromium wet etch solution to have more control over the etch speed. (5) Reactive ion etching into the Si top layer of the SOI wafer. Afterwards, the chromium layer is removed with pure chromium wet etch.

After the LIL exposures, the wafer is heated to a temperature of 125$^\text{o}$ C for 120 seconds. At such

elevated temperature, the constituent of the photoresist, which has received its threshold UV dose, becomes permanently insoluble in the developer. Then, the photoresist is exposed for 30 seconds to light from a UV lamp (flood exposure) at an intensity of approximately 12 mW/cm^2, followed by flushing in AZ 400K developer [11] for 20 seconds, after which the non-exposed photoresist has been removed (see figure 3.2).
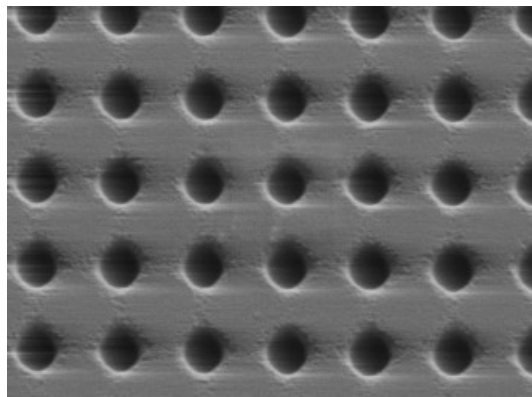
Figure 3.3 SEM micrograph of the structured image reversal photoresist (the image size is approximately 4 μm x 6 μm). This example shows a square pattern of round holes, obtained with two LIL exposures and intermediate 90° – rotation. The measured periodicity is 1 μm.

The resulting resist structure has been recorded with a scanning electron microscope and is shown in figure 3.3. The structure covers an area of about 1 cm^2 and consists of a square array of holes with an excellent 1 μm periodicity (measured error less than 1 %). The shape of the photoresist holes is round and uniform, with a measured size polydispersity of less than 6 %. In the micrograph, no defects could be detected within the whole 1 cm^2 area, which demonstrates an extraordinary reliability of the novel photoresist Clariant TI09 XR and LIL technology.

After creating the holes structure in the resist, reactive ion etching (RIE) is performed for 2 minutes to transfer the hole pattern into the ARC layer (see figure 3.3). Care is taken that the AR coating is removed completely from within the holes. This is checked via a local chemical

element analysis of the surface using a SEM equipped with energy dispersive X-ray analysis. After that, Cr wet etching is performed to transfer the hole structure into the Cr layer, where the photoresist- and ARC double-layer acts as the mask (see figure 3.4).

Figure 3.4 shows an SEM image of the correspondingly patterned chromium mask on top of the SOI wafer.
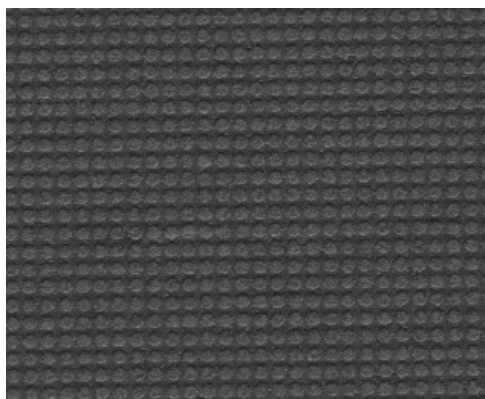
Figure 3.4 SEM micrograph of the Cr layer with the holes on a square grid (the image size is approximately 22 μm x 28 μm).

From the SEM micrograph it can be seen that the shape of the holes remains round, but the diameter of the holes is increased by about 10 % compared with the previous pattern in the resist layer (figure 3.3), due to the isotropic nature of the wet etch. Finally, the pattern of the Cr layer is transferred into the Si top layer by etching for 10 minutes with an ion-etching recipe based on oxygen and CHF_3. The etch depth is adjusted to a value of 0.5 μm via the O_2 flow (5 sccm) and the CHF_3 flow (25 sccm). Finally, the residual chromium is removed with a wet etch solution of $HClO_4$ (10 ml), $Ce(NH_4)_2(NO_3)_6$ (33 gr), and H_2O (400 ml).
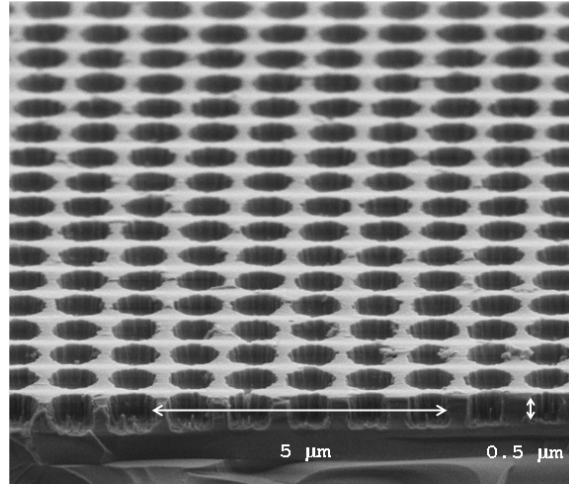
Figure 3.5 SEM micrograph of the square hole-structure in the 0.522 μm thick Si top layer of the SOI wafer. The total covered area is about 1 cm^2, which contains more than 10^8 holes in silicon. The holes are spaced by 1 μm and have a depth of 0.5 μm.

Figure 3.5 shows a side-view SEM image of the resulting 2D PhC sample, which was cut out of the exposed area with a diamond saw. The PhC shows a periodic square hole structure in the 0.5 μm thick Si top layer. The layer thicknesses and hole depths were measured with SEM at a side surface after cutting the sample. The measured periodicity of the structure across its entire area of 1 x 1 cm^2 is 1 μm with a polydispersity of the hole diameter of less than 6 %.

3.4 Conclusions

In conclusion, the existing method of LIL was modified in a novel manner, such that it can be applied to fabricate large area, two-dimensional photonic crystals in slabs made of the high index material silicon. A key advance in this work is the use of an antireflection coating between the Si substrate and the photoresist layer to minimize reflection-induced blurring of the pattern, which otherwise would occur during exposure of the photoresist. Second the use of an intermediate Cr

mask allows to deeply etch the Si layer. The described modification led to the fabrication of a 2D Si PhC with a square hole pattern over an exceptionally large surface of 1 cm^2. Inspection of the PhC with SEM showed an excellent periodicity and a very good roundness of the holes. It can be expected that this process can easily be adapted for fabrication of 2D PhCs also in other high index materials, such as GaAs, or even metals.

References

[1] T. Krauss, Y.P. Song, S. Thoms, C.D.W. Wilkinson and R. De La Rue, *Electron. Lett.* **30**, 1444 (1994)

[2] A. Chelnokov, K. Wang, S. Rowson, P. Garoche and J.M. Lourtioz, *Appl. Phys. Lett.* **77**, 2943 (2000)

[3] W. Bogaerts, V. Wiaux, D. Taillaert, S. Beckx, B. Luyssaert, P. Bienstman and R. Baets, *IEEE J. Sel. Top. Quant. Electron.* **8,** 928 (2002)

[4] Y. Xia and G.M. Whitesides, *Langmuir* **13** (7), 2059 (1997)

[5] M. Campbell, D.N. Sharp, M.T. Harrison, R.G. Denning, and A.J. Turberfield, *Nature* **404**, 53 (2000)

[6] L. Vogelaar, W. Nijdam, H.A.G.M. Wolferen, R.M. Ridder, B. Segerink, E. Flück, L. Kuipers and N.F. Hulst, *Adv. Mater.* **13,** 1551 (2001)

[7] M. Born and E. Wolf, eds., *Principles of Optics*, 5th ed., Pergamon, New York, 1975

[8] S. Kuiper, H. Wolferen, R. Cees, W. Nijdam, G. Krijnen, M. Elwenspoek, *J. Micromech. Microeng.* **11**, 33 (2001)

 [9] SOITEC, Parc Technologique des Fontaines, 38190 Bernin, France

[10] R.M.A. Azzam and N.M. Bashara, *Ellipsometry and polarized light*, Elsevier Science Publishers, 1987

[11] Microchemicals GmbH, Schillerstrasse 18, D – 89077 Ulm, Germany

Mid-infrared characterization of two-dimensional photonic crystal slabs fabricated in silicon with laser interference lithography

Chapter 4 Spectral investigation in reflection of large-area 2D silicon PhC slabs. Resonant coupling of mid-IR radiation to photonic band structure slabs.

After the LIL fabrication of a silicon 2D PhC slab for mid-infrared wavelengths (previous chapter), in the following, we describe a first step of optical characterization of the crystal in their wavelength range. Part of the motivation for such characterization, also in comparison with the theoretical expected shape of dispersion curves (band diagram) is to prepare for the nonlinear optical phase switching experiments in the MIR spectral range, as will be presented in chapter 6. In order to retrieve the dispersion curves of the slab in the range from 1.9 to 2.8 μm, angular dependent infrared reflectivity measurements have been carried out. The center frequency of the observed resonance features is used to reconstruct the band structure and to identify a suitable bandgap and the dispersion required for nonlinear optical experiments in the MIR spectral range. In addition, the quality factors of the leaky modes are determined from the bandwidth of the observed features. The value obtained for Q-factors is of general interest, as such value would be the first quantitative measure of the optical quality of a high-index PhC sample manufactured with LIL.

This chapter is organized as follows. It introduces the principle behind spectral investigations of the reflectivity of the crystal. Then the detailed experimental setup consisting will be presented, followed by the experimental results and analysis.

4.1 Introduction of the reflectivity experiment

In order to determine the dispersion of the LIL fabricated crystal, a commonly used method is employed, which is based on the variation of resonant coupling between external radiation and leaky modes of the photonic structure as the angle of incidence is varied [1].

The calculations, which have been described in chapter 2, indicate that mapping the dispersion curves of the leaky modes would require a light source that covers the spectral range of 1.9 to 2.8 μm. In order to provide the proper wave vector range, the angle of incidence, must be varied between 10° to 70°. The divergence of the incident beam is then the limiting factor for the precision: a distribution over a range of angles of incidence will result in a distribution over a range of projected wavevectors and will ultimately, limit the resolution, with which the coupled wavevector can be determined and, consequently, the contrast between spectral features in the reflectivity spectra. Furthermore, the probe beam shape should be adapted to homogenously illuminate a large portion of the PhC structure, such that a single measurement averages the response from a large surface area, thereby testing the long-range periodicity. A clear advantage of the large area of the crystal is that a large probe beam cross section can be used which increases the average detected power and thus also the signal-to-noise ratio. Figure 4.1 shows the experimental setup.
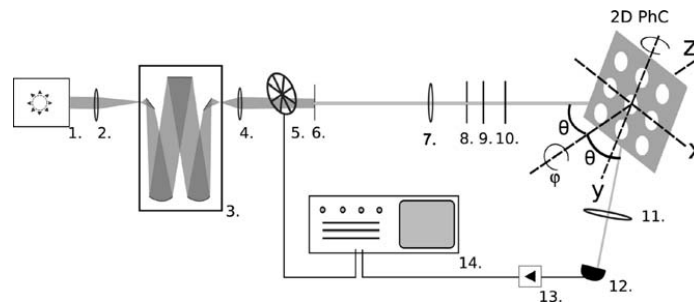
Figure 4.1 Experimental setup for specular reflectivity measurements. The individual components are: 1, QTH light source; 2, lens; 3, monochromator; 4, lens; 5, optical chopper; 6, slit; 7, lens; 8, pinhole; 9, low-pass filter; 10, polarizer; 11, lens; 12, detector; 13, amplifier; 14, lock-in amplifier.

As a broad-bandwidth light source, a 250 W quartz tungsten halogen (QTH) lamp (Oriel 66995) is used, driven by a stabilized current supply. This white-light source has a spectral power of more than 3 mW/nm over the wavelength range from 1.9 to 2.8 µm. The white light is spectrally filtered using a 300-mm monochromator (Hilger and Watts) with a grating of 750 lines/mm blazed for the MIR. For efficient throughput, the filament of the QTH bulb is directly imaged onto the entrance slit of the monochromator using a CaF lens with a focal length of 300 mm, a diameter of 50 mm, and a NA chosen to match the acceptance angle of the monochromator. Entrance and exit slits of the monochromator are both set to a width of 0.75 mm. The light emerging from the monochromator is collected and focused onto a slit with 5 mm width with a lens of 150 mm focal length and 25 mm diameter. The slit is then imaged onto the PhC using another lens of 500 mm focal length and a pinhole to remove off-axis stray light. Using a wire-grid polarizer, the polarization is chosen to be either parallel or perpendicular to the plane of reflection, i.e., we choose either transversal-electric (TE) or transversal-magnetic (TM) polarized light. Finally, a high-pass optical filter is used to remove light transmitted through the monochromator in higher orders.

With this experimental setup, a wavelength tunable mid-IR light beam is generated, which illuminates the PC sample with the following characteristics: the power in front of the sample is approximately 2 nW, with a spectral bandwidth of 5 nm. The beam divergence is estimated to be 3°, which translates into a wavevector error ranging from less than 30 % for the smallest angle of incidence, $\theta = 10°$, to less than 2 % for $\theta = 70°$. The beam cross section is of rectangular shape with dimensions of 2 mm by 5 mm, such that, even at high angle of incidence (up to 70°) the projection of the beam cross section is entirely within the 100 mm^2 area of the sample. This represents a compromise between the wave vector resolution, the spectral resolution, and the signal-to-noise ratio. Narrowing the monochromator slit width, for example, would improve the spectral resolution, but it would also increase the beam divergence and, thus, decrease the wave vector resolution, and it would decrease the available power and, consequently, reduce the signal-to-noise ratio.

The sample is mounted on a rotation stage and rotated around the surface normal, such that the direction of the in-plane wave vector of the incident light, i.e., the projection of the wave vector

on the sample surface, is along one of the two symmetry directions ΓM and ΓX of the square lattice, i.e., along the directions connecting the symmetry points Γ and M, and Γ and X, respectively. The desired orientation is verified by inspecting the mounted sample with a microscope. A second rotation stage allows the variation of the angle of incidence, to change the in-plane component of the incident wavevector.

The light reflected off the PhC surface is weak, of only nW power level, and it is in a spectral region where detectors with low noise and high quantum efficiency are not readily available. Nevertheless, even small changes in reflectivity can indicate coupling to a leaky mode. Therefore, to increase the high signal-to-noise ratio, a sensitive MIR detector is combined with a powerful and low-noise amplifier as follows. After reflection off the surface of the sample, the light passes a rotating-disc optical chopper with the chopping frequency set to 3.5 kHz, and is projected using a lens of 100 mm focal length on the detector. As a detector for the MIR radiation, a photoconductive PbS detector is used (OEC GmbH, model A5-0-3), which is carefully protected from surrounding light as well as from stray light originating from the white-light QTH source. To maximize the detector efficiency, a bias voltage of 110 V is applied to the photoconductive detector. For increasing the signal, a differential pre-amplifier followed by an integrating amplifier was used. This also eliminates the DC component of the signal and ensures that the differential amplifier operates in the linear regime. The designed circuit is designed similar to the one described in reference 4. The detector signal is processed using a lock-in amplifier (Princeton Applied Research Corp., Model 129A). The resulting signal-to-noise ratio is 25 at nW power levels and is, thus, suitable to record weak changes in reflectivity from the PhC surface.

4.2 Results and discussion of the specular reflectivity spectra

4.2.1 Reflectivity spectra

Specular reflectivity spectra are obtained along the ΓM symmetry direction, and along the ΓX symmetry direction for two perpendicular polarizations of incident light, and for angles of incidence varying between $\theta = 10°$ and $70°$. The spectra of the reflected light were normalized to the spectra of the QTH light source, obtained by placing the detector on the sample position.

In figure 4.2, the absolute reflectivity of the photonic crystal slab along ΓM symmetry direction is displayed for TE polarized (in plane of reflection, figure 4.2a), and TM polarized (perpendicular to the plane of reflection, figure 4.2b) as a function of wavelength by the black curves. In both figures, the angle of incidence, θ, increases from bottom ($\theta = 10°$) to top ($\theta = 70°$).
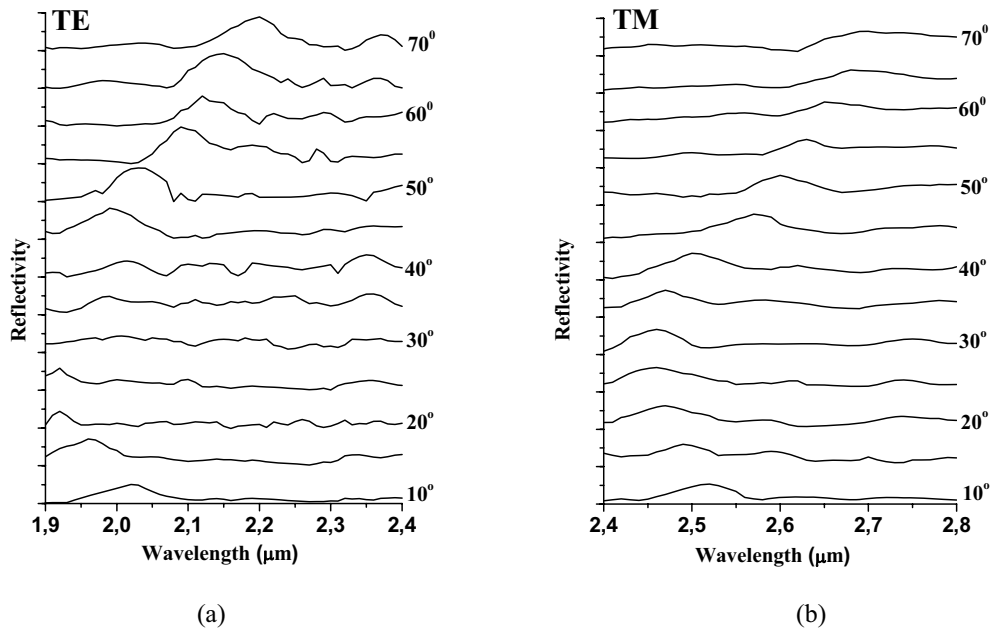

(a)   (b)
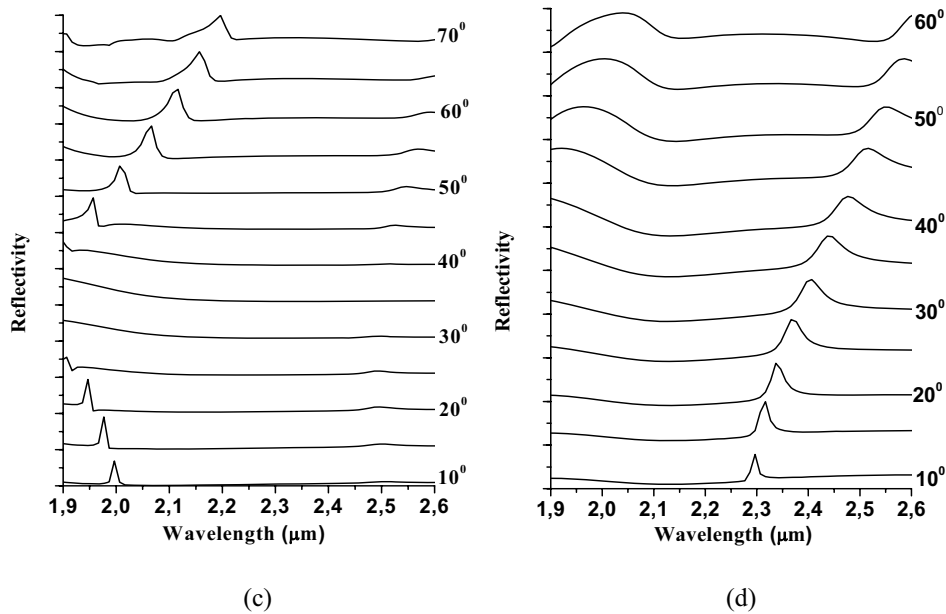
Figure 4.2 Reflectivity of the photonic crystal slab as a function of wavelength for propagation along Γ-M symmetry direction. The distance between the large ticks on the vertical axes correspond to absolute reflectivities between zero and unity for each trace. (*a*) Measured reflectivity for TE polarized and (*b*), for TM polarized light. The curves are vertically shifted for clarity; from bottom to top, the angle of incidence increases from $\theta = 10°$ to $70°$.

Both sets of spectra show sharp features superimposed on a background. The latter may also have originated from residual light sources in the room and from stray light of the QTH light source, or from Fresnel reflection and Fabry-Perot (Airy) fringes associated to the layered structure of the sample. The background is more dominant for smaller angles of incidence. The sharp features shift in wavelength with the variation of the incidence angle by more than 200 nm. Comparing the two graphs in figure 4.2a and 4.2b, it is found that the spectra recorded for TE polarization clearly differ from those recorded for TM polarization.

We have compared the measured reflectivity spectra with theoretical ones as calculated using the rigorous coupled wave analysis described in chapter 2. The result for along Γ-M symmetry direction is shown in figures 4.3a and 4.3b, for TE and for TM polarized incident light, respectively.

(a)   (b)
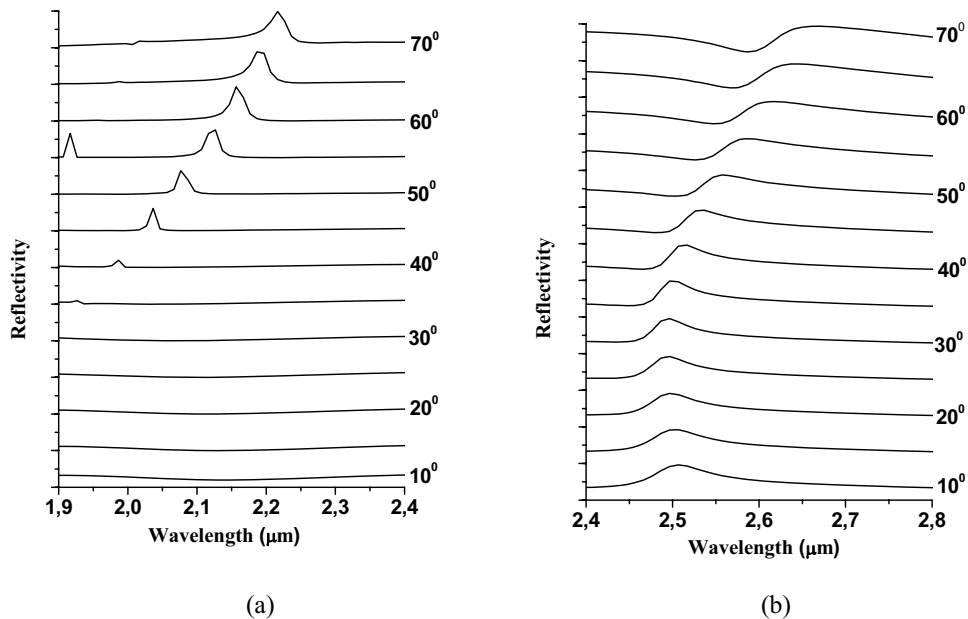
Figure 4.3 Calculated reflectivity of the photonic crystal slab as a function of wavelength for propagation along Γ-M symmetry direction, (*a*) for TE polarized and (*b*) for TM polarized light. The curves are vertically shifted for clarity.

Measurements were also performed along the Γ-X symmetry direction for both polarizations. These spectra are displayed in figures 4.4a (TE polarization) and for 4.4b (TM polarization), and show similar distinct features, which also shift in wavelength, as the angle of incidence is varied. Again, the theoretical spectra were calculated and are displayed in figures 4.4c and 4.4d, for TE and TM polarized light, respectively. For both polarizations and for both symmetry directions, a hole radius of 0.4 μm and a Si layer thickness of 0.5 μm were found to yield the best fit with the measured spectra.

(a)   (b)

(c)   (d)
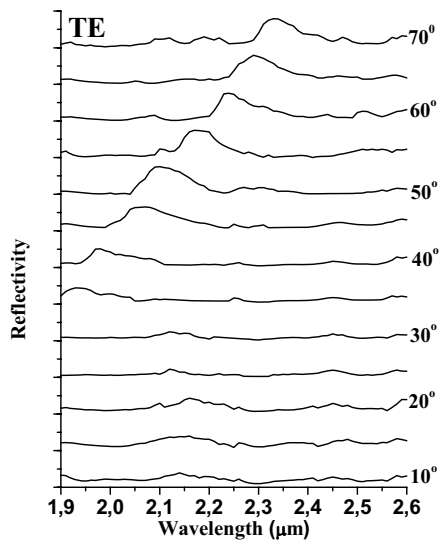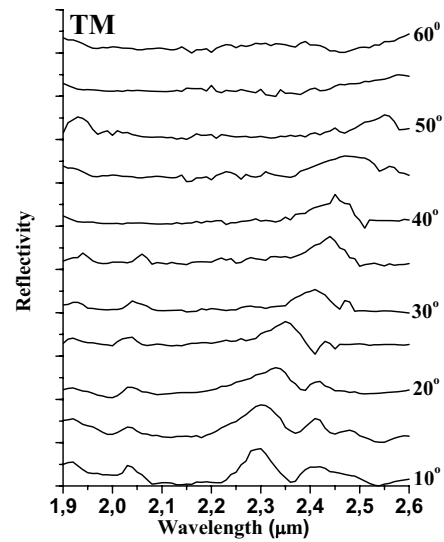
Figure 4.4 Reflectivity of the photonic crystal slab as a function of wavelength for propagation along $\varGamma$-X symmetry direction. Measured reflectivity (*a*) for TE polarized and (*b*) for TM polarized light. Calculated reflectivity, (*c*) for TE polarized and (*d*) for TM polarized light. The curves are vertically shifted for clarity; from bottom to top, the angle of incidence increases from $\theta = 10°$ to $70°$ (*a*) and from $10°$ to $60°$ (*b*).

It can be seen that calculated and measured reflectivities are comparable. Again, the spectra display distinct features, which also shift in wavelength, as the angle of incidence is varied. In figures 4.3c,d and 4.4c,d one can also see some slowly varying, background-like features (e.g. in figure 4.3a at $10°$, or in figure 4.4d at $40°$ around 2 μm). These are either due to broadband Fresnel reflection or broad Fabry Perot fringes from the layered structure of the sample, in addition to a background possibly from strong and background light.

4.2.2 **Line shapes of measured features**

A closer investigation reveals that the features possess different line shapes, such as maxima, minima, and dispersive (asymmetric) forms. Similar asymmetric line shapes have been observed for one-dimensional structures [5] and two-dimensional triangular [1] and square lattices [3]. In reference 1, these dispersive line shapes have been explained by the phase shift of the reflected light when it couples to a leaky mode. It is evident, however, that the observed differences in line shape hamper the extraction of the center wavelength and the linewidth of the probed leaky modes which are crucial to determine for the characterization of a PhC in a comparison with theory. Therefore, to accurately determine the center wavelength and linewidth, we have fitted the experimentally found resonances with the theoretically expected lineshape. The expected shape is a Fano-type of lineshape [6, 7] as was explained in chapter 2 (see equation 2.10) and was found to agree with experiments of others as well [2, 3].

Figure 4.5 displays three such Fano fits (solid line) to the experimental data (square symbols) obtained for the Γ-X symmetry direction, TM polarization, and for an angle of incidence of 10° (see also figure 4.4b, lowest trace).
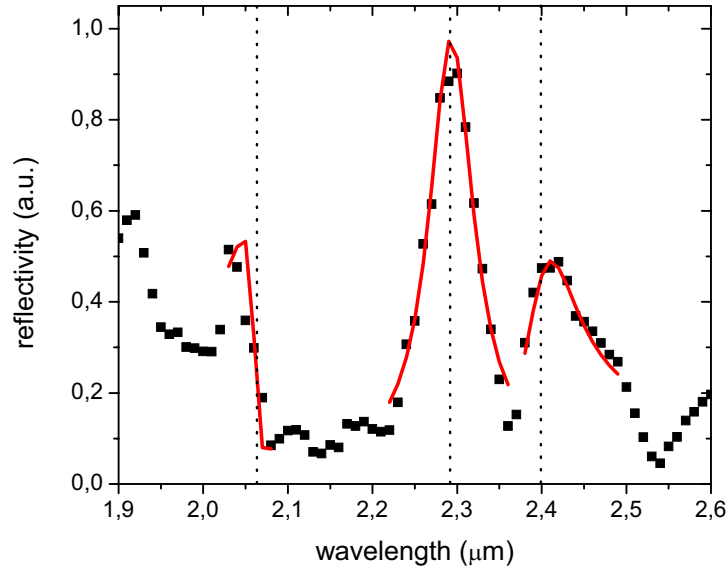
Figure 4.5 Example of a measured reflectivity spectrum with Fano-like line shapes. Squares: measured reflectivity for ΓX symmetry direction, TM polarization, and 10° angle of incidence as a function of wavelength. Solid lines: Fano-line shapes fitted to three distinct reflectivity features. Dotted vertical lines: center wavelengths of the Fano line shapes.

It can be seen that there is a good agreement of the fits with the experimental data. The fits yield, in this example, features with center wavelengths of 2.06 μm, 2.24 μm, and 2.29 μm (indicated by vertical dotted lines). This example demonstrates the suitability of the Fano function (equation 2.10) to describe the measured line shapes in the reflectivity spectra. In the following, we present the results obtained by fitting the described formula to our experimental specular reflectivity spectra, i.e., the bandwidth and the centre frequency of the features observed in the spectra.

4.3 Quality factor

The quality factor, Q, of a photonic resonance is a measure for the lifetime of a PhC mode, as was described in chapter 2. The lifetime of the investigated leaky modes is, on one hand, intrinsically limited by radiation losses. On the other hand, fabrication imperfections such as irregularities regarding the hole size, hole roundness and hole displacement (i.e. an erratious periodicity) can further lower the lifetime and, thus, broaden the width of the Fano resonances. The measurement of Q and a comparison to the intrinsic Q would, thus, give a quantitative indication of the fabrication quality of the LIL technique applied here.

The quality factor is calculated for each of the reflectivity features that could be identified in the measurements presented in figures 4.2 and 4.4a,b. Most of the Q values obtained lie in an interval between about 20 and 70. Only for the Γ-X symmetry direction and TM polarized light, some exceptionally high values are obtained, which are not considered for the evaluation in order to avoid statistical deviation. As such, the resulting mean Q value is more likely to be under-estimated than over-estimated. The Q values obtained for Γ-X symmetry direction yield a mean value of 46 ± 4 for TM polarized light and of 43 ± 3 for TE polarized light. For the second symmetry direction, Γ-M, the mean Q values are 45 ± 4, and 45 ± 5 for TM and TE polarized light, respectively.

The four mean Q values for the two different symmetry directions and the two light polarizations overlap, such that we can estimate the quality factor of the leaky modes of the 2D PhC to be around 45. This Q factor is about two orders of magnitude lower than that typically obtained from comparable, defect-free PhC slabs manufactured using other methods, like e.g., electron-beam lithography [8]. The effect is probably intrinsic to the LIL manufacturing process that seems to produce short-range errors in the hole shape (as can also be seen by the slightly irregularly shaped holes in the SEM image). The long-range periodicity, on the other hand, enters the data as well, due to the large probe beam diameter. thus the observed Q-values also form an upper limit for long-range periodicity errors, which should be low compared to other manufacturing methods, because, in contrast to those, LIL does not require displacement of the sample and is, thus, free of stitching errors.

67

4.4 Out-of-plane band structure - coupling to leaky modes

From the identified positions of the resonance features, the dispersion of the leaky modes probed by the reflectivity measurements are mapped by inserting the experimental data in the frequency-wavevector-plane. The resulting out-of-plane band structure for Γ-X symmetry direction is shown in figure 4.6a for TE polarized light and in figure 4.6b for TM polarized light.
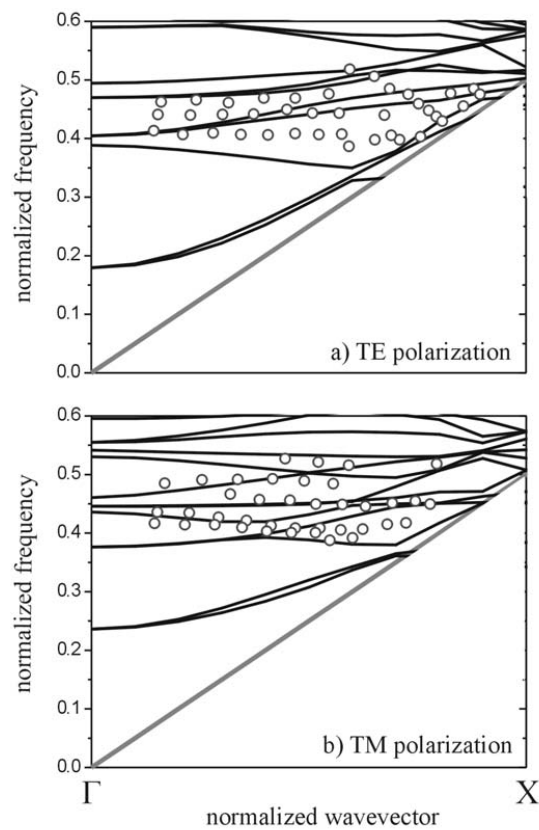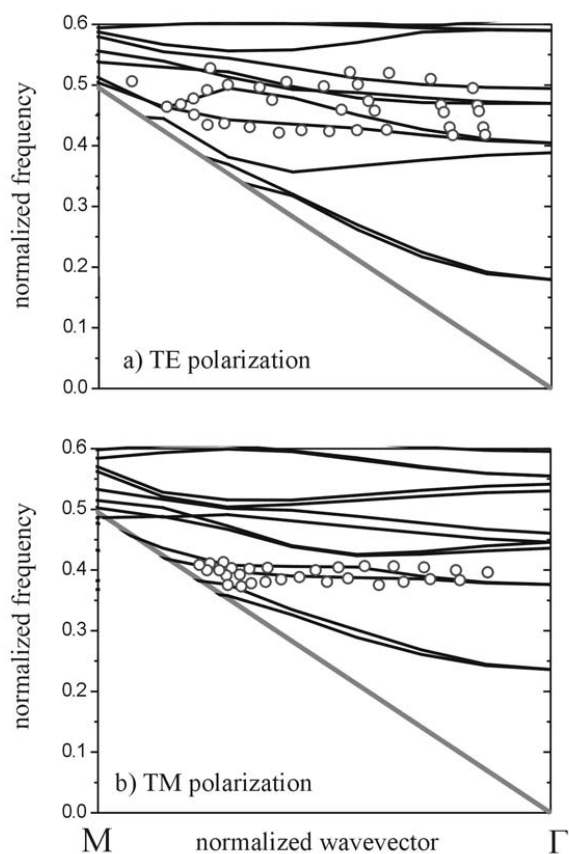

Figure 4.6 Out-of-plane band structure for Γ-X symmetry direction, (a), for TE polarized light and (b), for TM polarized light. The graphs show the dispersion obtained from the reflectivity experiments (open circles) together with calculated dispersion curves of the leaky modes (solid lines) above the light line, i.e., the dispersion of light in air (gray line).

In both graphs, the normalized frequency, i.e., the lattice constant of the photonic structure over the wavelength of the incident light is plotted as a function of the normalized wavevector. From left to right, the wavevector increases from 0 to the inverse periodicity in Γ-X direction. The gray line in both graphs represents the light line, i.e. the dispersion of light in air, which indicates the lower limit of the out-of-plane band structure in these graphs. The values obtained from the out-of-plane reflectivity experiments are displayed by circles. According to the wavelength range chosen for the experiment, the normalized frequency of the probed modes lies around 0.4. The dispersion has also been calculated [9] using the structure parameters obtained from SEM observations, depicted in figure 3.5 from chapter 3 (a periodicity of 1 µm and a hole diameter of 0.7 µm). In the calculations, the modes are usually referred to as being even or odd with respect to a horizontal symmetry plane. It is known that even modes only couple to TM polarized incident light, while odd modes couple to TE polarized light [10]. In figures 4.6a and 4.6b the calculated odd and even modes are displayed, respectively, by solid black lines. In both graphs, the experimental points agree with the calculated photonic bands, with one exception for the case of TE polarization (figure 4.6a), where the position of the experimental values appear to be at slightly lower frequencies and shorter wavevectors than expected from the calculated dispersion bands.

Figure 4.7 shows the corresponding out-of-plane band structure obtained for the Γ-M symmetry direction, for TE polarized (figure 4.7a) and for TM polarized (figure 4.7b) light. Again, the normalized frequency is plotted as a function of the normalized wavevector. In this case, the wavevector increases from left to right until the inverse periodicity in Γ-M direction is reached. As before, the experimental points are displayed as circles, and the corresponding calculated dispersion is given by the solid lines.

Figure 4.7: Out-of-plane band structure for *Γ-M* symmetry direction, (a), for TE polarized light and (b), for TM polarized light. The graphs show the dispersion obtained from the reflectivity experiments (open circles) together with calculated dispersion curves of the leaky modes (solid lines) above the light line, i.e. the dispersion of light in air (gray line).

In both graphs, better agreement than in figure 4.6 between measured and calculated dispersion can be observed.

4. 5 Summary and conclusion

In summary, we have presented the first, linear characterization in reflection of a large square-lattice photonic crystal slab based on Si. Angle dependent reflectivity measurements allows coupling to resonant modes situated above the light line. From the spectral position of the measured resonances, the dispersion curves of photonic modes are obtained in the range from 1.9 to 2.8 μm along the Γ-X and Γ-M crystal symmetry direction. The reconstructed dispersion curves from reflectivity measurements are in agreement with the band diagram simulations above the light line. Furthermore, the line shape of the measured resonances showed good agreement with that of Fano-type resonances. The line shape analysis based on Fano-fits reveals the resonance frequency, the line width of the resonance. We associate the line width to a quality factor of the resonant mode and, for the first time, determine the quality factors of the leaky modes observed for a PhC manufactured with the modified LIL method used for crystal fabrication. From our results, we conclude that LIL, in comparison with other commonly used processes, enables the manufacturing of large structures of only moderate short-range quality, but of excellent long (mm-) range periodicity. The presented experimentally obtained values for the quality factors of the probed resonant modes, about 45, can be of importance, e.g., for a realistic judgment of resonant field enhancement in optically nonlinear effects.

References

[1] V.N. Astratov, I.S. Culshaw, R.M. Stevenson, D.M. Whittaker, M.S. Skolnick, T.F. Krauss and R.M. De La Rue, J. Lightwave Techn. **17,** 2050 (1999)

[2] M. Galli, D. Bajoni, M. Belotti, F. Paleari, M. Patrini, G. Guizzetti, D. Gerace, M. Agio, L.C. Andreani, D. Peyrade and Y. Chen, IEEE J-SAC **23,** 1402 (2005)

[3] V. Pacradouni, W.J. Mandeville, A.R. Cowan, P. Paddon, J.F. Young and S.R. Johnson, Phys. Rev. B **62,** 4204 (2000)

[4] T. Berger and E. Brookner, Applied Optics **6**(7), 4204 (2001)

[5] M. Patrini, M. Galli, F. Marabelli, F. Agio, L.C. Andreani, D. Peyrade and Y. Chen, IEEE JQE **38,** 885 (2002)

[6] U. Fano, Phys. Rev. **124,** 1866 (1961)

[7] F.H. Mies, Phys. Rev. **175,** 164 (1968)

[8] T. Krauss, Y.P. Song, S. Thoms, C.D.W. Wilkinson and R. De La Rue, Electron. Lett. **30,** 1444 (1994)

[9] S.G. Johnson and J.D. Joannopoulos, Opt. Express **8**, 173 (2001)

[10] L.C. Andreani and M. Agio, IEEE J. Quantum Electron. **38**, 891 (2002)

Mid-infrared characterization of two-dimensional photonic crystal slabs fabricated in silicon with laser interference lithography

Chapter 5 Mid-Infrared transmission spectra of a large-area 2D silicon PhC slab

In the following sections the investigation of the transmission spectra, at normal incidence, of large area (1 cm^2) two-dimensional silicon photonic crystal slab is presented. The transmission spectra were measured from 1.1 μm (the near-infrared single-photon absorption edge of silicon) to 2.4 μm (the mid-IR two-photon absorption edge). The recorded spectra display Fano and Fabry-Perot type transmission resonances. The Fano resonances arise upon coupling between external radiation and resonances of the PhC sample. The Fabry-Perot resonances are attributed to interference between reflections from the three layers that make up the sample (top silicon layer, buffer silicon oxide layer and bottom silicon layer). The experimental transmission results are in agreement with transmission calculations spectra, based on plane wave simulations. Furthermore, for the first time, the influence of errors in large area high index contrast photonic crystal fabricated with LIL has been quantified in transmission. This was achieved by using a fitting function for the experimental data, which provides the quality factors of the investigated resonances. These are compared with theoretical quality factors expected for ideal crystals.

5.1 Experimental setup

The transmission measurements were performed with a spectrophotometer (Varian, Cary 5E) at near to mid-infrared wavelengths between 1.1 μm to 2.4 μm under normal incidence. The spectral bandwidth of the source was set to 4 nm (at a wavelength of 2 μm so that a resolution of about 3 THz is obtained). The far-field beam divergence of the light beam in front of the sample

was 4° x 3.4°. The rectangular cross section of the light beam was rather large, 2.5 mm x 1.5 mm, in order to allow for high throughput, however, the beam remained located entirely within the crystal's 1 cm^2 area. For showing the difference to a standard photonic crystal of microscopic size, as is typically available from scanning-type of fabrication methods (e.g. electron beam lithography), consider a 50 μm x 50 μm. In this case the large area of the incoming light beam would need to be reduced by a factor of 400 in order to match it to the crystal area. Taking into consideration the associated reduction in probe beam power, the standard square root law for shot noise this would have increased the measurement time by roughly a factor of 20 to achieve a similar signal-to-noise ratio as is achieved here. The experimental setup is similar to that employed in chapter 4, however, the detector is placed so that it is in the path of the transmitted radiation. The structure of the investigated 2D silicon PhC slabs is depicted schematically in figure 5.1, together with the corresponding first Brillouin zone and its Γ-X and Γ-M symmetry directions.
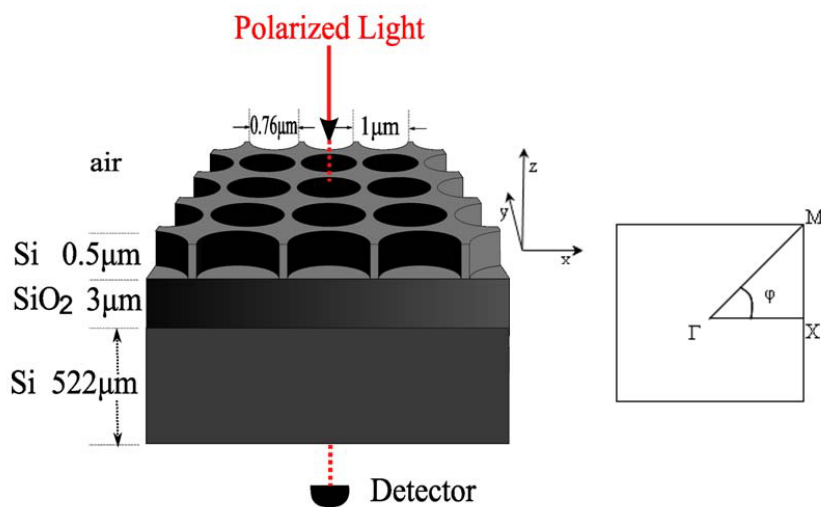
Figure 5.1 Schematic representation of the photonic crystal slab used to measure the transmission under normal incidence (left). The corresponding irreducible Brillouin zone is spanned by the Γ-X and Γ-M crystal symmetry directions (right).

A polarizer is placed in front of the crystal to set the polarization. To orient the photonic

crystal's hole pattern at a known angle with regard to the polarization direction, the sample is rotated about its surface normaļ. The coarse orientation of the x and y-directions are displayed by the edges of the square-shaped crystal which is cut approximately parallel to these directions. A few degrees of rotation is then sufficient to orient the diffraction (Laue) pattern obtained with a HeNe laser under normal incidence symmetrically with regard to the direction of the polarizer. Behind the sample the transmitted light is collected by a large-area detector. Absolute transmission spectra were obtained by normalizing experimental data to the spectrum of the incident light with no crystal in the sample mount. The spectra show a signal-to-noise ratio of about 100 with a recording time of a few minutes per spectrum.

5.2 Results and discussion of the transmission spectra

For normal light incidence onto a PhC slab with round holes and 4-fold rotation symmetry, theory predicts the transmission to be polarization independent [1]. In order to verify this we have measured transmission spectra for light polarized along the Γ-X axes (0°), the Γ-M (45°), and in between ($\varphi = 22.5°$). As can be seen from figure 5.2, the spectra are almost identical, with less than 5 percent deviations in transmission, which confirms the expected polarization independence.
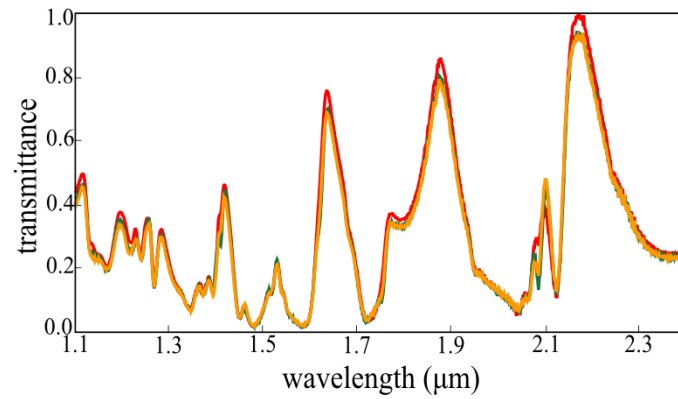
Figure 5.2 Transmission spectra of the PhC slab measured at normal incidence. The electric field polarized along the *Γ-X* direction (φ = 0°, red trace), the *Γ-M* (φ = 45°, orange) and along an intermediate direction (φ = 22.5°, green).

Based on this observation, in the following, we restrict ourselves to the analysis of one of the measured transmission spectra, for which we select the trace with φ = 45° (electric field along *Γ-M* direction) as replotted in the upper part of figure 5.3a.

In the following, we restrict ourselves to one of the measured transmission spectra, for which we select the trace with φ = 45° (polarization parallel to the *Γ*-M direction) as replotted in the upper part of figure 5.3a.
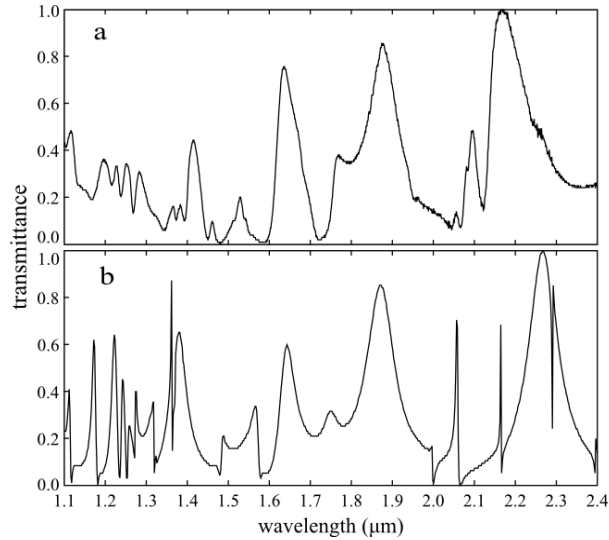
Figure 5.3 Measured (a) and calculated (b) transmission spectra at normal incidence for linearly polarized light.

It can be seen that the spectrum consists of a series of broader transmission peaks (e.g., 100 nm bandwidth at around 2.15 μm), which resemble an Airy-type transmission function, on which narrower, Fano-type dispersive features are superimposed (e.g., around 2.1 μm).

The origin of the broader resonances can be attributed to interference in the alternating layers of materials and their respective refractive indices. For instance, the slow variation of transmission along the broad resonances indicates a low quality factor and a wide free spectral range (FSR), which may be addressed to the small thickness of the top and buffer layers and to the well-below-unity Fresnel reflectivity of the involved interfaces.

For a better identification, we calculate the FSR that corresponds to the effective thickness and index of the three layers. The top layer consists of about 62 % Si and 38 % air, as can be concluded from the air filling factor, which is determined by the diameter and spacing of the holes. Based on the effective medium theory [2] this corresponds to an effective refractive index of 2.48. The 0.5-μm thickness of this layer then corresponds to a relatively large FSR of 121 THz. For the 3-μm thin silicon oxide buffer layer ($n = 1.5$), we predict an FSR of 33 THz. The 522-μm thick Si thick substrate corresponds to a small FSR of 80 GHz.

The recorded spectra show a spacing between the three main Airy peaks (at 2.15 μm, 1.85 μm and 1.63 μm) of 22.6 and 21.9 THz, respectively. These values indicate that the Airy resonances are to be addressed to the buffer layer and suggest a thickness of 4.5 μm for this layer. On the other hand, when looking at the spacing between Airy-peaks at shorter wavelengths (e.g., at 1.85 vs. 1.525 μm, or 1.63 vs. 1.42 μm), we find values of 34.6 and 27.2 THz, respectively. This indicates thicknesses of 2.9 μm and 3.7 μm, in better agreement with the wafer specifications (3 μm). The overall variation of the peaks observed across the entire, 150 THz wide recorded spectrum may be addressed to the thin Si top layer, whereas the calculated FSR of the substrate falls well below the resolution of the spectrometer.

Next, we will focus on the origin and properties of the narrow-band features observed in transmission, such as in the range between 2 and 2.2 μm. These sharper, dispersive features, superimposed on the Airy resonances, can be attributed to the photonic structure in the Si top layer [3]. At normal incidence illumination, the hole pattern diffracts part of the incident light into the plane of the crystal where, at suitable frequencies, leaky modes of the PhC slab can be excited and diffractively radiate back into the normal direction. This corresponds to an additional transmission path at leaky mode frequencies. The superposition of this path with direct (zero in-plane wave vector) transmission then leads to dispersive and asymmetric Fano-shaped resonances that can, e.g., be located in the wing of a broader Airy resonance.

To model the transmission, we numerically calculated the transmission function using the rigorous coupled wave analysis (RCWA) [4].

The transmission was calculated for normal incidence, with the electric field aligned along the Γ-M direction and with the following parameters as given above, i.e., a hole diameter of 0.76 μm, a periodicity of 1.0 μm, an effective index of 2.48 for the top layer, and a 3 μm thick buffer layer. The thickness of the silicon top layer, the index of the buffer layer, and the index of the substrate were slightly varied in order to obtain a best fit of the calculated spectrum. A problem is that the very high spectral resolution, as would be required here to well resolve the rather small (0.08 THz) FSR of the thick substrate, would lead to prohibitively long calculation time and memory requirements. On the other hand, for a comparison to our experimental spectra, such high resolution is not required because the experimental resolution (3 THz) averages such fringes out, thereby yielding a constant background from the substrate's Fresnel reflection. Based on these

considerations we accounted for the finite experimental resolution with a sufficiently low substrate thickness, and at below 0.01 μm we found only neglegible influence on both the Airy-type and Fano-type resonances.

When comparing the calculated transmission spectrum with the experimental one (figure 5.3), a fair agreement can be seen in the number, position and height of the broader (Airy) features when using for the calculations a top layer thickness of 0.55 μm, a buffer layer index of 1.44, and a substrate index of 3.45. From this we can conclude that the parameters used for the calculation are well suited to describe the overall optical properties of the PhC. One can find also fair agreement in the spectral positions where sharper Fano features are expected, however, the spectral width of the measured resonances is clearly larger than for the perfect (error-free) structure assumed in the calculations. This deviation in linewidth for the Fano resonances thus indicates the strength of errors inherent to our LIL fabrication process.

In order to quantify the influence of these fabrication errors, we determined the quality factor of the measured Fano-shaped resonances (defined as the center frequency divided by the linewidth) from the experimental spectra by local fits Fano functions to the data. In previous cases [3, 5-7], Fano functions were used which assumed a spectrally constant background transmission interfering with the Lorentzian-shaped resonances of leaky modes. Here, however, the observed Fano resonances are clearly located in the wing of broader Airy resonances, i.e., the background transmission cannot be assumed as constant but varies slowly with frequency, thereby modifying the shape of the Fano resonances [8]. In order to account for this with a combined Fano-Airy fit function, we replaced the spectrally constant amplitude of background transmission (see equation 3 in [3]) with the Airy field transmission function [9] (see chapter 2) for the layer parameters found from the RCWA-fit in figure 5.3b. The center frequency, width and amplitude of the Lorentzian component were used as fit parameters. Figure 5.4 shows an example of such an Fano-Airy fit and it can be seen that there is a good agreement with the experimental line shape.
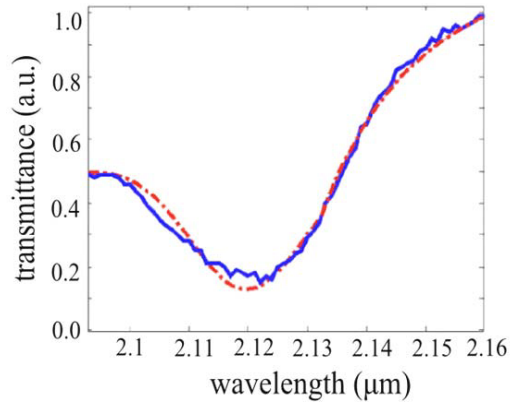
Figure 5.4 Example of a measured transmission spectrum (solid blue line) compared with a combination of Lorentz and an Airy function (dash-dot line).

For this resonance, the fit yields a *Q*-value of 125 and a center wavelength of 2.12 μm. Similar fits at two further resonances (at 2.05 and 2.08 μm) gave *Q*-values of 130 and 90 respectively. These *Q*-values are high compared to those derived from reflectivity measurements. The discrepancy may arise because the reflectivity data were obtained only at non-zero angles of incidence, with up to 70°. Also at the smallest angle (10°) the TE and TM spectra had shown a clear difference and, at this angle, the relative spread of the in-plane wave vector is relatively large (30°). This might have reduced the observed *Q*-value. The lack of polarization dependence (see figure 5.2) at normal incidence suggests that no noticeable decrease of the observed *Q*-values is expected at almost the same beam divergence. Finally, the Fano function fitted to the reflectivity data assumed a constant background. A finite background slope due to Airy resonances, may partly be interpreted as an increased width of the Lorentzian contribution, i.e., as a lowered *Q*-value.

For a comparison with theoretical expected *Q*-values, we used a finite-difference time-domain (FDTD) method [10] as described in chapter 2. These calculations reveal the Q-values as given solely by intrinsic losses in an ideal structure, i.e., the maximum achievable values are limited only by diffraction at the pattern of holes [11]. For the computations we used again the same parameters as in chapter 4, however, with the substrate extending to beyond the computational

cell, thereby assuming an infinite thickness. The motivation and justification of this approach follows similar arguments as for a thin substrate in the RCWA calculations.

From the calculations we find intrinsic Q-values, ranging from 161 to 358 for the resonances in the wavelength range from 2 μm to 2.2 μm. The difference between the experimental Q-factors and theoretical predicted values are due to extrinsic losses, which are associated with experimental deviation from an ideal structure. The contribution of extrinsic losses can be estimated to be around 200 from the measured Q and the calculated Q.

Extrinsic losses can be caused by irregularities or sidewall roughness [12], tapered sidewalls [13], or out of plane scattering [14, 15]. However, recent experiments performed on large structures for the THz range have shown that the most dominant contribution comes from errors in the large-scale periodicity of the hole pattern [16]. These experiments were restricted to the relatively small area crystal structure of about 20 x 20 periods where, however, the relative fabrication precision of THz PhC slabs is excellent. In contrast, our experiments test a much wider range of large-scale periodicity (up to 10,000 x 10,000 periods) and still yields Q-values that are, within a factor of 1.2 to 2.5, comparable to the theoretical values. This indicates that the modified LIL fabrication technique provides excellent long-range periodicity over a large area.

5.4 Summary and conclusion

We have measured the spectral transmission of a large-area (10 mm x 10 mm) two-dimensional Silicon photonic crystal slab waveguide in the near- and mid-infrared wavelength range. Transmission was recorded under normal incidence over the wavelength range from 1.1 μm to 2.4 μm. We observe Fano and Fabry-Perot-type transmission resonances, which are independent of polarization. The position and height of the resonances are in reasonable agreement with predictions based on rigorous coupled wave analysis. The width of the measured Fano resonances, which originate from the photonic hole structure, show Q-values between 90 and 130. These values are a factor of 1.2 to 2.5 above what is predicted for a perfect structure. However, as the Q-values of such resonances are predominantly susceptible to errors in the long-range periodicity, the present experiments mainly form a test of the long-range periodicity of the

fabrication technique.

References:

[1] V. Lousse, W. Suh, O. Kilic, and S. Fan, *Opt. Express* **12**, 1575 (2004)

[2] T.C. Choy, *Effective Medium Theory, Principles and Applications*, Oxford University Press, 1999

[3] S. Fan and J.D. Jonnopoulos, *Phys. Rev. B* **65**, 235112 (2002)

[4] DiffractMod software under RSoft program

[5] L. Prodan, P. Gross, R. Beigang, L. Kuipers, and K.-J. Boller, *J. Phys. D: Appl. Phys*. **40**, 5571 (2007)

[6] U. Fano, *Phys. Rev.* **124**, 1866 (1961)

[7] V. Pacradouni, W.J. Mandeville, A.R. Cowan, P. Paddon, J.F. Young and S.R. Johnson, *Phys. Rev. B* **62**, 4204 (2000)

[8] F.H. Mies, Phys. Rev. **175** 164 (1968)

[9] E. Hecht, *Optics Light for a New Age* (Addison-Wesley Publisher) 2001

[10] MIT Electromagnetic Equation Propagation (MEEP): http://abinitio.mit.edu/wiki/index.php/Meep

[11] W. Bogaerts, P. Bienstman, D. Taillert, R. Baets, and D. De Zutter, *Opt. Quant. Electron.* **34***, 195 (2002)

[12] W. Bogaerts, P. Bienstman, R. Baets, *Opt. Lett.* **28**, (2003)

[13] Y. Tanaka, T. Asano, Y. Akahane, B.S. Song and S. Noda, *Appl. Phys. Lett.* **82**, 1661 (2003)

[14] R. Ferrini, R. Houdre, H. Benisty, M. Qiu and J. Moosburger, *J. Opt. Soc. Am. B* **20**, 469 (2003)

[15] H. Benisty, D. Labilloy, C. Weisbuch, C.J.M. Smith, T.F. Krauss, D. Cassagne, A. Beraud and C. Jouanin, *Appl. Phys. Lett.* **76**, 532 (2000)

[16] T. Prasad, V.L. Colvin, and D.M. Mittleman, *Opt. Express* **15**, 16954 (2007)

Mid-infrared characterization of two-dimensional photonic crystal slabs fabricated in silicon with laser interference lithography

Chapter 6 Nonlinear optical phase switching of a 2D PhC slab

6.1 General introduction of nonlinear optical response from PhC

So far we reported on the characterization of the linear optical properties of a Si PhC slab fabricated by a modified LIL method, i.e., where a single, low intensity probe beam in the near to mid-IR range was incident to the sample. In this chapter we present initial results on the nonlinear optical response from the same sample. In particular, we demonstrate that light induced changes in reflectivity, enhanced by a guided resonance, can even be observed at rather moderate pulse energy (*nJ* range), such as available from standard *fs* laser oscillators. The key to observability is to measure light induced change in the optical phase upon reflection from the PhC, rather than changes in reflected power. For phase changes in ultrashort time intervals, we employ mid-IR ultrashort probe pulses and a Mach-Zehnder interferometer. Phase changes in reflection from the PhC are induced with additional near infrared, ultrashort pulses. With this technique we observe an optical switching of the reflection phase from a guided resonance.

In the last decade, many studies have focused on observing nonlinear optical effects in PhC's, with the goal to influence light with light, which is of interest, e.g., for potential future applications in optical information processing. Particular interest lies in the potential to arrive at processing with much higher speed than possible with electronics. The solution to such high speed is to employ optical nonlinearities with an ultrafast response and recovery time, i.e., where the refractive index is rapidly varied by an ultrashort pulse from a sufficiently intense drive laser. The induced index variation can then modify a photonic resonance in order to control the propagation of another light signal.

Usually, because the nonlinearity of most materials is rather small, the described effects not only

require high light intensities but also large interaction lengths. The purpose of a PhC is to provide a large, effective interaction length or, in other words, a photonic resonance enhances the nonlinear response. More specifically the goal is to enhance nonlinear effects on a wavelength (micron) scale with a sufficiently strong optical confinement, to be provided by photonic structures with a high-index-contrast. For providing the required high intensities, ultrashort pulses from a standard modelocked laser oscillator (typically *nJ*-range pulse energies) can be amplified by several orders of magnitude in multipass or regenerative amplifiers. A disadvantage of this is, however, that this lowers the pulse repetition rate into the *KHz* range and may lengthen the pulse duration.

When looking at the speed and strength of the various types of nonlinearities available, unfortunately, one finds that increasing the speed leads to a correspondingly lower strength. For example, the fastest optically induced changes of the refractive index (within a few *fs*) can be obtained via the optical *Kerr* effect, which is a third-order, non-resonant effect. This effect occurs in any transparent material and changes the material's refractive index, n_0, in proportion with intensity according to $n(I) = n_0 + n_{NL}I$, where I is the intensity, and where the coefficient n_{NL} is called the *Kerr* index or nonlinear index. The typical values for n_{NL} are indeed small, e.g., in the order of $n_{NL} = 10^{-20}$ m^2/Watt for glass, meaning that the initial index, n_0, can only be changed by a small fraction of a percent even with intensities near the damage threshold (GW/cm^2). A resonant enhancement of the intensity by the resonances of a photonic is then of particular interest to lower the externally required (incident) intensity. Due to the high attractivity of the nearly instantaneous response, the *Kerr* effect has since long been considered for an implementation in photonic crystals, e.g., to induce a light induced spectral shift of photonic band gaps [1, 2]. Similar predictions are a *Kerr*-induced frequency shift and modified shapes of photonic resonances [3]. The first experimental signs of *Kerr*-based switching were reported with a periodic stack of Si - SiO$_2$ layers on a glass substrate, which essentially forms a one-dimensional PhC [4]. Beyond this, there has been relatively little experimental success to demonstrate *Kerr* switching in PhC's with higher dimension, i.e., 2D and 3D PhCs. For instance, Rahn et al. have found signs of self-phase modulation (SPM) with ultrashort pulses in a 2D photonic crystal waveguide made from AlGaAs [5]. SPM is a non-resonant, third-order nonlinear effect but here it occurred only in combination with resonant effects, single and two-

photon absorption. In a more recent experiment, the excitation of the leaky modes of a GaAs PhC slab showed signs of *Kerr* response [6]. Nevertheless, the two-photon absorption and a corresponding carrier excitation dominated these results as well although, in part of the experiments, the drive laser was tuned to slightly below the half-gap frequency to avoid two-photon absorption.

A different and much more successful method to obtain an optically induced index change is the generation of free carriers by linear absorption of the drive laser [7, 8]. As linear absorption is a resonant and first-order process, much lower light intensities are sufficient to modify the refractive index. The change of index with carrier excitation, and its use for optical switching in photonic crystals has been theoretically investigated in a number of publications (see, e.g., [9] and the references therein). However, a general property of carrier induced switching is a much longer relaxation time of the nonlinear index change which is caused by the finite recombination time of the excited carriers (typically in the range of a few to more than 100 picoseconds), which reduces the potential switching speed accordingly. A shortening of the response down to a few *ps* has been reported due to the faster recombination of carriers at the surface of photonic structures [7]. A variation of the response time can also be achieved by changing the electronic material properties, such as via introduction of quantum wells [10]. Leonard et al. were the first to show an ultrafast photonic band-edge tuning in a 2D PhC in the near infrared via such injection of free carriers [11]. Roberts et al. have recently observed up to 30 % change in reflectivity from a 2D PhC by a carrier induced shift of a guided resonance [7].

Actually, the named carrier-excitation has so far accompanied all experiments on *Kerr* induced switching. The reason for this is that, even when the photon energy of the drive laser is below the electronic bandgap, two-photon absorption occurs due to the high intensities required for inducing a *Kerr* effect. Two-photon absorption would become reduced when the photon energy is well below the electronic half-gap. However, such experiments seem not to be performed yet. The reason is, possibly, that this requires photonic crystals for the mid-IR, and also highly intense and ultrashort light pulses in the mid-IR where substantial pulse energies (*mJ* - range) are less easily available.

A common feature of all the above named experimental observations of nonlinear effects in photonic crystals is that exclusively changes in the optical power (e.g. changes in reflected

power) have been observed. This mode of observation requires a substantial spectral shift of photonic resonances with drive intensities that often require larger oscillator-amplifier systems with *mJ* level pulse energies.

In this thesis we report the observation of nonlinear carrier induced response from a 2D PhC at much lower intensities as generated with pulse energies of only a few *nJ*. The key to this is to use interferometric detection of the nonlinear response. Specifically, we measure the *phase shift* of light reflected from a 2D PhC, rather than measuring *power changes* in the reflected beam. With the increased sensitivity in detecting phase changes interferometrically, the pulse energies required from the drive laser can be provided by most modelocked oscillators without amplification. To simultaneously provide an ultrafast temporal resolution in these phase measurements, we employ ultrashort probe pulses with an adjustable delay with respect to an ultrashort drive laser pulse. After reflection of the probe pulses from the PhC, optical phase changes are inspected with a Mach-Zehnder interferometer.

Our observations are performed with the LIL-fabricated Si PhC as described and characterized in the previous chapters 3 and 4. For exciting a guided resonance at probe wavelengths of around 2.1 μm wavelength we have use oblique reflection of ultrashort probe pulses in that wavelength range. To obtain a switching of the phase of the reflected probe light we used drive pulses with two alternative wavelengths (1.2 μm and 0.75 μm). A wavelength of 0.75 μm was chosen in order to provide a strong excitation of free charge carriers via single-photon absorption in Si. When the drive laser wavelength was set to 1.2 μm, carrier excitation is possible only via two-photon absorption which may also involve probe photons.

6.2 Experimental setup

To probe the phase of reflection provided by a guided resonance, a suitable probe wavelength is to be chosen at which a photonic resonance in the PhC can be excited. As the optimum range of operation of the available light source (see below) was at around 2.1 μm wavelength, we selected a guided resonance in this range. Such resonance is present at an angle of incidence of 45°, along the *ΓM* symmetry direction and for TE polarized light, as is described in chapter 4.

The light sources available in the experiments [12] were a mode-locked Ti:Sapphire laser which synchronously pumped an optical parametric oscillator (OPO). Thereby, temporally synchronized ultrashort pulses are available at three wavelengths simultaneously, i.e., the laser wavelength, the OPO signals wavelength, and the OPO idler wavelength. Figure 6.1 depicts the remainder of the optical setup, i.e., a delay line in the beam line for the drive pulses (lhs) and the Mach Zehnder interferometer (rhs). A HeNe laser is used for general assistance in alignment of the probe beam through the interferometer.
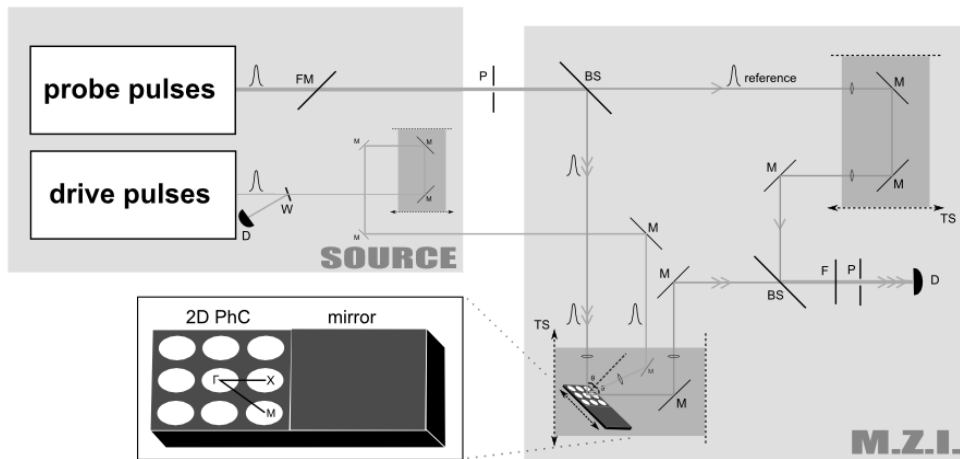
Figure 6.1 Schematic diagram of the experimental setup.

The mode-locked Ti:Sapphire (TiSa) oscillator (Tsunami, Spectra Physics, model 3960) generates 25 nJ pulses at a repetition rate of 80 MHz. The FWHM pulse is measured as 100 fs with an intensity autocorrelator (NT&C, Micro$cor Type A). The spectrum of the Tsunami is measured with an optical spectrum analyzer (IST-REES E201). The center wavelength of the laser can be tuned between 720 and 850 nm. In our experiments the center wavelength was set to a value of 750 nm. The average power at this wavelength was measured as 2 W. A fraction of about 500 mW is sent through an adjustable delay line (using a Thorlabs, PT series translation stage) towards the PhC, for use as drive pulses.

The remaining power (1.5 Watt) from the laser is used to synchronously pump an optical

parametric oscillator (OPO, Spectra Physics OPAL). Via changing the temperature of the nonlinear crystal in the OPO (LBO) the signal wavelength can be tuned in the wavelength range from 1.1 μm to 1.3 μm, and the idler wavelength from 1.9 μm to 2.3 μm. The average idler power is 50 mW and the signal power is 150 mW. The pulse duration of the idler pulses is 150 fs as measured with an autocorrelator (APE Berlin, Micro). The center wavelength of the OPO signal wave is measured with a laser spectrum analyzer (IST-REES E202). From the pump and signal wavelengths one can then infer the idler wavelength. The signal beam from the OPO can be adjustably delayed and sent along the same path as the beam from the TiSa laser. Thereby the signal pulses can be employed as alternative drive pulses for the PhC as well.

The idler beam is sent to the MZI setup (figure 6.1, rhs). At the interferometer entrance, the beam is split into two beams of approximately equal power with a pellicle beam splitter. The first beam is sent towards the PhC sample and is called the sample beam. A CaF_2 lens is used to focus the probe beam to a beam diameter of about 20 μm. The probe beam is incident to the PhC under an angle of 45° along the ΓM symmetry direction with TE polarization and the reflected probe pulse is sent with a gold mirror towards the interferometer output. The other beam from the beam splitter, called the reference beam, is sent via gold mirrors along a computer-controlled delay line, which determines the optical path length difference between the reference and sample beam. The delay line is based on a high precision piezo-driven motor (New Focus, picomotor, 20 nm resolution). At the interferometer output the reference and sample beams are recombined with a second pellicle beam splitter. Behind absorptive filters that block any residual radiation from either of the drive beams, and behind an adjustable aperture, the probe radiation is detected with a mid-IR InGaAs photodiode (DET 10D, Thorlabs, sensitive between 1.2 μm - 2.6 μm, active area 0.8 mm^2). To record the average probe beam power, a multi-stage amplifier and a DC current detection circuit follow the photodiode. The response time of the probe beam detection is about 1 ms.

Also the beams with either 0.75 μm wavelength from the TiSa laser or 1.16 μm from the OPO signal are directed onto the PhC and focused to a diameter of about 25 μm. These beams provide drive intensities of roughly 1 GW/cm^2 and 100 MW/cm^2, respectively, and both values are well below the damage threshold of Si (a few hundred GW/cm^2). The drive beams are incident under an angle of about 20° in the same plane as the probe beam and are TE polarized as well. The

spatial overlap of the probe and each of the drive beams is carefully checked with a 25 μm pinhole and observation of transmitted light on a photodiode. The temporal overlap of the probe and drive pulses is adjusted with two-photon absorption in a photodiode. The temporal overlap of probe pulses from the sample and reference arms becomes apparent when the InGaAs diode records interference fringes within a certain length of arm length difference in the MZI.

6.3 Recording and evaluation of interferograms

For recording interferograms of the 150 fs long and wavelength tunable probe pulses (from 1.9 μm to 2.2 μm) the electrical signal from the InGaAs diode is recorded as a function of the optical path length difference between the sample and reference arms of the MZI. The smallest step size in delay, δL, is 40 nm per step as limited by the smallest step size of the picomotor acting on the delay line in the reference arm (20 nm/step). Using the relation $\delta t = c/\delta L$, this correspond to a temporal resolution in delay time, δt, of about 0.13 fs, or about 1/50 of an optical cycle of the probe carrier wave, or a phase resolution, $\delta \phi$, of 0.13 rad. However, independent mechanical vibrations in the interferometer arms may disimprove the resolution influence the arm length difference. To quantify this, a separate measurement of the experimental error in phase measurements is described below. The recording of an interferogram typically comprises 6250 delays in a minute. A typical example of a recorded interferogram, with the PhC replaced by a gold mirror (such that only gold mirrors are present in the MZI), is shown in figure 6.2.
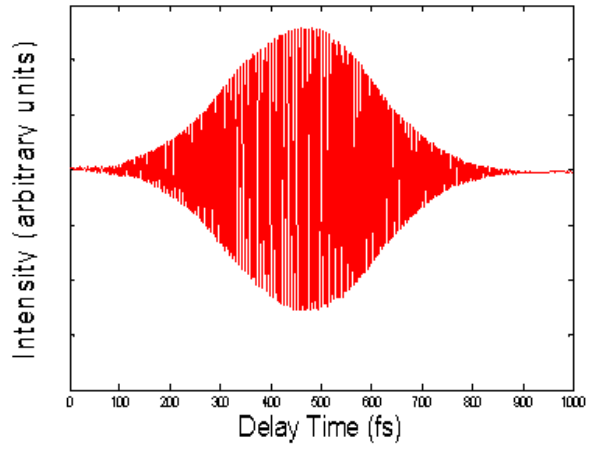
a)
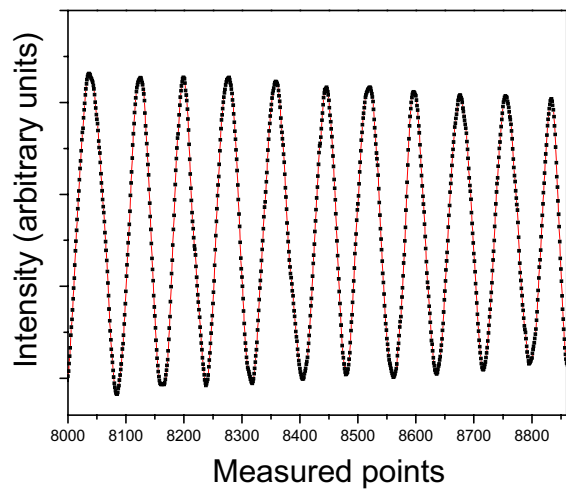
b)

Figure 6.2 a) Full interferogram measured as recorded with only gold mirrors in the MZI. b) Enlarged part of (a) showing well resolved interference fringes. The red line connects neighboring data points.

The interferogram consists of 6250 data points and displays approximately 50 interference fringes. In the upper part of the figure (a), where a complete interferogram is shown, the apparent randomness in fringe spacings and fringe amplitude is only caused by the limited resolution in plotting the large amount of data. This can be seen from the lower part of the figure (b), where an enlarged section of the same interferogram is shown. Here it can be seen that the fringes are highly periodic and that, about 50 data points are recorded per delay over one wavelength.

To retrieve small phase shifts that occur in the sample arm with regard to the reference arm, the data have been evaluated along the lines as described, e.g., in reference 13. As the variation of data around the average detector signal is the cross correlation function of the probe field in the two arms, the Fourier transform of the cross correlation yields the complex-valued amplitude spectrum of the delay difference between the two arms. More specifically, if one of the optical components is exchanged, e.g., here a gold mirror vs. the PhC, the change found after Fourier transformation yields the difference in the amplitude of the reflection spectra obtained by this exchange of components. Here, importantly, when the PhC in the sample beam is probed, e.g., without and with irradiation from the drive laser, the difference of the Fourier transform of the two interferograms reveals the change of the reflection amplitude spectra that was induced by the drive laser. Taking the arctan of the imaginary-to-real-part-ratio gives then the real-valued change of phase shift (as function of probe beam light frequency), which was induced by drive laser irradiation. Taking the square root of the sum of squared real and imaginary parts gives the real-valued change in the reflection amplitude (as function of probe beam light frequency).

For implementing such data evaluation we have used a phase extracting procedure, which is, similar to the one developed by Takeda et al [14]. Briefly, the steps of the data processing are as follow. First, fast Fourier transformation (*FFT*) is applied to the measured interferograms. Thereafter, spectral components that are likely not to come from the quasi-periodic fringe pattern in the interferogram are removed from the real-valued *FFT* phase and amplitude spectra, such as low frequencies from slow variations of background radiation and high frequencies from electronic noise. With an almost linearly increasing phase as function of the inverse delay, this typically yields a saw-tooth-like phase spectrum as is shown figure 6.3, in which the phase is defined only modulo 2π, which is called a discontinuous phase spectrum or wrapped phase

spectrum. Next, for a better overview of the overall phase variation vs. light frequency, the phase is unwrapped, i.e., the phase spectrum without the discontinuities in the phase spectrum is calculated. The unwrapping is mathematically defined as the integral of the derivative of the wrapped phase. Here, in the numerical data evaluation, the unwrapped phase is obtained by summing up the phase differences between preceding data points if the phase jumps are smaller than 2π, or by adding a phase reduced by 2π if a phase differences is larger than 2π [15].
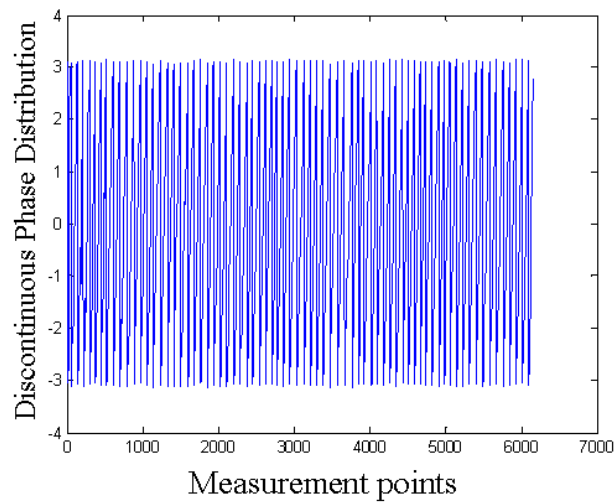
Figure 6.3 Wrapped phase spectrum obtained from the data in figure 3 after FFT.

Figure 6.4 shows the central part of the unwrapped phase spectrum obtained from the interferogram in figure 6.2 (black curve) and the corresponding amplitude spectrum (blue curve). The straightforward *FFT* spectrum, as shown in figure 6.4, yields only relatively few data points in the shown spectral interval. However, in a more elaborate data evaluation, a more dense coverage with data points may be obtained with so-called zero-filling techniques [16]. For example, the width of the recorded interferogram is increased (and thereby the number of data points per spectral interval after *FFT* is increased) by extending the interferograms with additional zeroes at both ends, where the measured interference contrast is neglegible.

When inspecting the amplitude spectrum in figure 6.4, we find that the width of central peak is

in good agreement with the spectral bandwidth of the probe radiation. From the phase spectrum can be seen that the phase increases smoothly and almost linearly by approximately 40 rad over the shown range. This can be addressed to the smooth dispersion of the additional gold mirror, which is present in the reference arm, and to the CaF_2 lens which is present in the sample arm. Note, however, that special care has to be taken with phase spectra due to the following reason. The numerical calculation provides a phase value for all frequencies in the *FFT* spectrum. Nevertheless, in the wing of the spectrum, where the spectral amplitude drops to around zero, the definition of the phase becomes meaningless and, correspondingly, there the displayed phase can be subject to large errors. To exclude such errors we have, in the following, maintained only a small sub-set of the phase data centered in the narrow spectral range where the measured spectral amplitude is above a fourth of its maximum value. To obtain phase spectra over a wider range than shown in figure 6.4 we have, instead, tuned the probe wavelength to a next, adjacent value and recorded a next interferogram.
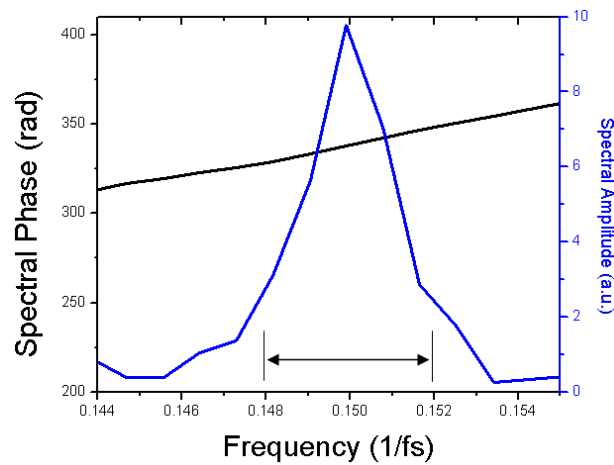
Figure 6.4 Amplitude spectrum and unwrapped phase spectrum obtained by *FFT* from the interferogram in figure 6.2. We regarded only phase data within the shown spectral interval of 0.004/fs width, where the spectral amplitude is well above zero.

Before measurements of light induced phase changes in the PhC can be presented, it is required

to experimentally determine the reproducibility and noise in measuring phase variations. To obtain a measure for such errors, we inspected two interferograms that were recorded with nominally the same parameters settings (e.g., the probe wavelength, alignment, or sample was not changed), but the second interferogram was recorded at a later time (4 minutes). The difference in phase spectra was computed and is shown in figure 6.5.
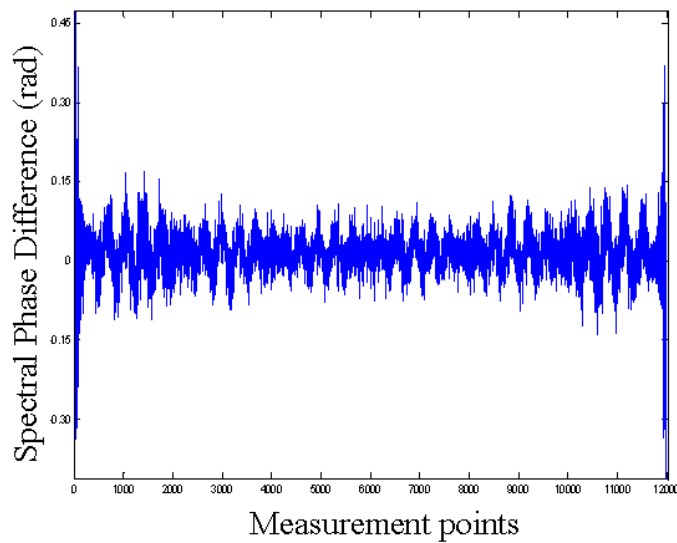
Figure 6.5 Evaluation of the experimental phase error: the shown trace is the difference between two independently recorded phase spectra using the same experimental settings. It can be seen that the peak-to-peak phase error amounts to approximately 0.25 rad while the full width rms is less than 0.1 rad.

As can be seen in the figure 6.5, the peak-to-peak (full width) phase noise over most of the spectrum is less than approximately $\lambda/25$ (0.25 rad) and the full width rms-value is less than 0.1 rad. The recorded noise can probably be addressed to acoustic perturbations of the path length difference, to residual changes in background light or to residual electronic pickup noise, possibly also to small temperature induced drifts. The recorded noise is comparable with the phase uncertainty of 0.13 rad expected from the finite step size of the delay line.

A second test of interferometer stability refers to recording wider spectra than obtainable with a single setting of the probe center wavelength (as in figure 6.4). For obtaining wider phase spectra (see section 6.5), interferograms at adjacent probe center wavelengths were recorded such that the wings of the amplitude spectra overlap. In the overlapping range, besides a spectrally constant offset, we found that the difference in phase variation between two spectra was typically only 0.01 rad. This means that, by correcting for the offset, wide-range phase spectra can be assembled from adjacent, overlapping spectra with only small error (about 0.01 rad per spectrum).

6.4 Phase changes induced with drive radiation at around 1100 nm

In the following we present inteferograms, which were recorded with a probe center wavelength of 2102 nm (142.7 THz), while the PhC was illuminated also with drive radiation from the OPO signal wave (constant center wavelength of 1166 nm). Four interferograms were recorded in which the peak of the drive pulse was stepwise delayed with regard to the peak of the probe pulse by various different times, 670 fs, 130 fs, and 65 fs until both pulses arrive simultaneously on the sample (0 fs). The corresponding interferograms are displayed in figure 6.6.
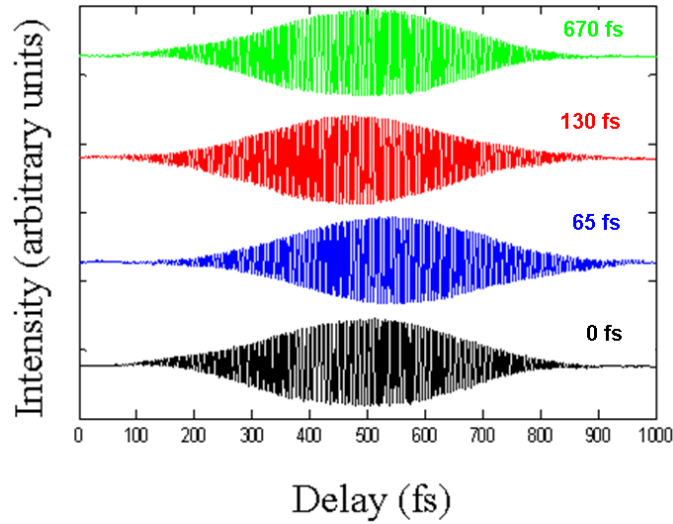
Figure 6.6 Interferogram recorded with the PhC in one arm of the MZI interferometer with a probe center wavelength of 2102 nm. In the first three traces the 1166 nm drive pulse arrives after the probe pulse with a delay of 670 fs (green trace), 130 fs (red), and 65 fs (blue). The black trace is recorded when the probe and drive pulse arrive simultaneously (no delay between the peaks of the pulses).

As can be seen, the interferograms look quite similar, except that there is some slight relative shift of the maximum in the envelope and also some weak differences in the shape of the envelopes. However, here, for a closer inspection of phase shifts induced by optically nonlinear effects we have so far only concentrated on the phase spectra obtained from *FFT*. The corresponding phase spectra are shown in figure 6.7.
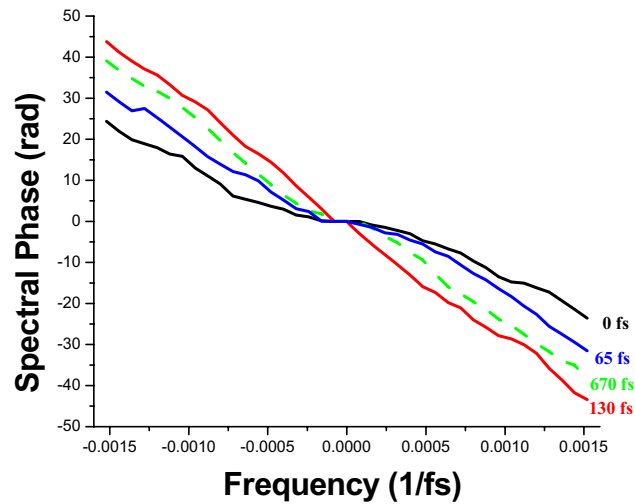
Figure 6.7 Phase spectra of the four interferogram in figure 6.6 for frequencies around the probe center frequency of 142.7 THz (2102 nm). The spectral bandwidth of the probe pulses is larger than the shown range. The drive pulse is delayed with regard to the probe pulse by 670 fs (green trace), 130 fs (red), 65 fs (blue) and the black trace corresponds to zero delay. The horizontal axis displays the probe frequency with regard to the central probe frequency of 142 THz (2102 nm).

One can notice two main features in the spectra. The first is a negative overall slope of all spectra and all curves, independent of drive pulse delay, show the same slope at the ends of the spectrum. For a comparison, interferometer measurements were also performed on with a gold mirror as the sample (such as in figure 6.4, no drive laser present) and with an unpatterned SOI wafer, with and without the drive laser. In all of these cases, we found a phase spectrum which is to good approximation a linear function vs. frequency, i.e., no significant change of slope was found. Based on these observations we address the overall negative slope in figure 6.7 simply to different dispersion provided by the Si PhC or a SOI wafer and the CaF_2 lens in the sample arm with regard to the two gold mirrors which are present in the reference arm.

The second feature to be seen is a drive-probe delay dependent effect, i.e., an optically nonlinear

effect. In particular one can see that, superimposed on the general slope, there is a delay dependent change of phase centered at the probe frequency (142.7 THz, 2102 nm). For an easier interpretation of the delay dependent change of phase in the spectra, we subtracted from the spectra the overall negative slope part (from the trace with no delay) and replotted the result in figure 6.8.
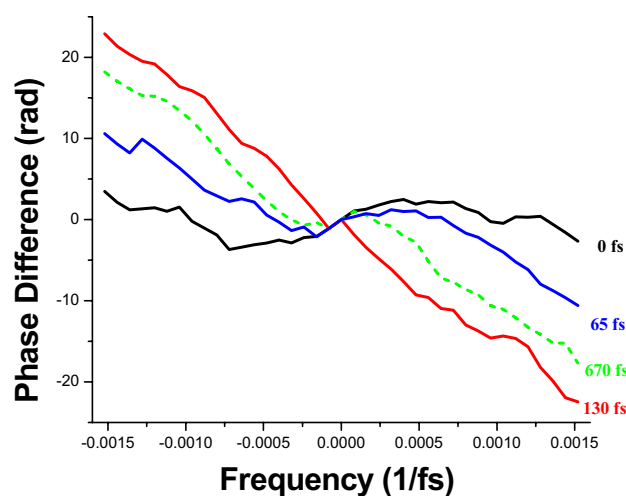
Figure 6.8 Phase difference of the four phase spectra in figure 6.7 around the probe center frequency of 142.7 THz (2102 nm). The horizontal axis displays the probe frequency with regard to the central probe frequency of 142 THz (2102 nm).

It can be seen that the drive laser induced phase change follows a dispersive spectral shape. The found shape actually resembles a third-order function of frequency with a change of sign at the center probe frequency.

For a qualitative interpretation of such phase spectra, we recall which phase spectra of ultrashort pulses correspond to what pulse shapes in the time domain. Specifically, we find that a third-order variation in phase spectra corresponds to a temporally asymmetric pulse shape. Such shapes are found typically from the reflection of ultrashort pulses from a saturable absorber where the leading edge of the pulse reduces the intensity while the associated excitation of

99

carriers reduces absorption in the trailing edge [17]. However, in the experiments described here the probe laser wavelength is too long for linear absorption, i.e., the probe photon energy is well below the Si bandgap energy and even below the half-gap energy.

A related process leading to an asymmetric temporal shape is self-phase modulation caused by two-photon absorption [18]. Briefly, absorption in the leading edge of the pulse excites carriers that provide a reduced index for the trailing edge. In our experiments the shown phase spectra might have been caused by two-photon absorption as well. As the phase spectra on the delay between the probe and drive pulse, and as both the probe and the drive pulse photon energies are below the bandgab energy of Si, such two-photon absorption needs to involve both pulses (non-degenerate two-photon absorption). Possible explanations for the observed phase spectra are then as follows.

When a delayed drive pulse is present which partly overlaps with the probe pulse, two-photon-absorption can occur in the trailing edge of the probe pulses. This reduces the reflected probe power in the trailing edge and leads to a temporal asymmetry in the reflected probe pulse and, consequently, to a third-order component in the observed phase spectra. However, the asymmetry should then be strongest when the probe and drive pulses overlap only partially while, in the experimental spectra, the third-order phase component is strongest at zero delay.

Regarding index changes that follow carrier excitation via non-degenerate two-photon absorption, the index of the sample and thus the reflection phase would change for the trailing part of the probe pulse. This may thus be named cross-phase modulation by two-photon absorption induced carrier excitation. Note that this can introduce a temporal asymmetry in the reflected probe pulse also at full overlap with the drive pulse, because the effect was also observed in degenerate two-photon absorption [18].

Finally, what can be noticed in figure 6.8 is that one of the recorded phase spectra (dashed curve in figure 6.8) shows some third-order component in the phase spectrum as well, although it was recorded with the drive pulses arriving much after the probe pulses (670 fs). Unfortunately, so far, we have no clear explanation for this observation.

6.5 Phase changes induced with drive radiation at around 750 nm

In the last part of the experiments presented here, we show phase spectra that cover a much wider spectral range than the previously discussed measurements. The intention of this is to cover a range which is larger than the spectral width of the inspected photonic resonance which extends approximately from 1950 to 2050 nm (ΓM, TE, 45°, see chapter 4). For achieving a wide spectral coverage from 1900 to 2100 nm, we recorded a series of 19 interferograms at adjacent probe center wavelength (see section 6.3).

As the second change we employed the pulses from the TiSa lasers as drive pulses for the PhC, simultaneously with the probe pulses (no delay). The intention of this is our expectation that, due to the shorter wavelength (photon energy larger than the Si bandgap energy), a higher density of free charge carriers would be achieved with single-photon absorption, leading to a stronger dependence of recorded spectra from the drive laser intensity.

For each of the 19 probe wavelengths, a set of four phase spectra was recorded: 1) with the PhC as sample and the drive laser pulses turned on, 2) with the PhC as sample and the drive pulses turned off, 3) with a bulk SOI wafer as sample (no hole pattern) and the drive pulses turned on, and finally 4) with the bulk SOI wafer as sample and the drive pulses turned off.

The motivation to record these four spectra was to search for carrier excitation induced phase changes which are due to the common effect of an index change and the photonic resonance, but not to the photonic resonance alone, and not to a carrier induced index change alone. In view of the larger wealth of data obtained from the described measurements we present here only the two most relevant phase spectra. The first spectrum is shown in figure 6.9 as the black symbols. It is obtained by recording the spectrum with the PhC in place and the drive pulses on, and subtracting from this the spectrum from the PhC with the drive pulses blocked. The second spectrum is shown in figure 6.9 as the red symbols. This difference spectrum is obtained in the same manner with the bulk SOI wafer used as sample.
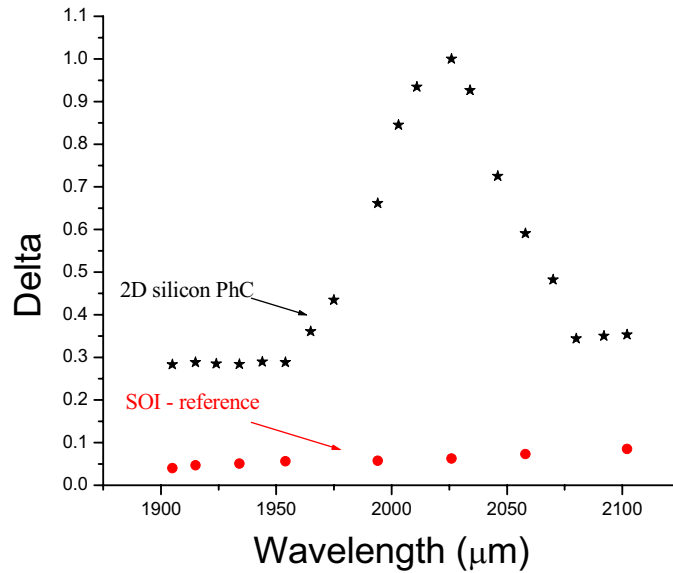
Figure 6.9 Black symbols: phase difference (delta) as a function of probe wavelength measured with the 2D PhC sample (difference in phase spectrum with and without drive pulses). Red symbols: phase difference with the unpatterned SOI wafer.

In figure 6.9 can be seen (black symbols) that turning on the drive laser pulses leads to a spectrally dependent phase change in the light reflected from the PhC. To more detail, the turn-on of the drive laser generated a peak of about 1 rad height located at around 2100 nm, and it generated a spectrally flat change of phase of about 0.3 rad. The peak possesses a full width at half-maximum of about 60 nm above the flat change of phase. Note that the recorded phase changes are well outside the experimental uncertainties as determined in section 6.3. Note also that the peak of phase change occurs at the same center wavelength as the peak of reflected power due to the guided photonic resonance, as was found before with probe radiation alone (located at 2100 nm with a similar bandwidth of about 100 nm, see chapter 4). In comparison, if the SOI wafer is used as the sample (red symbols), the turn-on of the drive pulses induces only a

spectrally flat and smaller change of phase, approximately 0.05 rad, without any signs of a resonance.

Our general interpretation of these observations is that the peak-shaped phase change is based on the presence of a photonic resonance and, simultaneously, on an optically induced effect caused by the drive laser. This is supported by the observation that the turn-on of the drive laser only generates a spectrally flat change of phase with the unpatterned SOI sample. A possible explanation for the optically induced peak in figure 6.9 is that the drive laser had excited free charge carriers and with this a broadband change of the refractive index, as seen with the SOI wafer. However, when a photonic resonance is present (PhC used as sample), probe light with frequencies in the range of the guided photonic resonance experiences more of this index change by a longer effective interaction, than probe light with frequencies outside the resonance.

The same interpretation from a different point of view is the following: the drive laser induces an index change in the PhC such that the probe pulses should experience a spectrally shifted resonance in the reflected power spectrum. This has been predicted by Banaee et al. via calculating the power spectra of light reflected from guided resonance in 2D PhC waveguide slabs [3]. However, when looking at the Kramers and Kronigs' (*KK*) relations [19] one finds that this would also spectrally shift the phase spectrum which is associated with the power resonance. Here, the power spectrum of the inspected photonic resonance is largely symmetric and thus a dispersive phase spectrum can be associated with it, which shifts with drive laser intensity. As a result one expects that the shape of recorded difference phase spectrum (black symbols in figure 6.9) is that of a dispersive spectrum from which the same, but shifted, spectrum, is subtracted, i.e., a double-dispersive shape.

This argument would apply only when the drive laser induced carrier density is constant during the duration of the probe pulses. Here, however, the situation is more complicated due to two averaging effects. Firstly, the spot size of the probe on the crystal (about 20 μm) is not much smaller than that of the drive laser (25 μm) with the result that the probe pulse reflection averages over a range of phase changes caused by various locally different drive intensities. Secondly, the duration of the probe pulses (150 fs) is longer than that of the drive pulses (100 fs). This yields a similar, temporal average in the probe reflection phase. Due to the named averaging, any finer spectral features in the difference phase may be lost, leaving only the

spectrally slowest feature.

We assume that such averaging effects are the reason why we did not observe a double-dispersive difference phase spectrum but only a single-peaked spectrum. Nevertheless, the width of the experimentally observed peak, which is approximately 60 nm should then correspond to the average, optically induced spectral shift of the guided resonance. When comparing the width of the resonance in figure 6.9 with the carrier induced shift in power spectra obtained by others, we find an agreement within a factor of about 20. For instance, a guided resonance was shifted by about 3×10^{-3} (5 nm near 880 nm in AlGaAs) with a pump fluence of 2.3 mJ/cm^2 [7]. In our case, the pump fluence is smaller by about a factor of two, in the order of 1mJ/cm^2 (7 nJ drive pulse energy focused to a spot size of 25 μm) and the relative width of the of the resonance in figure 6.9 is about 3×10^{-2} (60 nm at 2100 nm). Possibly, the factor of 20 stronger effect in our case may be explained by a much more efficient excitation of charge carriers. While Bristow et al. used drive pulses which were detuned to below the single-photon absorption edge, we use single-photon excitation of carriers which is supposed to yield a much higher carrier density. Nevertheless, a more quantitative evaluation of our experimental data is required to verify the suggested interpretation of the results.

6.6 Conclusions

We have interferometrically observed, for the first time, an ultrafast nonlinear optical phase switching in a photonic crystal. An interferometric detection was used in view of the inherently high sensitivity to small phase changes as expected to occur for the moderate intensity available from standard modelocked oscillators with nanojoule pulse energies used here.

Interferometric detection was accomplished with a Mach-Zehnder interferometer into which an ultrafast mid-IR probe pulse enters, and where the 2D PhC slab is used in reflection in one of the interferometer arms. The reflection angle and the probe wavelength were selected to excite a guided photonic resonance where the photon energy is below half of the electronic bandgap of silicon from which the photonic crystal is made. To induce optically nonlinear effects, an additional ultrashort pulse, called the drive pulse, is sent to the crystal at various delay times

with respect to the probe pulse.

When using a longer wavelength for the drive pulse, with photon energy below the electronic bandgap of silicon, we observe that the reflected probe light experiences a spectrally dependent phase shift which changes on fs-time scales with the drive pulse delay. The drive pulse induced phase shift spectrum resembles that of third order dispersion which is usually associated with temporally asymmetric pulses. In a second experiment, drive pulses with a shorter wavelength where used, such that the photon energy is larger than the electronic bandgap and, additionally, a wider mid-IR range was covered, achieved with a stepwise tuning of the center wavelength of the probe pulses. In this case we observe a drive laser dependent, i.e., nonlinear optical phase shift which is larger within the bandwidth of the probed photonic resonance. This proves a resonant enhancement of the optically induced phase response by the photonic resonance.

The named observations can be termed ultrafast phase switching of the PhC when looking at the ultrafast time scale on which this occurs. So far, the physical mechanisms that have contributed to the phase switching are not identified in detail. We believe however, as based on the shape of the observed phase spectra, that drive-pulse-controlled saturable absorption or two-photon absorption based cross phase modulation can be involved.

After an optimization of the observed ultrafast phase switching this may offer potential applications, such as for switching the transmission of photonic Fabry-Perot interferometers [20]. But the immediate steps would have to focus on a more detailed analysis of the underlying switching mechanisms and, possibly, an extended experimental characterization. For the latter, to enable detection with largely increased spectra bandwidth, and to avoid stepwise tuning, one may consider to combine probe pulses from so-called white light generation [7], and to avoid tuning with the interferometric detection.

References

[1] P. Tran, *Phys. Rev. B* **52**, 10673 (1995)

[2] V. Lousse and J.P. Vigneron, *Phys. Rev. E* **63**, 027602 (2001)

[3] M.G. Banaee, A.R. Cowan, and J.F. Young, *J. Opt. Soc. Am. B* **19**, 2224 (2002)

[4] A. Hache and M. Bourgeois, *Appl. Phys. Lett.* **77**, 4089 (2000)

[5] M.D. Rahn, A.E. Fox, M.S. Skolnick, and T.F. Krauss, *J. Opt. Soc. Am B* **19**, 716 (2002)

[6] J.P. Mondia, H.W. Tan, S. Linden, H.M. van Driel, and J.F. Young, *J. Opt. Soc. Am. B* **22**(11), 2480 (2005)

[7] A.D. Bristow, J. Wells, W. Fan, A. Fox, M. Skolnick, D. Whittaker, A. Tahraomi, T. Krauss, and J. Roberts, *Appl. Phys. Lett.* **83**, 851 (2003)

[8] M.I. Gallant and H.M. van Driel, *Phys. Rev. B* **26**, 2133 (1982)

[9] P.M. Johnson, A.F. Koenderink, and W.L. Vos, *Phys. Rev. B* **66**, 081102 (R) (2002)

[10] P. Murzyn, A.Z. Garcia-Zeniz, D.O. Kundys, A.M. Fox, J. Wells, D.M. Whittaker, M.S. Skolnick, T.F. Krauss, and J.S. Roberts, *Appl. Phys. Lett.* **88**, 141104 (2006)

[11] S.W. Leonard, H.M. van Driel, J. Schilling, and R.B. Wehrspohn, *Phys. Rev. B* **66**, 161102 (2002)

[12] Optical Sciences (OT) group, Prof. Dr. Jennifer Herek, Prof. Dr. L. Kuipers, Dr. Herman Offerhaus, University of Twente, MESA+ Institute for Nanotechnology, The Netherlands

[13] S. Diddams and J. C. Diels, *J. Opt. Soc. Am.* B **13**, 1120 (1996)

[14] M. Takeda, H. Ina and S. Kobayashi, *J. Opt. Soc. Am.* **72**, 156 (1981)

[15] Y. Xi and C. Ai, *Proc. SPIE* **2003**, 254 (1993)

[16] K. Lepla, and G. Horlick, *Appl. Spectrosc.* **44 (8)**, 1259 (1990)

[17] Peter van Voorst, PhD Thesis - Chapter 5, University of Twente, 2008

[18] T. Ulmer, R. Tan, Z. Zhou, S. Ralph, R. Kenan, C. Verber, and A. Thorpe, *Opt. Lett.* **24**, 756 (1999)

[19] D.C. Hutchings, M. Sheik-Bahae, D.J. Hagan, and E.W. Van Stryland, *Opt. Quant. Electron.* **24**, 1 (1992)

[20] W. Suh, M. Yanik, O. Solgaard, and S. Fan, *Appl. Phys. Lett.* **82**, 1999 (2003)

Mid-infrared characterization of two-dimensional photonic crystal slabs fabricated in silicon with laser interference lithography

Chapter 7 Summary

This thesis describes the fabrication and optical characterization of two-dimensional, waveguiding photonic crystals, so-called 2D PhC slabs.

A photonic crystal for use in the mid-IR spectral range was fabricated by developing a novel type of laser interference lithography (LIL). The important improvements with regard to standard LIL methods are that also high-index materials can be patterned over large (cm^2) areas, and that deeper etching of these patterns is possible. These are essential properties to fabricate large area photonic crystals with high index contrast and enable to make use of standard silicon-on-insulator (SOI) wafers.

The crystal was fabricated with a square pattern of round air holes at 1 μm spacing to obtain photonic bandgaps and guided resonances in the mid-IR. Of particular interest was to provide guided photonic resonances at wavelengths longer than about 2 μm, where the photon energy is below half of the electronic bandgap, as would be desired to suppress unwanted two-photon absorption at high light intensities.

The crystal was characterized with regard to the named linear optical properties via reflection and transmission experiments in the near and mid-IR. From this and comparison with a numerical modeling, the dispersion of guided modes was deduced. The probing of guided photonic resonances yielded Fano-type resonances superimposed on broad Fabry-Perot (Airy) resonances in good agreement with the theoretical prediction. From fits to several of the recorded Fano resonances we deduced the extrinsic losses in terms of quality factors, which

quantifies the fabrication quality of the novel LIL method applied here. Additionally, a guided resonance with its photon energy below half of the electronic bandgap was selected for a characterization of also nonlinear optical properties of the crystal.

For the optically nonlinear characterization we applied, for the first time, an interferometric detection of light induced, ultrafast phase changes (phase switching) in a photonic crystal. Two largely different wavelengths were used for the ultrashort pulses that induce the phase switching. In the recorded interferograms, phase switching shows as light induced phase changes in the mid-IR probe pulses reflected from the photonic crystal which changes on ultrafast (fs) time scales and which is enhanced by the photonic resonance. In particular, from the shape of the observed phase spectra we conclude that either, single-photon or two-photon absorption based excitation of charge carriers can be responsible for the observed phase switching, depending on the wavelength used to induce phase switching.

Acknowledgments - Dankwoord

The end of one journey means the beginning of another one. After two-years of working as a researcher while exploring the western part of Europe, I started my PhD program in the eastern part of The Netherlands, at Twente University (UT) in 2003. During the last year of this journey, I was offered the chance to continue my journey in Netherlands Centrum for Laser Research (NCLR, on the UT campus). Throughout all these years, I was lucky to meet and let to know a large number of precious people: friends, co-workers and advisors. Therefore I take the opportunity to thank the persons who contributed directly or indirectly to the completion of my thesis with success.

First of all, I would like to thank Professor Klaus Boller and Dr. Petra Gross, my promotor, respectively assistant promotor, from whom I learned the rigorous academic attitude needed. Thank you very much, Klaus, for your attention and enormous commitment on guiding my work from the very beginning until writing this thesis, tolerance while dealing with my personality, for all your comments and advice on our research projects over the years. And, thank you very much, Petra, for your didactical supervision, infinite patience and for taking care of the smallest details while correcting my manuscripts. This must have taken a lot of your precious time. Thank you also for your attractive, understandable and straightforward style of revealing thoughts which have proven to be often-exceptional and for allowing us benefit from it. Our enthusiasm and ideas have converged to the results presented in this PhD thesis.

Additionally, I am particularly grateful to Professor Kobus Kuipers, for his valuable ideas about the nanocrystals and scientific assistance on my manuscript. Thank you, Kobus, for being so enthusiastic and communicative about nanotechnology, for your optical expertise, and for teaching me very useful tips on general cleanroom procedures during the period of time we had a daily chance to discuss about the fabrication of our photonic crystals.

My gratitude extends as well to all the members of my graduation committee for kindly agreeing to examine my thesis.

Thanks also to Roel and Ronald for being my *paranimfen* during the Ph.D. defense and for working together in the same research project as part of investment in our future.

Finally, I would like to dedicate this thesis to Oxana and Vanessa-Maria, for encouraging me all along this fascinating journey and your love with the promise of spending more time together after completing this PhD study.

Liviu Prodan
28th March 2008, Enschede, The Netherlands

Curriculum Vitae

Liviu Prodan
Born: January 25th, 1976, Iasi, Romania

September 1990 – June 1994
Baccalaureate diploma – chief of promotion
High School, Physics and Chemistry Group "Radu Cernatescu", Iasi, Romania

October 1994 – June 1999
Bachelor of Physics (B.Sc.), Technological Physics specialization – ranked third
Laser Optics Department
Faculty of Physics, Alexandru Ioan Cuza University, Romania

October 1999 – February 2001
Master Scholarship (M.Sc.) – ranked first
Plasma Physics Department and Institute for Spectrochemie and Spectroscopie, Dortmund, Germany

March 2001 – January 2002
Researcher
Dutch Polymer Institute, Eindhoven, The Netherlands

February 2002 – May 2003
Researcher
Laser Physics Group, The Netherlands

June 2003 – May 2007
Ph.D. student – onderzoek in opleiding
Stichting voor Fundamenteel Onderzoek Materialen (FOM) and Laser Physics and Nonlinear Optics Group, Twente University, The Netherlands

June 2007 – March 2008
Researcher
Laser Applicatie Centrum (LAC), The Netherlands
Laser Physics and Nonlinear Optics Group, Twente University, The Netherlands

April 2008
Researcher
Netherlands Centrum voor Laser Research (NCLR)